Studies on the Nonlinear Seismic Response of Soil-Structure Interaction Systems(Dissertation_全文)

AUTHOR(S):

Miura, Fusanori

STUDIES ON THE NONLINEAR SEISMIC RESPONSE OF SOIL-STRUCTURE INTERACTION SYSTEMS

By

Fusanori MIURA

Disaster Prevention Research Institute
Kyoto University

STUDIES ON THE NONLINEAR SEISMIC RESPONSE OF SOIL-STRUCTURE INTERACTION SYSTEMS

By

Fusanori MIURA

Disaster Prevention Research Institute
Kyoto University

SUMMARY

This dissertation is devoted to investigations by the finite element method of the dynamic characteristics of nonlinear soil-structure interaction systems and of the dynamic stability of structures.

A general method is proposed to analyze nonlinear soil-structure interaction which considers the sliding and separation phenomena at the interfaces between the soil and structure, and the nonlinear behavior of soil. The joint element has been used to model the contact surface and its constitutive relationships are determined from a variety of simple shear tests of various construction materials and soils. A joint element which is three-dimensional was developed to investigate the dynamic characteristics of three-dimensional nonlinear systems and to provide comparisons with two-dimensional systems.

The stability against sliding of a massive structure was analyzed by classical methods and that proposed here. Dynamic characteristics such as the frictional resistance of pile surfaces and the lateral group efficiency of a group of piles are clarified. The dynamic stability of an existing slope is discussed. The effects of ground water on the stability are taken into consideration. Finally, a procedure to take into account the effects of hydrodynamic pressure on nonlinear soil-structure interaction systems is presented, and the dynamic stability of a revetment structure under such pressure is measured.

ACKNOWLEDGEMENTS

The author wishes to express his sincere gratitude to Professor Kenzo Toki of the Disaster Prevention Research Institute of Kyoto University for guidance and constant encouragement during the course of this study and also for his critical reading of the manuscript. Special appreciation is extended to Professor Toru Shibata of the Disaster Prevention Research Institute of Kyoto University for suggestions and advice. Professor Tadanobu Sato of the Disaster Prevention Research Institute of Kyoto University gave valuable suggestions and constructive criticism. Thanks are due to Professor Yuzo Onishi of Kyoto University and Mr. Hideaki Kishimoto of Japan Computer Consultants, Osaka, for their suggestions regarding the programing of the computer codes. Professors Toshihisa Adachi of the Disaster Prevention Research Institute of Kyoto University and Masayoshi Shimizu of Tottori University gave helpful advice concerning the experiments in chapter 1. The author further wishes to thank Mr. Susumu Emi of the Hanshin Expressway Public Corporation for valuable advice and to his colleagues of Professor Toki's laboratory for their profitable discussions and general support.

TABLE OF CONTENTS

INTRODUCTION

1. General Remarks

The Japanese archipelago is located in the Circum Pacific Seismic Zone and it has frequently been affected by serious earthquakes. In the design of almost all structures, therefore, it is normal practice to take into account the effect of earthquakes, an important environmental factor.

In recent decades, the dynamic interaction between the soil and structures has been regarded with growing interest by workers in the field of earthquake-resistant design as man-made structures have been built on a larger and larger scale. Dynamic response analyses of soil-structure interaction systems are necessary in order to grasp the dynamic characteristics of structures and to enable the design of structures which can satisfactorily resist the force of earthquakes.

Soil-structure interaction is defined as the transmission of kinematic energy through the interface of the soil and structure. This interaction is affected not only by the mechanical properties of the constituents but also by the geometrical form and condition of the interface. Accordingly, there is no one universal method to analyze dynamic interaction, although various methods such as the elastic wave propagation method, the finite element method and the spring-dashpot replacement of the interface effect are generally used. Most studies concerned with soil-structure interaction assume a perfect bonding on the contact surface between the soil and structure, but static normal stress due to the surcharge along the contact surface is not generally considered. The practical application of these assumptions inevitably

imply tensile stress on the contact surface. In the actual system, separation phenomenon may occur at the interface where tensile stress is generated, and seismic force is transmitted through the decreased contact area which then result in an increase in contact stress. As the stress-strain relationships of soil depends on the intensity of confining pressure, strong nonlinear behavior will appear in the case where there are variations in the interface's areas. Moreover, sliding phenomena may occur during strong earthquakes, and then the response of the soil-structure system will be greatly different from the response when perfect bonding at the interface is assumed.

There have been many attempts by researchers in the fields of soil and rock mechanics to clarify discontinuous plane mechanisms in continuous material and many models to express this discontinuity have been proposed. Anderson et al.[1] proposed a "pin-ended element" and Goodman et al.[2,3] a "joint element". They applied their models to the discontinuous line in continuous rock. Zienkiewicz et al.[4] also proposed a "joint element" in which the stiffness matrix is derived differently from that proposed by Goodman et al. Ngo et al.[5] suggested a "linkage element" and adopted it in an examination of the bondage strength between the reinforcement and the concrete of reinforced concrete. Herrmann[6] outlined a detailed procedure to analyze contact problems with the aid of a "bond link element". Bazant et al.[7] examined crack propagation by introducing "sharp inter-element cracks" and "blunt crack bands" in finite element mesh. All of the above however, fall into the category of static problems.

Some analytical research has concerned separation and sliding between the soil and structures during seismic excitation. A series of analyses have made by Wolf et al.[8-11] to examine the dynamic characteristics of a nuclear reactor building when a partial lifting-off has taken place. Uchida et al.[12], Kennedy et al.[13] and Takemori et al.[14] used nonlinear rocking springs to examine the seismic response charac-

teristics of a nuclear reactor building with the partial lifting-off as one factor. Yim et al.[16] proposed methods to analyze dynamic stability against the overturning of a rigid structure. The dynamic sliding stability of a structure has been discussed by Sasaki et al.[17], Kausel et al.[18] and Becker et al.[19] Although each of these methods is a means to analyze individual phenomena, none is complete because they cannot analyze both phenomena at the same time and because it is very difficult to expand any of them to an analysis of an embedded structure when both phenomena are to be taken into account. A general method which can analyze both separation and sliding phenomena simultaneously is necessary.

2. An Outline of the Dissertation

This dissertation presents a method which can effectively analyze nonlinear dynamic interaction, including the material nonlinearity of soil and the phenomena of separation and sliding, by arranging joint elements along the contact surface between the soil and structure. The applications of such a method are also detailed.

Strength parameters such as the angle of friction or interface cohesion can be expected to play important roles in any analysis of nonlinear dynamic responses. Numerous simple shear tests have been performed (chapter 1) in order to clarify the constitutive relationships of the interface that exist between various structural materials and soils. The results obtained from these tests have then been used in analyses.

Chapter 2 describes an effective procedure to analyze dynamic soil-structure interaction considering not only phenomena of sliding and separation but also the nonlinear behavior of soil. This method is based on the application of the joint element, developed by static rock mechanics, to the dynamic problem of interaction. The soil is assumed to be an elasto-perfect plastic material. The seismic responses of two soil-structure models are dealt with in order to illustrate the method's

applicability to actual soil-structure interaction systems as well as clarify the effects of the phenomena on the system's dynamic responses.

In chapter 3, a three-dimensional joint element is developed by an expansion of the two-dimensional joint element, and its applicability to the interaction is discussed. The structure's dynamic stability against sliding is demonstrated by comparing the results obtained by the proposed method with those of classical static methods and two-dimensional analyses.

In chapter 4, responses of pile foundation structures are analyzed in order: (i) to show the effects of embedding the footing on structural responses, (ii) to estimate quantitatively the frictional resistance of the pile surface and (iii) to account for the dynamic lateral group efficiency of piles. In this regard, the present method is employed in order to estimate static and dynamic stresses as well as to account for separation and sliding at the contact surface between the soil and pile foundation.

Chapter 5 investigates in detail the qualitative stability of the existing slope by applying both static and various dynamic forces. Slope stability is compared to the commonly-used estimates. The effects of ground water on slope stability are also examined by a simple model of the pore water pressure buildup. Furthermore, the assessment has been performed when the slope is reinforced by sheetpiles. Joint elements model all of the interfaces between soil elements which in turn are modeled by the ordinal isoparametric element. This makes it possible to estimate dynamic stability against sliding along arbitrary sliding surfaces formed by a series of joint elements, as well as to investigate the progressive failure of the slope.

Linear and nonlinear seismic response analyses are performed on the water-soil-structure interaction system (chapter 6) to determine the effects of hydrodynamic pressure on the response and on the structure's dynamic stability. In principle, the dynamic analysis of this inter-

action must be performed in the frequency domain because of the hydrodynamic pressure's frequency dependence. Therefore, the virtual mass equivalent to hydrodynamic pressure is shown to be nearly independent of frequency as long as the water depth is low. A procedure which accounts for the effects of hydrodynamic pressure is described and some results are listed.

The major results are reviewed in the chapter entitled "Concluding Remarks" and proposals are made for future studies.

References

1) Anderson H. W. and J. S. Dodd: Finite element method applied to rock mechanics, Proc. 1st Cong. ISRM, Lisbon, II, pp.317-321, 1966.

2) Goodman R. E., R. L. Taylor and T. L. Brekke: A model for the mechanics of jointed rock, J. Soil Mech. Found. Div., Proc. ASCE, Vol.94, pp.637-659, 1969.

3) Goodman R. E.: Methods of geological engineering in discontinuous rocks, West Publishing Company, chap.8, pp.300-368, 1976.

4) Zienkiewicz O. C., B. Best, C. Dullage and K. G. Stagg: An analysis of nonlinear problems in rock mechanics with particular reference to jointed rock systems, Proc. 2nd Cong. ISRM, Belgrad, pp.8-14, 1970.

5) Ngo D. and A. C. Scordelis: Finite element analysis of reinforced concrete beams, J. of ACI, Vol.64, No.3, pp.152-163, 1967.

6) Herrmann L. R.: Finite element analysis of contact problems, Proc. ASCE, No.EM5, Oct., pp.1043-1057, 1978.

7) Bazant Z. P. and L. Cedolin: Blunt crack band propagation in finite element analysis, Proc. ASCE, No.EM2, Apr., pp.297-315, 1979.

8) Wolf J. P.: Soil-structure interaction with separation of base from soil (lifting off), Nucl. Eng. and Design 38, pp.357-384, 1976.

9) Wolf J. P.: Seismic response due to travelling shear wave including soil-structure interaction with base-mat uplift, Int. J. Earthq. Eng. Struct. Dyn., Vol.5, pp.337-363, 1977.

10) Wolf J. P. and P. E. Skrikerud: Seismic excitation with large overturning moments: tensile capacity, projecting basement or lifting off?, Nucl. Eng. and Design 50, pp.305-321, 1978.

11) Wolf J. P. and P. Obernhuber: Effects of horizontally propagating waves on the response of structures with a soft first storey, Int. J. Earthq. Eng. Struct. Dyn., Vol.9, pp.1-21, 1981.

12) Uchida K., T. Miyashita and S. Nagata: Earthquake response analysis of a nuclear power plant building with a circular basemat, Ann. Re-

port Kajima Institute of Construction Technology, 21, pp.673-678, 1973, (in Japanese).

13) Kennedy R. P., S. A. Short, D. A. Wesley and T. H. Lee: Effect on nonlinear soil-structure interaction due to base slab uplift on seismic response of a high-temperature gas-cooled reactor (HTGR), Nucl. Eng. and Design 38, pp.323-355, 1976.

14) Takemori T., K. Sotomura and M. Yamada: Nonlinear dynamic response of reactor containment, Nucl. Eng. and Design 38, pp.463-474, 1976.

15) Tsuboi Y., Y. Hangai, M. Takeda and M. Honma: A simple analytical method of walled structure considering up-lift of foundation, Proc. 5th Japan Earthq. Eng. Symp., pp.1265-1272, 1978.

16) Yim C. S., A. K. Chopra and J. Penzien: Rocking response of rigid blocks to earthquakes, Int. J. Earthq. Eng. Struct. Dyn., Vol.8, pp.565-587, 1980.

17) Sasaki Y., Y. Fujino and M. Hakuno: Sliding of mass by seismic excitation- the influence of UD components-, 33rd Proc. Ann. Meeting of JSCE, I-185, 1978, (in Japanese).

18) Kausel E. A., A. S. Lucks, L. Edgars, F. Swiger and J. T. Christian: Seismically induced sliding of massive structures, Proc. ASCE, No.GT12, Dec., pp.1471-1488, 1979.

19) Becker J. M., C. Lorente and P. Mueller: Seismic response of precast concrete walls, Int. J. Earthq. Eng. Struct. Dyn., Vol.8, pp.545-564, 1980.

A METHOD TO ANALYZE THE PROBLEMS OF NONLINEAR INTERACTION CAUSED BY SEISMIC EXCITATION

1. Dynamic Properties of the Contact Surface between the Soil and Structures

1.1 General remarks

There is the possibility that sliding and/or separation will occur at the contact surface between the soil and structure during strong earthquake motion. The joint element proposed by Goodman[1] is suitable to express these mechanisms and therefore, has been employed.

Strength parameters such as the angle of friction or cohesion have a considerable effect on the nonlinear dynamic responses. This makes it necessary to investigate the nonlinear constitutive relationships of the contact surface between various structural materials and soils and to establish what would be reasonable in the case of the joint element.

Potyondy[2] performed a large number of experiments on the frictional strength of the contact surface between various structural materials including wood, concrete and steel and soils such as clay, sand and cohesive granular soil. Kishida and Yoshimi et al.[3-6] investigated the friction resistance at the surface between metal and sand using a ring torsional shearing apparatus by which the grain behavior of the soil specimen can be observed in a greatly deformed state by x-ray. Ishido et al.[7-9] investigated the frictional strength between different construction materials and sand and applied the results to that between concrete walls and soil. Miyamoto et al.[10] examined the frictional characteristics of concrete and sand and quantified the roughness of the surface of con-

crete which had not been specifically quantified previously.

Most of the research, however, has paid attention only to peak strength, but this is not sufficient information to characterize the behavior of the contact surface. For this reason, experiments performed here have been designed to fully clarify the frictional characteristics of a surface.

1.2 A description of the experiments

(1) Test and measuring apparatus

Two kinds of tests have generally been used to determine the soil strength - the triaxial compression test and the direct shear test. One kind of direct shear test, the single-plane shear test, is suited to an investigation of the strength between construction materials and soils because it can control the shearing plane. It has been used in this study.

The shear box has a shearing area of 19.63 cm^2 (5.0 cm in diameter). The deflection of the load guage and deformations of the specimen are all measured on dial guages and plotted through an amplifier by multi-penrecorder.

(2) Specimens

As frictional strengths between construction materials and soils were compared with the latter's shear strength, two specimen types were necessary for each soil test. One was of construction material and soil and the other was made up of soil only. The former is hereafter referred to as the "compound specimen" and the latter as the "simple specimen". The size of a specimen was 5.0 cm in diameter and 2.0 cm in height. The construction material and the soil in the compound specimens were both 1.0 cm in height.

(3) Test soils and construction materials

In choosing construction materials for the test, consideration must

be given to the application of the results in the field of civil engineering. At the present time, the major construction materials are steel and concrete, and mortar is the primary material discussed here. Glass and stone with rough surface finishes as well as mortar indicate the effects of surface roughness on frictional strength.

Three types of soil, sand, clay and an intermediate soil mixture of sand and clay, and soft rock were used as ground materials. Their material properties are described below.

(a) Soils

The two types of sand were Toyoura sand and river sand, which has a large grain size. Table 1-1 lists their material properties and Fig. 1-1 shows the grain size accumulation curves. The properties of the Fujinomori clay used are listed in Table 1-2. To obtain a cohesive granular soil (an intermediate soil), clay was mixed with sand by two different weight ratios, as follows:

$$\left.\begin{array}{l}\text{Clay : Sand = 1 : 1}\\ \text{Clay : Sand = 2 : 1}\end{array}\right\} \qquad (1\text{-}1)$$

Table 1-1 Material properties of sand.

	Gs	D_{10}
Toyoura sand	2.65	0.16
River sand	2.64	0.32

Table 1-2 Material properties of clay.

Gs	L.L.(%)	P.L.(%)
2.61	48.5	26.7

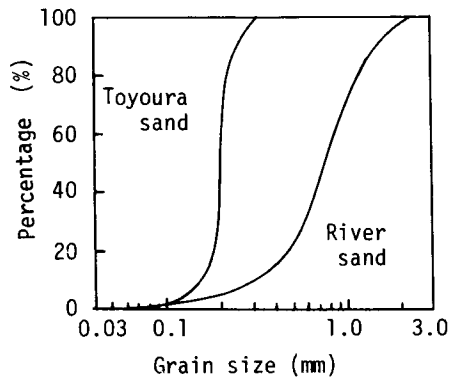

Fig. 1-1 Grain size accumulation curves of Toyoura and river sand.

(b) Construction materials

The roughness of the surface of mortar has been estimated by R_{max} according to JIS B 0601-1970. R_{max} is defined by the difference between the highest and lowest points on the cross section of the surface whose length is 2.5 mm (Fig. 1-2). Soft rock (tuff) was used both as the ground material and as the construction material. When it was used as the construction material, indentations were made artificially on its surface. The average values of R_{max} are:

$$\left.\begin{array}{ll} \text{Mortar} & R_{max} = 0.10 \text{ mm} \\ \text{Soft rock} & R_{max} = 1.35 \text{ mm} \end{array}\right\} \quad (1\text{-}2)$$

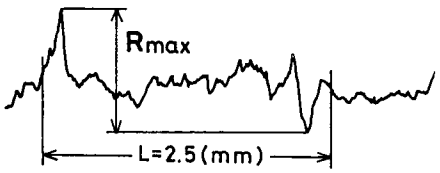

Fig. 1-2 Surface roughness estimation (R_{max}, JIS B 0601-1970).

Glass has also been tested as a construction material under the supposition of the extreme case in which the construction material's surface is perfectly smooth.

(4) Test conditions

As the purpose of this study is to clarify shearing characteristics and to establish the surface's soil-structure constitutive relationships during earthquakes, tests have been performed with a high rate of shearing. The shearing rates were:

$$\left.\begin{array}{l} 24.9 \text{ mm/min}, \quad 2.27 \text{ mm/min} \quad \text{for sand} \\ 49.0 \text{ mm/min}, \quad 2.27 \text{ mm/min} \quad \text{for clayey soil} \end{array}\right\} \quad (1\text{-}3)$$

As a normal shearing rate is about 1.0 mm/min, the shearing rate is nearly fifty times faster than normal one when it is 49 mm/min.

The structures under consideration, e.g. a massive structure or a foundation of a bridge with wide spans are extremely large and heavy and thus, the normal pressure at the contact surface is very great. Pressures up to 8.0 kgf/cm^2 are charged onto the specimen, whereas in past tests, normal pressure has been no greater than 1.5 kgf/cm^2.

1.3 Analyses of experimental results

(1) Relationships between shear stress and horizontal displacement

(a) Sand

The relationships between shear stress τ and horizontal displacement δ are shown in Fig. 1-3(a) when the normal stress is 2.0 kgf/cm^2. In the figure, the solid circles indicate the compound specimen and the open circles the simple specimen. Fig. 1-3(b) shows the relationships between normal displacement ΔH, which corresponds to the volumetric change, and horizontal displacement δ.

As can be seen from Fig.1-3(a) there was no drop in stress in the compound specimen after the yield but there was a remarkable drop in the case of the simple specimen. The shear strength (frictional strength) of the compound specimen was lower than that of the simple specimen. From Fig. 1-3(b), The volume change ΔH was found to be positive, in other words, positive dilatancy occurs during the test, and is of smaller magnitude in the compound specimen than in the simple specimen. These tendencies have been observed in all other tests where the levels of normal stress have been changed.

The effects of shearing rate were then investigated. The resultant $\tau-\delta$ relationships for Tovoura and river sands, respectively, are shown in Figs. 1-4(a) and (b). The open circles and triangles are the results at low shearing rates (2.27 mm/min) and the solid circles and triangles are at high shearing rates (24.9 mm/min). The effects of the shearing rate on the $\tau-\delta$ relationships and on shear strength were negligible.

(b) Clay

Fig. 1-5(a) shows the $\tau-\delta$ relationships in the case of clay. Here, the normal stress , σ_n, is as the same as the consolidation stress, p. The curves are similar to the curves for sand, in other words, there was no stress drop in the compound specimen, but a slight drop in the simple specimen.

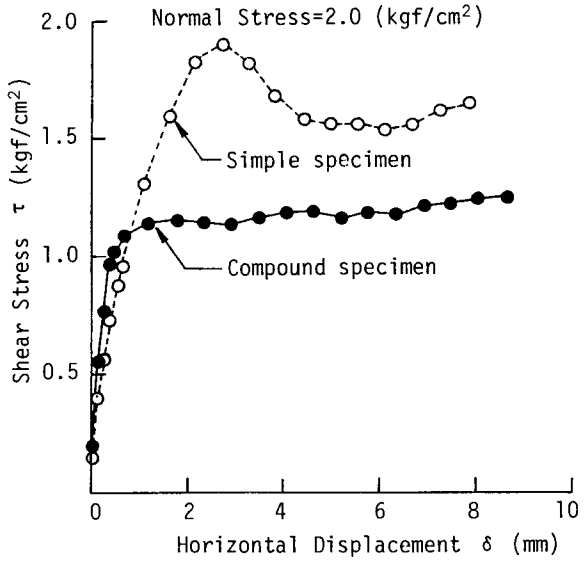

Fig. 1-3(a) The relationship between shear stress, τ, and horizontal displacement, δ, in the case of sand.

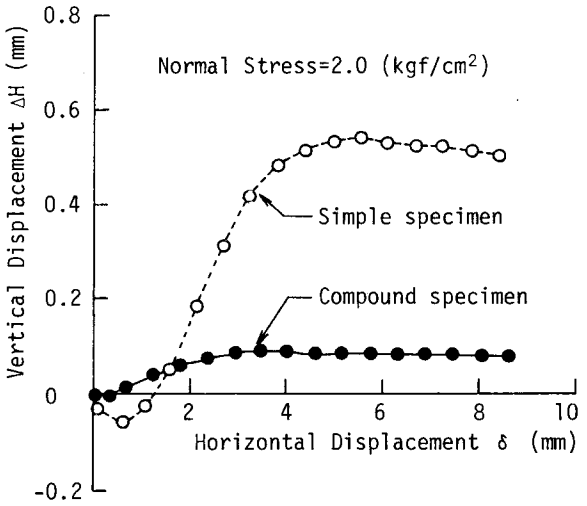

Fig. 1-3(b) The relationship between the volumetric change, ΔH, and horizontal displacement, δ, in the case of sand.

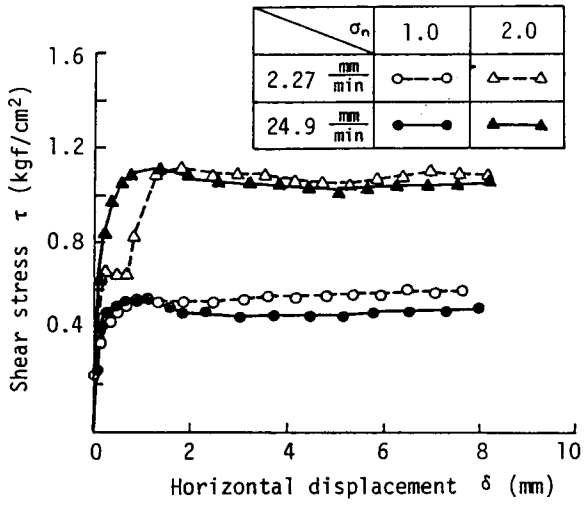

(a) Toyoura sand

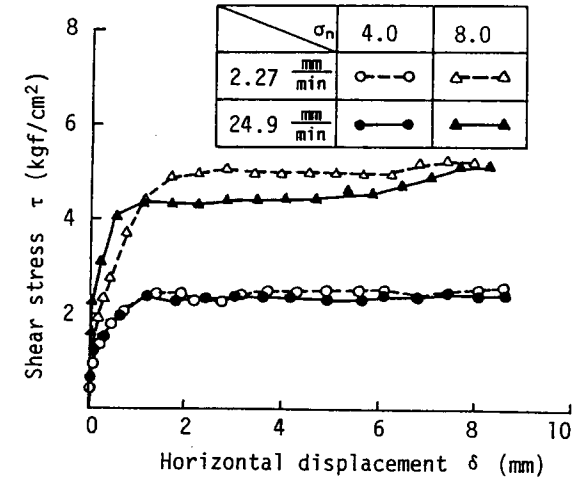

(b) River sand

Fig. 1-4 The effects of shearing rate on the $\tau - \delta$ relationship.

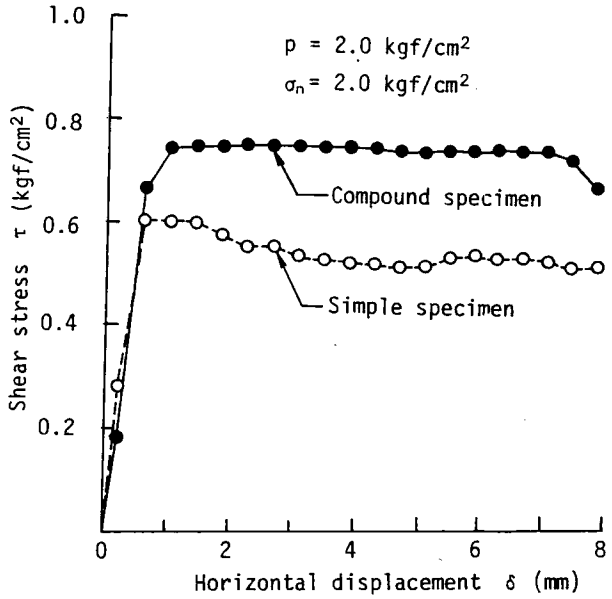

Fig. 1-5(a) The relationship between shear stress, τ, and horizontal displacement, δ, in the case of clay.

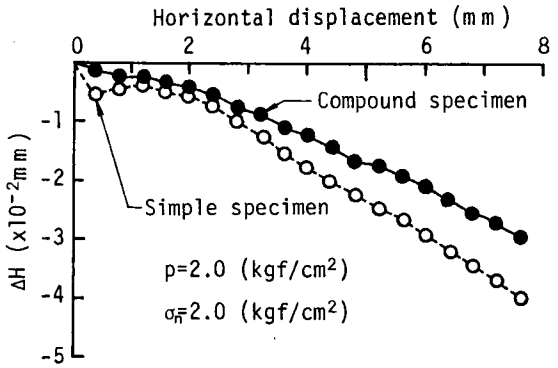

Fig. 1-5(b) The relationship between the volumetric change, ΔH, and horizontal displacement, δ, in the case of clay.

As concerns magnitude, however, the shear strength of the compound specimen is larger than the simple specimen.

Figure 1-5(b) shows the $\Delta H - \delta$ relationships. Clay gave opposite results to those of sand. The volume decreased during the test, i.e., negative dilatancy occured, but of a smaller magnitude in the compound specimen.

The effects of shearing rate on the $\tau - \delta$ relationships obtained from two different shearing rates were compared (Fig. 1-6) and the effects were negligible. For cohesive granular soil, similar tendencies to those of clay were found.

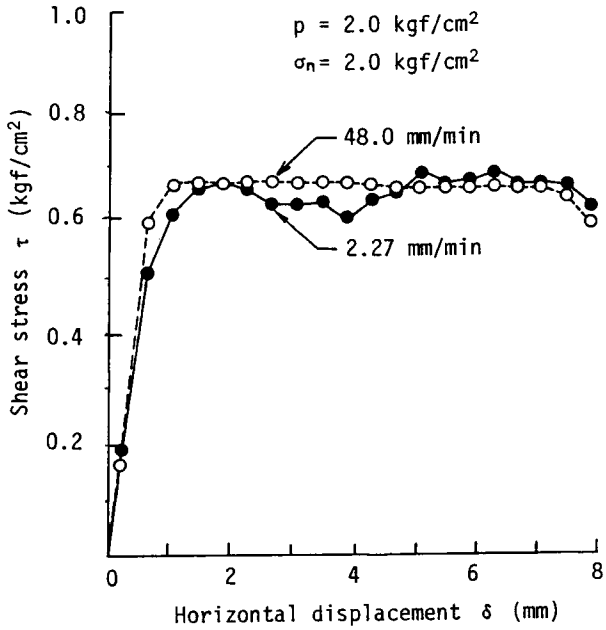

Fig. 1-6 The effects of the shearing rate on the $\tau - \delta$ relationship.

(2) Comparisons of the frictional strength of the contact surface and the shear strength of soil

(a) Sand

Figure 1-7 compares the frictional strength of the compound specimen and the shear strength of the simple specimen. The test numbers from the figure and corresponding test conditions have been tabulated in Table 1-3. From the results, shearing rate, relative density and grain size of sand had little effect on the ratio of the strengths. The ratios all were in the range of $0.70 \sim 0.75$.

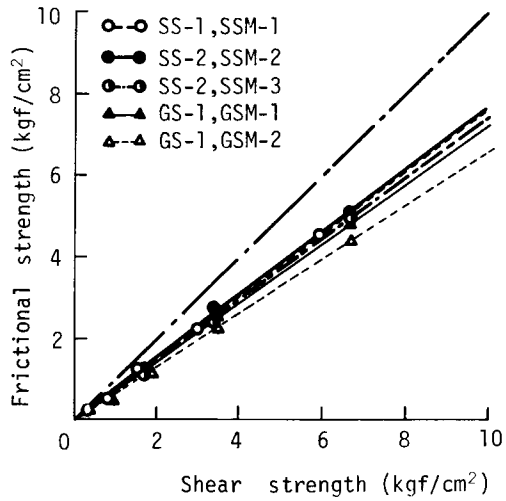

Fig. 1-7 The relationship between the frictional strength of the contact surface and the shear strength of sand.

Table 1-3 Test numbers for simple and compound sand specimens.

	Specimen	Void ratio	Shearing rate(mm/min)	Test No.
Toyoura sand	Simple specimen	0.793 0.684	2.27 2.27	SS-1 SS-2
	Compound specimen	0.787 0.703 0.680	2.27 2.27 24.9	SSM-1 SSM-2 SSM-3
River sand	Simple specimen	0.704	2.27	GS-1
	Compound specimen	0.695 0.696	2.27 24.9	GSM-1 GSM-2

(b) Clay and cohesive granular soil

Figure 1-8 compares the frictional strength and the shear strength of clayey soils. Frictional strength is approximately 1.2 times greater than the shear strength.

Inverse results for sand and clayey soil were obtained in the case of the magnitude of frictional strength and shear strength. That is, sand frictional strength was 25 ∿ 30 % less than shear strength but clayey soil shear strength was 20 % less.

Positive dilatancy occured during sand tests, at a lower magnitude in the compound specimen than in the simple specimen (Fig. 1-3(b)), indicating that negative pore water pressure was lower in the former. In other words, effective stress is less in the compound specimen and therefore, its frictional strength is less. On the other hand, in clayey soils, negative dilatancy occurred (Fig.1-5(b)). As the magnitude is lower in the compound specimen, smaller levels of possitive pore water pressure have built up. Accordingly, the effective normal stress in the compound specimen is greater, giving rise to its greater frictional strength.

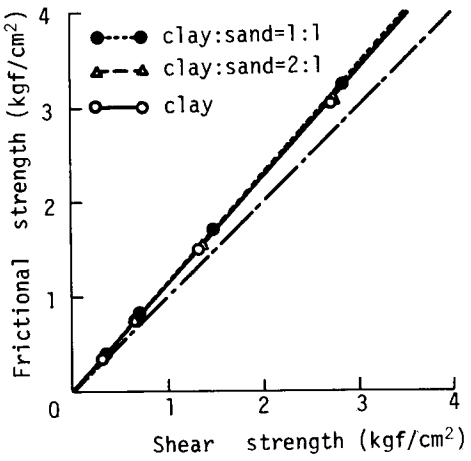

Fig. 1-8 The relationship between the frictional strength of the contact surface and the shear strength of clayey soil.

(3) The effects of the surface roughness of structural materials on the shear strength of the contact surface

Shearing characteristics of various compound specimens have been compared to those of simple specimens. The $\tau - \delta$ relationships are shown in Fig. 1-9 when the soil is Toyoura sand. When the materials are glass or mortar, the shear strength of the compound specimen was approximately 30 % less than that of the simple specimen because, in both cases, surface roughness are smaller than sand grain size. For rock which has a very rough surface, the shearing characteristics of both specimens were similar and their shear strengths were identical.

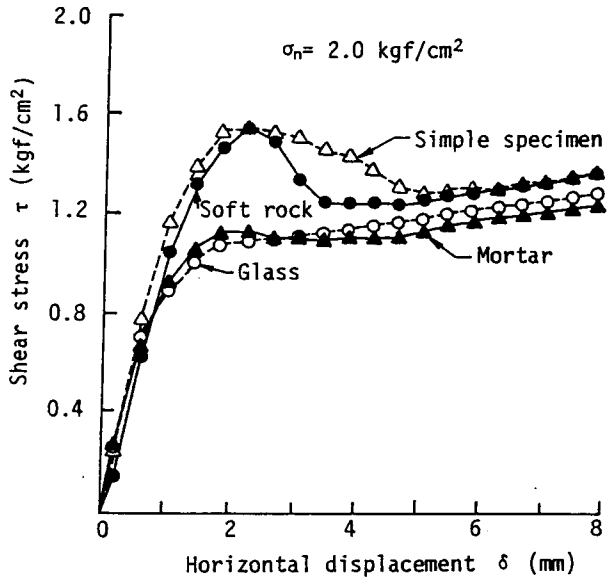

Fig. 1-9 The effects of surface roughness of different construction materials on shearing characteristics (sand).

Figure 1-10 shows the $\tau - \delta$ relationships when the soil material is clay. The shear strength of glass with its perfectly smooth surface is approximately 15 % less than that of the simple specimen. Mortar and soft rock have surfaces rougher than clay grain size and the shear strengths in compound specimens are approximately $10 \sim 15$ % greater. The

results imply that the shear strength at the contact surface depends on roughness of the construction material's surface, relative to the soil grain size, or, when the contact surface of the construction material is rougher than the grain size of the soil, shear strength is identical to or greater than that of the soil, but when the surface is smoother, the situation is reversed.

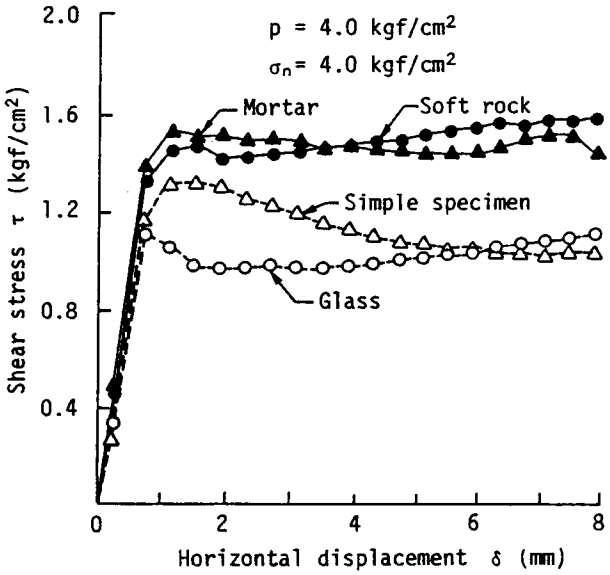

Fig. 1-10 The effects of surface roughness of different construction materials on shearing characteristics (clay).

1.4 The application of experimental results to the constitutive relationships of the joint element

No stress drop occurring after yield shear stress is reached in $\tau - \delta$ curves regardless of the soil material suggests that the joint element has an elasto-perfect plastic relationship.

The relationships between yield shear stress, τ, and normal stress, σ_n, are proportional for sand up to as high a normal stress as 8.0 kgf/cm^2. The ratios of the shear strength of the contact surface and

that of the sand are in the range of $0.70 \sim 0.75$, thus, the relationships between the friction angle of the contact surface, Ψ, and the internal friction angle of sand, ϕ, are

$$\Psi = \phi_J = (0.75 \sim 0.85)\phi \tag{1-4}$$

where, ϕ_J is the friction angle of the joint element.

For clay and cohesive granular soils, proportional relationships were obtained between the yield shear stress, τ_y, and consolidation stress, p. In the case of cohesive soils, yield shear stress corresponds to cohesion, C. The relationships between C and p were:

$$\left.\begin{aligned} \tau_y = C &= 0.31p \text{ (clay)} \\ &= 0.31p \text{ (clay : sand = 2 : 1)} \\ &= 0.35p \text{ (clay : sand = 1 : 1)} \end{aligned}\right\} \tag{1-5}$$

In addition, the ratios of the yield shear stress at the contact surface, C', and that of cohesive soils, C, are all approximately 1.2. Namely,

$$C' = C_J = 1.2C \tag{1-6}$$

where, C_J is the cohesion of the joint element. The results indicate that strength parameters, ϕ_J and C_J, of the contact surface can be calculated simply from the ϕ of sand or from the C of clay by Eq.1-1 or Eq.1-3, or from p by Eq.1-2 and Eq.1-3, if the ϕ or C of soil are available.

In practice, it is necessary to determine the shear strength of the contact surface between a structure with various surface roughnesses and soil with various grain sizes. The results in section 1.3 suggest a method to obtain strength parameters based on the relationships between the surface roughness and soil grain size. When the surface roughness of the structure is greater than the soil grain size, soil shear strength is the shear strength of the contact surface, and if surface roughness is less, soil shear strength should be multiplied by $0.70 \sim 0.75$. The an-

gle of internal friction is the strength parameter of sandy soil and the cohesion is the parameter of cohesive soil.

1.5 Conclusions

In order to obtain rational nonlinear constitutive relationships of the joint element which model the contact surface, a series of single-plane shear tests were performed. The results can be summarized as follows:

(1) The shearing characteristics of the joint element are of the elasto-perfect plastic type.

(2) The shear strength of the contact surface is not seriously affected by the shearing rate.

(3) The shear strength of the contact surface strongly depends on the magnitude of the construction material's surface roughness relative to the grain size of soil which comes in contact with it. That is, when the surface roughness of the structure is greater than the grain size of the soil, the shear strength of the soil is the shear strength of the contact surface. On the other hand, when the surface roughness is less, soil shear strength must be multiplied by $0.70 \sim 0.75$. In this case, the angle of internal friction becomes the strength parameter of sandy soil and cohesion the parameter of cohesive soil.

Chapter 1 references

1) Goodman R. E.: Methods of geological engineering, West Publishing Company, pp.320-330, 1976.

2) Potyondy J. G.: Skin friction between various soils and construction materials, Geotech. M.E., 1961.

3) Kishida T. and Y. Yoshimi: Frictional resistance between metal and sand, 12th Proc. Ann. Meeting of the Japanese Society of Soil Mechanics and Foundation Engineering (JSSMFE), pp.295-298, 1977, (in Japanese).

4) Kishida T., Y. Yoshimi and K. Ueki: Frictional resistance between metal and sand (No.2), 13th Proc. Ann. Meeting of JSSMFE, pp.437-440, 1978, (in Japanese).

5) Kishida T., K. Ueki and Y. Yoshimi: Frictional resistance between metal and sand (No.3), 14th Proc. Ann. Meeting of JSSMFE, pp.393-396, 1979, (in Japanese).

6) Ueki K., T. Kishida and Y. Yoshimi: Frictional resistance between metal and sand (No.4), 14th Proc. Ann. Meeting of JSSMFE, pp.397-400, 1979, (in Japanese).

7) Ishido M.: A study of the coefficient of friction between sand and pile surface, 24th Proc. Ann. Meeting of the Japan Society of Civil Engineers (JSCE), III-106, 1969, (in Japanese).

8) Ishido M., N. Seki and Y. Inoue: Characteristics of the friction between sand and the concrete wall, Proc. Ann. Meeting of Seibu branch of JSCE, 1971, (in Japanese).

9) Ishido M., N. Seki and A. Nomaguchi: A study of the skin friction, 27th Proc. Ann. Meeting of JSCE, III-117, 1972, (in Japanese).

10) Miyamoto J., H. Kishida and K. Kobayashi: Changes in the coefficient of friction due to the high constraining pressures, 10th Proc. Ann. Meeting of JSSMFE, pp.487-490, 1975, (in Japanese).

2. Separation and Sliding between Soil and Structure during Strong Ground Motion

2.1 General Remarks

There have been a number of studies dealing with the partial lifting-off of the base mat of nuclear reactor building. Uchida et al.[1] introduced the bilinear rocking-spring characteristic determined for static load using a three-dimensional finite element representation of the elastic half space. Kennedy et al.[2] and Takemori et al.[3] have also used this concept, but they approximated rocking-spring by the linear elastic theory of half space. In these works, however, the coupling of the vertical and rocking motion and also sliding phenomena were omitted. Wolf[4] detailed a rigorous procedure to determine the nonlinear impedance function of a rigid plate partially in contact with elastic half space, and to take partial sliding into consideration. Furthermore, Wolf and Skrikerud[5] examined the effects of the base mat lifting-off on the response of nuclear reactor building by using several approximate methods. However, Wolf's method is very complicated and is difficult to apply to the response analysis of structure embedded in subsoil. Tsuboi et al.[6] examined the possibility of the overturning of a tall building with the finite element method, taking separation at the contact surface into account but did not sliding.

The yielding of soil at the base of the structure may precede sliding or separation at the contact surface or may occur simultaneously with them. The introduction of nonlinear characteristics of soil into a dynamic analysis is therefore required. However, the nonlinearity has not been taken into account in any of the above methods.

The purpose of this chapter is to present a general analysis pro-

cedure of the dynamic soil-structure interaction problem including the possibilities of separation and sliding as well as the yielding of soil. Here, joint elements[7] are set along the contact surface.

Soil was assumed to be an elasto-perfect plastic material. First, the analytical procedures and problems in employing the joint element in a dynamic response analysis are outlined. Then, the effects of soil nonlinearity on the response of the system are examined and the stability of the structure against sliding is compared, using the levels of safety of the present and past methods.

2.2 A procedure to analyze nonlinear dynamic soil-structure interaction

(1) Interface modeling by the joint element

(a) The stiffness matrix of the joint element

Figure 2-1 shows a joint element constructed from four nodal points, I, J, K and L. Two pairs of nodal points, I-L and J-K, are assumed to occupy the same coordinates at the initial state, that is, when surfaces I-J and K-L are in contact. Behavior is expressed by the relative motion of both surfaces of the joint element. This is classified as follows:

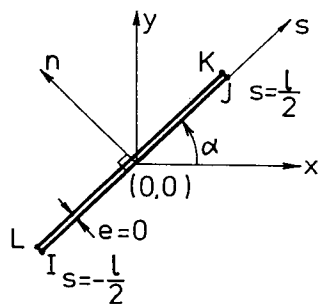

Fig. 2-1 The joint element configuration.

(i) parallel motion with the joint wall - sliding,

(ii) perpendicular motion to the joint wall - separation and contact,

(iii) rotational motion around the center of the element.

The deformation characteristics of the joint are determined by the stiffness of the shear direction, k_s, the normal

direction, k_n and the rotational component, k_ω. Since k_ω is expressed in terms of k_n, the constitutive relationships of the joint element is expressed by two parameters, k_s and k_n. The joint 'strain' defined at the center is:

$$\begin{Bmatrix} \gamma_0 \\ \varepsilon_0 \\ \omega \end{Bmatrix} = \begin{Bmatrix} \dfrac{u_K + u_L}{2} - \dfrac{u_I + u_J}{2} \\ \dfrac{v_K + v_L}{2} - \dfrac{v_I + v_J}{2} \\ \dfrac{v_K - v_L}{l} - \dfrac{v_J - v_I}{l} \end{Bmatrix} \tag{2-1}$$

where, γ_0 is the shear strain, ε_0, the normal strain, ω, the relative counterclockwise rotational angle of the joint wall, K-L to I-J, and u_i and v_i, the total displacement of node i in directions s and n, respectively.

The stress in the joint element is defined on the assumption that the nodal force is transmitted uniformly through the joint wall:

$$\left.\begin{aligned} \tau &= (F_{s,K} + F_{s,L})/l \\ \sigma &= (F_{n,K} + F_{n,L})/l \\ M_0 &= (F_{n,K} + F_{n,L})\,l/2 \end{aligned}\right\} \tag{2-2}$$

where τ is shear stress, σ, the normal stress, M_0, the moment caused by nodal point forces around the center of the joint, $F_{s,i}$ the nodal force component of s direction at nodal point i and $F_{n,i}$, the nodal force component of n at i.

Joint stress and strain are linked through the stiffness properties of the joint system:

$$\begin{Bmatrix} \tau \\ \sigma \\ M_0 \end{Bmatrix} = \begin{bmatrix} k_s & 0 & 0 \\ 0 & k_n & 0 \\ 0 & 0 & \dfrac{l^3}{4} k_n \end{bmatrix} \begin{Bmatrix} \gamma_0 \\ \varepsilon_0 \\ \omega \end{Bmatrix} \tag{2-3}$$

The stiffness matrix defining the relationship between nodal force and nodal displacement is easily obtained from Eqs. 2-1 and 2-3 and the relation $F_I = -F_L$ and $F_J = -F_K$:

$$\{F\}_{s,n} = [k]^J_{s,n}\{u\}_{s,n} \tag{2-4}$$

where, $\{F\}_{s,n}$ and $\{u\}_{s,n}$ are nodal force and displacement. They are written as:

$$\{F\}_{s,n} = \{F_{s,I}\ F_{n,I}\ F_{s,J}\ F_{n,J}\ F_{s,K}\ F_{n,K}\ F_{s,L}\ F_{n,L}\}^T \tag{2-5}$$

$$\{u\}_{s,n} = \{u_I\ v_I\ u_J\ v_J\ u_K\ v_K\ u_L\ v_L\}^T \tag{2-6}$$

The stiffness matrix $[K]^J_{s,n}$ is given by:

$$[K]^J_{s,n} = \frac{l}{4}\begin{pmatrix} k_s & 0 & k_s & 0 & -k_s & 0 & -k_s & 0 \\ & 2k_n & 0 & 0 & 0 & 0 & 0 & -2k_n \\ & & k_s & 0 & -k_s & 0 & -k_s & 0 \\ & & & 2k_n & 0 & -2k_n & 0 & 0 \\ & & & & k_s & 0 & k_s & 0 \\ & & & & & 2k_n & 0 & 0 \\ & & & & & & k_s & 0 \\ \text{Symmetric} & & & & & & & 2k_n \end{pmatrix} \tag{2-7}$$

The stiffness matrix $[K]^J_{s,n}$ is defined by the local coordinates (s,n), and when actually used, should be transformed to the global coordinate system.

(b) The constitutive relationships of the joint element

Based on the experimental results in chapter 1, stress-strain characteristics of the joint element are assumed to be those in Figs. 2-2(a) and (b) for normal and tangential components, respectively. Normal stress is not transmitted for $\varepsilon_0 > 0$ (separation) and a linear relation based on stiffness, k_n, is valid for $\varepsilon_0 \leqq 0$. Sliding will take place when the absolute value of shear stress reaches yield shear stress, τ_y, and

the linear shear stress-strain relation remains below this level. When separation occurs, the shear stress is not transmitted through the joint wall.

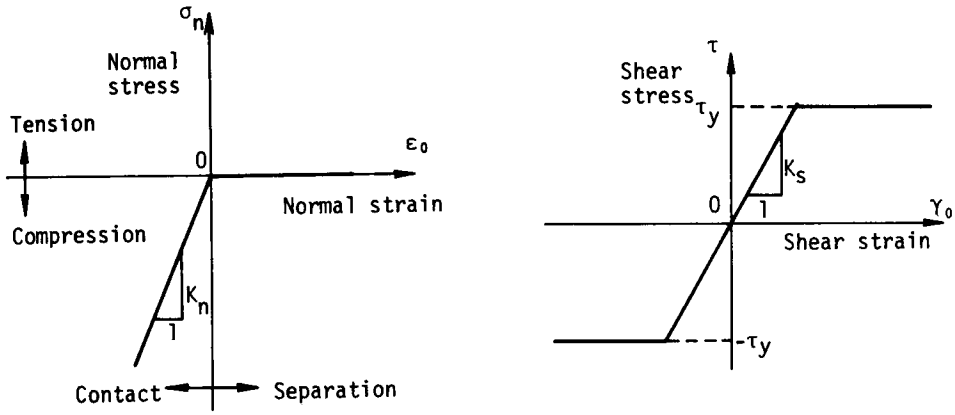

(a) Normal direction

(b) Tangential direction

Fig. 2-2 The constitutive relationship of the joint element.

Yield shear stress, τ_y, is determined as a function of normal stress according to the Mohr-Coulomb failure law:

$$\left.\begin{array}{lll} \tau_y = c_J - \sigma_n \tan\phi_J & \sigma_n \leqq 0: & \text{compression} \\ \tau_y = 0 & \sigma_n > 0: & \text{extension} \end{array}\right\} \qquad (2\text{-}8)$$

Spring coefficients, k_s and k_n, are related to the fictitious relative displacement at the soil-structure contact surface, which actually would not occur. Therefore, the influence of fictitious relative displacement on the response of the system cannot be overlooked when spring coefficients are small. Joint element deformation must be very small compared with solid element deformations. With this in mind, coefficients of adequate magnitude (Appendix 2-I) are:

For a shear spring coefficient;

$$k_s > \frac{\mu}{h} a \qquad (2\text{-}9)$$

For a normal spring coefficient;

$$k_n > \frac{2\mu + \lambda}{h} b \qquad (2\text{-}10)$$

where, μ and λ are the Lamé's constants and h, the height of the solid element. Arbitrary constants, a and b, prescribe the deformation of the joint element relative to that of the solid element. In general, the larger these constants are, the greater is the accuracy. However, an extremely large number is not efficient because the necessary time interval Δt decreases to a very small duration as the constants increase. In a soil-structure system, for example, good accuracy can be obtained when they are greater than $1 \sim 2$ for the structure element. Further concrete details concerning accuracy follow in section 2.3 (1).

(2) The constitutive relationships of soil

There are several constitutive relationships which are commonly used in soil mechanics, such as (i) the rigid-perfect plastic body[8], (ii) the elasto-perfect plastic body[9] and (iii) the strain-hardening body[10-12]. Considering the simplicity of the treatment in the numerical analysis and the conformity with the constitutive relationships of the joint element, soil is regarded as an elasto-perfect plastic body here. The Mohr-Coulomb failure law is adopted as the yield criterion. This relationship is given by the following equations 2-11 and in Fig. 2-3.

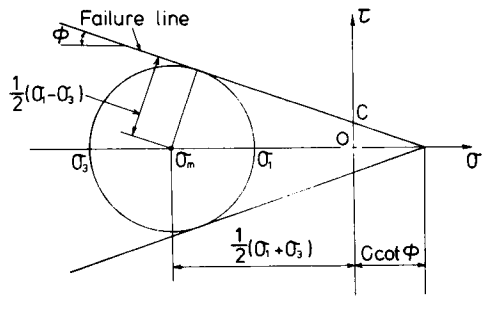

Fig. 2-3 The Mohr-Coulomb failure law.

$$\left.\begin{aligned} \tau_y &= c\cos\phi - \sigma_m \sin\phi \\ \sigma_m &= \frac{\sigma_1 + \sigma_3}{2} \end{aligned}\right\} \qquad (2\text{-}11)$$

where, τ_y is the yield shear stress, c and ϕ are the cohesion and the internal friction angle, and σ_1 and σ_3 are the maximum and the minimum principal stresses, respectively.

(3) The initial stress state

When yielding of soil or separation and sliding phenomena at the contact surface are included in a dynamic response analysis, the initial stress due to the gravity force must be taken into consideration as initial conditions. Initial stresses are obtained by solving the static problem, in which the external forces, $\{f_0\}$, is equivalent to the weight of the system, calculated from Eq. 2-12[13].

$$\{f_0\} = \int_V [N]^T \{p\} dv \tag{2-12}$$

where, $\{p\} = \{0 \quad -\rho g\}^T$ and ρ is mass density, g is the acceleration of gravity and $[N]$ is the shape function matrix. The superscript, T, indicates the transposition of a matrix and $\int_V dv$, the volumetric integral of the element.

(4) Numerical method for iterative solution

Constantpoulos et al.[14] have shown that the iterative scheme originally suggested by Seed and Idress[15] gives reasonable approximations of a rigorous nonlinear solution in the time domain for one-dimensional wave propagation problems, while the frequency domain algorithm of seismic response analysis restricts the solutions to linear ones. This scheme is a kind of the equivalent linearization method[16-18]. An alternative approximate method, known as the equivalent temporal damping method, has been implemented in a finite element digital computer code[19], which results in a piece-wise linear solution with time-varing damping and shear modulus properties determined by iteration for each element and each half cycle of response. Bieber and Hovland[20] have assessed the relative accuracy of two approximate methods by comparisons with exact numerical solutions.

A rigorous nonlinear dynamic analysis in the time domain, however, must be performed when a system is so strongly nonlinear as to exhibit separation and sliding at the contact surface and/or material nonlinearity of soil. Consequently, equation of motion governing the be-

havior of the system was integrated directly. The required interval of each step is of the order of 0.001 seconds.

The load transfer method analyzes nonlinear dynamic response. Since the method is iterative, it uses a constant stiffness matrix throughout the analysis, and CPU time is greatly reduced compared to other nonlinear analytical techniques, such as the Newton-Raphson method.

(a) Numerical computation by the load transfer method

The essential steps of the load transfer method are described below:

(i) Analyse the problem as an elastic one and compute the stresses in each element (both the joint and solid elements), to which the initial stresses present before the loading operation began are added.

(ii) At the end of step (i) it will be found that certain elements have yielded. As the system is nonlinear, the excess stress (the mobilized stresses minus the yield stresses) are eliminated without, however, permitting any point in the system to displace. In order to maintain an equilibrium "restraining forces" have to be temporarily applied to the system at this stage. In terms of finite element analysis such forces are evaluated element by element in the manner to be indicated.

(iii) As the restraining forces do not in fact exist, their effects have to be removed from the system by superposition of equal but opposite nodal forces. The system is now reanalyzed for the effect of such forces and the stresses computed are added to those pertaining at the end of step (ii) (when the excess stresses have been eliminated).

During the application of "de-restraining forces" the system behavior is again assumed to be elastic and when the stresses are computed, it will be found that the excess stresses may still develop. They will, however, be much reduced compared with the previous step.

(iv) If at the end of step (iii) the excess stresses are still exist, steps (ii) and (iii) are repeated until the excess stresses are reduced to be a negligible figure.

Figure 2-4 gives a schematic representation of this procedure. The modified external forces, the summation of the seismic external force and the de-restraining force, are the "quasi-external force", denoted by $P_{i,j}$ at the end of j-th iteration at time t_i. The quasi-external force is an external force to the system using the constant stiffness matrix.

(i) The displacement and the quasi-external force are converged to $u_{i-1,c}$ and $P_{i-1,c}$ at time t_{i-1} as shown in Fig. 2-4.

(ii) The first iterative approximation of the quasi-external force at time t_i is calculated as:

$$\left.\begin{aligned} P_{i,1} &= P_{i-1,c} + \Delta F_i \\ \Delta F_i &= F_i - F_{i-1} \end{aligned}\right\} \qquad (2\text{-}13)$$

where, F_i is the seismic external force at time, t_i. The corresponding displacement is $u_{i,j}$.

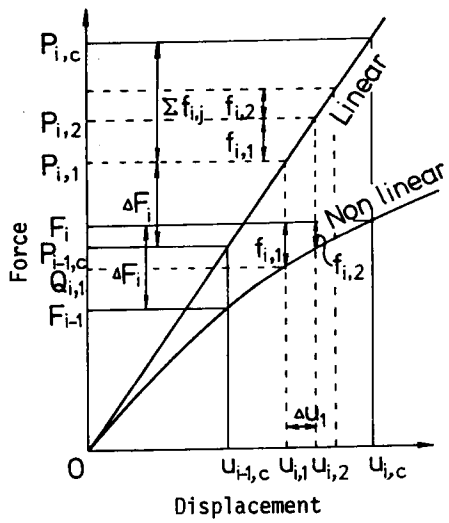

Fig. 2-4 The iterative process for load transfer method.

(iii) From the displacement, $u_{i,j}$, the de-restraining force, $f_{i,j}$, is calculated in the manner explained below.

(iv) The quasi-external force in the (j+1)th iteration is modified to $P_{i,j+1} = P_{i,j} + f_{i,j}$ and the displacement in the (j+1)th iteration $u_{i,j+1}$ is obtained from the equation of motion. As a result, the quasi-external force at time, t_i, is:

$$P_{i,c} = P_{i-1,c} + \Delta F_i + \sum_j f_{i,j} \qquad (2\text{-}14)$$

(b) The treatment of joint element nonlinearity

(i) The joint element is assumed to be a linear elastic system and nodal displacements at time $t = t_i$ are obtained from the equations of motion.

(ii) The nodal forces equivalent to the displacement-caused stresses are obtained from stiffness matrix.

(iii) Whether or not the prescribed constitutive relationships are satisfied is examined.

Sliding is taking place when

$$l\tau_y < lc_J - l\sigma_n \tan\phi_J \tag{2-15}$$

is satisfied. The de-restraining forces are obtained by subtracting the right term from the left term.

Separation is taking place when

$$l\,\sigma_n > 0 \tag{2-16}$$

is satisfied. The de-restraining forces are equal to $l\,\sigma_n$.

(c) The treatment of material nonlinearity of soil

(i) Assume the soil-structure system as a linear elastic system and obtain nodal displacements at time $t = t_i$ from the equations of motion. The stresses, σ_x, σ_y and τ_{xy}, for each element are calculated from the nodal displacements.

(ii) The maximum shear stress, τ_{max}, is estimated for each element by the equations:

$$\tau_{max} = \frac{\sigma_1 - \sigma_3}{2} \tag{2-17}$$

and

$$\begin{Bmatrix}\sigma_1\\ \sigma_3\end{Bmatrix} = \frac{\sigma_x + \sigma_y}{2} \pm \sqrt{\left(\frac{\sigma_x - \sigma_y}{2}\right)^2 + \tau_{xy}^2} \tag{2-18}$$

(iii) This maximum shear stress, τ_{max}, is compared to the yield shear stress, τ_y, obtained from Eq. 2-11. Elements for which $|\tau_y| < |\tau_{max}|$ are undergoing yielding. In this case, two kinds of failure modes can be considered, depending on the magnitude of the mean stress σ_m, as shown in Fig. 2-5. That is,

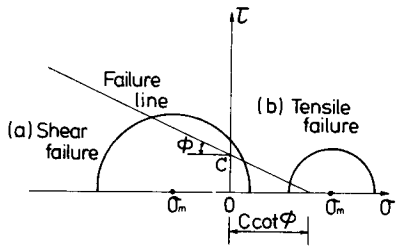

Fig. 2-5 Failure modes of soil.

(a) $\sigma_m \leqq c \cot \phi$: shear failure

(b) $\sigma_m > c \cot \phi$: tensile failure (2-19)

When an element exhibits shear failure, the de-restraining force, an additional external force making the linear and nonlinear systems equevalent, may be obtained as follows.

The stress state expressed by the Mohr's circle A in Fig. 2-6 in the case of a linear elastic soil must be reduced to keep it in contact with the failure line in the case of a nonlinear soil. Assuming that the mean stress, σ_m, and the direction, θ, of the principal stress remain unaltered, the resulting Mohr's circle becomes circle B in Fig. 2-6.

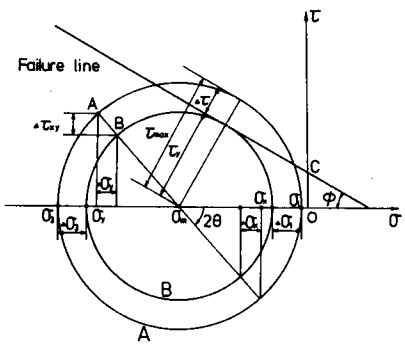

Fig. 2-6 Modification of Mohr's circle for shear failure.

Stress changes, $\{\Delta\sigma\}$, associated with the reduction of Mohr's circle from A to B are determined by:

$$\{\Delta\sigma\} = \begin{Bmatrix} \Delta\sigma_x \\ \Delta\sigma_y \\ \Delta\tau_{xy} \end{Bmatrix} = \begin{Bmatrix} -\Delta\tau \cos 2\theta \\ \Delta\tau \cos 2\theta \\ -\Delta\tau \sin 2\theta \end{Bmatrix} \tag{2-20}$$

$$\Delta\tau = \tau_{max} - \tau_y \tag{2-21}$$

The de-restraining forces, $\{f\}$, are given by the nodal forces which are equivalent in magnitude but have opposite sings to the stress changes given by Eq. 2-20. Namely,

$$\{f\} = -\int_V [B]^T \{\Delta\sigma\} dv \tag{2-22}$$

where, $[B]$ is the strain shape function matrix.

In case of element tensile failure, Mohr's circle A must be reduced to point P in Fig. 2-7. In this case stress chages, $\{\Delta\sigma\}$, are given by Eq. 2-23.

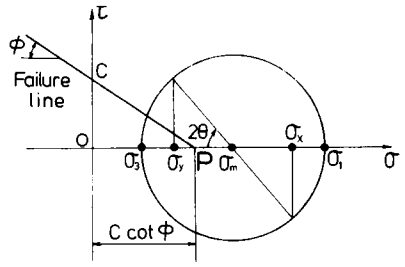

Fig. 2-7 Modification of Mohr's circle for tensile failure.

$$\{\Delta\sigma\} = \begin{Bmatrix} \Delta\sigma_x \\ \Delta\sigma_y \\ \Delta\tau_{xy} \end{Bmatrix} = \begin{Bmatrix} C\cot\phi - \sigma_x \\ C\cot\phi - \sigma_y \\ -\tau_{xy} \end{Bmatrix} \qquad (2\text{-}23)$$

The de-restraining forces, $\{f\}$, are obtained as above, but with Eq. 2-23 replacing Eq. 2-20. Once the $\{f\}$ are calculated, they are added to the external forces, $\{P\}$, and the computation proceeds by returning to step (i).

If the above method is used, systems with nonlinear constitutive relationships can be treated as linear systems with constant stiffness excited by quasi-external forces. The computation of the inverse stiffness matrix is required only at the first step of the response analysis and computation time is thus greatly reduced.

2.3 Dynamic response characteristics of the structure when either separation or sliding takes place

(1) Models and excitations

Figure 2-8(a) shows Model I, a structure resting on the ground surface. Model I is a typical reactor building of a nuclear power station in Japan. Three models make up Model I. In the first model, Model I-1, the soil is linear elastic and the joint elements have nonlinear constitutive relationships. In the second model, Model I-2, the soil is nonlinear and the joint elements again have nonlinear constitutive relationships. In the third case, Model I-LI, the soil is linear elastic but it has no joint elements, and is the ordinary linear model. The finite element mesh of Model I is shown in Fig. 2-8(b). Three joint elements are arranged along the contact surface between the structure

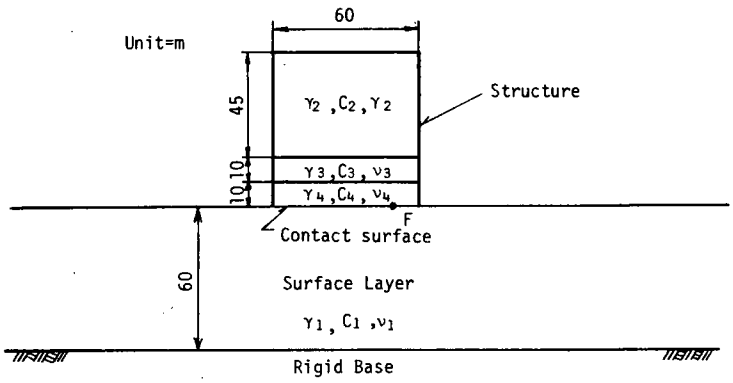

Fig. 2-8(a) Model I - A general view of soil-structure system.

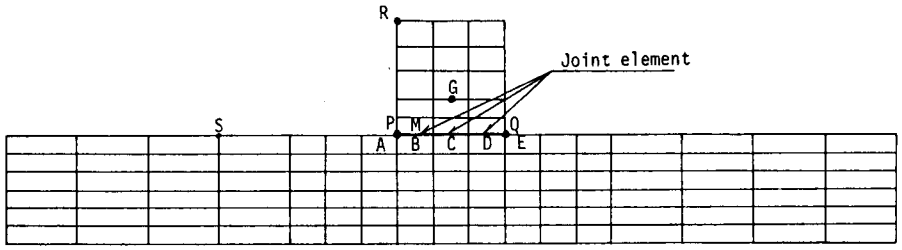

Fig. 2-8(b) Finite element mesh of Model I.

Table 2-1 Material properties of Model I.

	Unit weight (tf/m^3)	Shear wave velocity (m/sec)	Poisson's ratio	Damping factor	Cohesion (tf/m^2)	Friction angle (°)
Ground	γ_1=1.8	C_1=500	ν_1=0.4	h=0.2	10.0	30.0
Structure	γ_2=0.75 γ_3=1.7 γ_4=2.4	C_2=1720 C_3=1600 C_4=1600	ν_2=0.17 ν_3=0.17 ν_4=0.17	h=0.05	——	——
Joint element	Shear spring const. K_S=3.0x10^5 tf/m^3 Normal spring const. K_n=3.0x10^5 tf/m^3				5.0	30.0

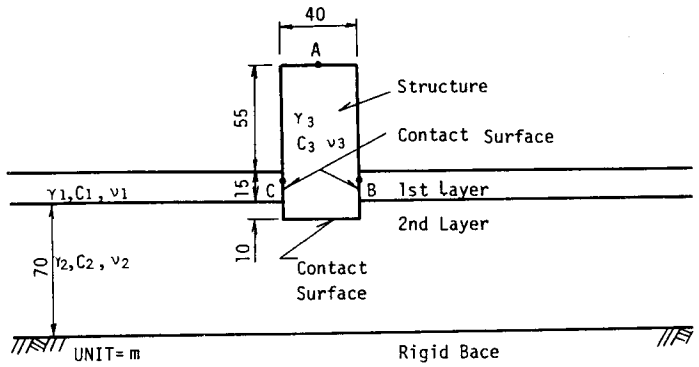

Fig. 2-9(a) Model II - A general view of soil-structure system.

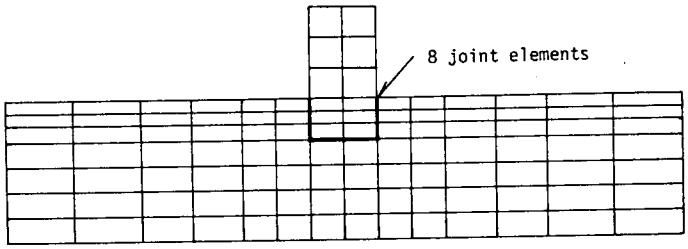

Fig. 2-9(b) Finite element mesh of Model II.

Table 2-2 Material properties of Model II.

	Unit weight (tf/m^3)	Shear wave velocity (m/sec)	Poisson's ratio	Damping factor
Ground	γ_1=1.8 γ_2=1.8	C_1=180 C_2=360	ν_1=0.4 ν_2=0.4	h=0.2
Structure	γ_3=2.4	C_3=1600	ν_3=0.17	h=0.05
Joint element	Shear spring const. $K_S=2.0\times10^5$ tf/m^3 Normal spring const. $K_n=2.0\times10^5$ tf/m^3 Cohesion C_j=10, 20 tf/m^2 Friction angle ϕ_j=0°, 30°			

and the ground. Model II, shown in Fig. 2-9(a), is a pier foundation of a long span bridge in which eight joint elements are arranged along the contact surface. The finite element mesh of Model II is shown in Fig. 2-9(b). The parameters of Model I are listed in Table 2-1 and of Model II in Table 2-2. The damping factor is 20 % of critical. While the damping factor of soil is usually assumed to be approximately 0.1, h=0.2 was adopted to include radiation damping. Although radiation damping is frequency-dependent, here it was assumed to be independent of frequency because step-by-step integration in the time domain is required.

As for mesh size, it has been ascertained that when the element length, l, in the direction of wave propagation is smaller than 1/8 of the wave length, L, it is sufficiently accurate[21]. When the element width, b, which is perpendicular is smaller than $L/2$ good results are also obtained[22]. Namely,

$$l \leqq \frac{L}{8} = \frac{V}{8f} \tag{2-24a}$$

$$b \leqq \frac{L}{2} = \frac{V}{2f} \tag{2-24b}$$

where, V is the wave velocity and f, the frequency. The predominant ground motion is due to the shear wave which propagates upward and downward in the ground of model. Taking Model I as the example and substituting V=500 m/sec and the maximum mesh size of the ground element l=10 m and b=40 m into the above relations, one can obtain f=6.25 Hz, or this mesh is accurate to a frequency of 6.25 Hz, covering the predominant frequency of the system and major portion of the range (1.0 ∿5.0 Hz) in the analysis (Fig.2-23). In the same way, the finite element mesh of Model II is accurate to 4.0 Hz. The fundamental natural frequency of Model II is 1.20 Hz.

These models are subjected to simultaneous excitation of NS and UD components of the El Centro (1940) accelerograms as well as to sinusoidal excitation. Sinusoidal input acceleration is multiplied by the

envelope function $E(t)$ given by:

$$\left.\begin{aligned} E(t) &= t \quad \text{for} \quad 0 \leqq t \leqq 1.0 \text{ sec} \\ &= 1.0 \quad \text{for} \quad t > 1.0 \text{ sec} \end{aligned}\right\} \tag{2-25}$$

That is, input reaches the specified amplitude 1.0 sec after the analysis begins. A rigid base is assumed beneath the ground surface layer and it is the source of the ground excitation.

Spring constants of $3.0\text{X}10^5\,\text{tf/m}^3$ have generally been used. Fictitious relative displacement at the contact surface resulted in increases of less than 2.4 % maximum response acceleration, 3.0 % velocity and 3.3 % displacement, at the center of gravity of the structure, when Model I-LI and a check model with joint elements in linear constitutive relationships and linear elastic ground were subjected to the El Centro accelerograms. The value, $3.0\text{x}10^5\,\text{tf/m}^3$, corresponds to 4.8 of a in Eq. 2-9 and 1.9 of b in Eq. 2-10 for the structure element where h=10 m, $\mu=6.27\text{x}10^5\,\text{tf/m}^2$ and $\lambda=3.14\text{x}10^5\,\text{tf/m}^2$ and to 69.1 of a and 11.5 of b for the ground element where h=10 m, $\mu=4.34\text{x}10^4\,\text{tf/m}^2$, and $\lambda=1.73\text{x}10^5$ tf/m^2. The time interval of computation Δt is 0.002 sec.

To verify the effectiveness of the load transfer method for a nonlinear dynamic response analysis, numerical computations of the three models, Model I-LI, Model I-1 and Model I-2, were carried out on a FACOM M-200 computer system (GIBSON-0.106 micro seconds). CPU times were about 400 seconds. The duration of these analyses was 10 seconds (5,000 steps). Convergence was obtained after a few iterations. By comparison, it takes 1.69 seconds to form the stiffness, damping and mass matrices, to add these matrices and to solve the inverse matrix of the added matrix. As a result, about 8,500 seconds are necessary to carry out the 5,000 analysis steps by the step by step method, such as the Newton-Raphson method, in which it is necessary to reform the stiffness matrix and to solve the inverse matrix at each time step. Consequently, the load transfer method is extremely efficient to analyze nonlinear dynamic

response.

(2) Response to sinusoidal excitation

(a) A response analysis of Model I-1

Figure 2-10 shows the amount of sliding at the contact surface and displacement at the center of gravity (CG) of the structure for the case of $\phi_J=0°$ and the horizontal sinusoidal excitation of 200 gal. The displacement at the CG of the linear system without the joint element is denoted by the smooth curve. The symbols ● and ○ correspond to sliding and displacement at the CG, respectively. Both the magnitudes of sliding and displacement decrease with increasing frequency and the difference between them is kept almost constant when frequency varies. This implies that sliding will occur when the structure is inclined at a specific angle, whereas rocking motion is predominant in the linear system. Sliding disappears beyond a specified frequency for a given excitation level. To clarify the effect of excitation level on sliding, the relationship between the sliding magnitude and acceleration amplitude is examined in Fig. 2-11. The excitation is sinusoidal at a frequency of 5 Hz. It is obvious that the relative displacement at the CG is almost proportional

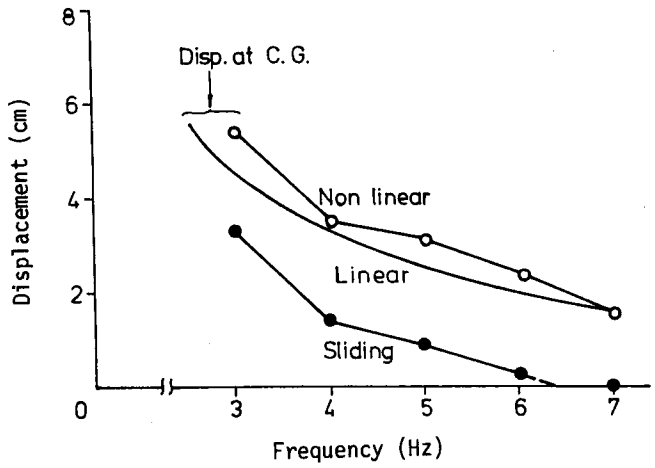

Fig. 2-10 Frequency dependence of displacement at the center of gravity, and sliding at the interface due to horizontal sinusoidal excitation ($\phi_J=0°$, excitation amplitude: 100 gal).

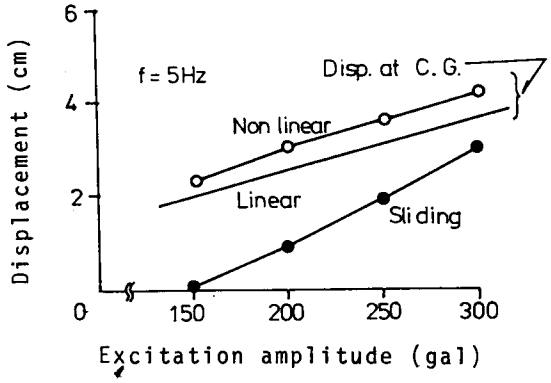

Fig. 2-11 Dispalcement at the center of gravity and sliding at the interface due to sinusoidal excitation (Frequency: 5 Hz).

to the excitation level. Sliding does not occur up to an excitation amplitude of 150 gal and sliding magnitude is proportional to the increment of excitation amplitude above the critical value. This implies that sliding will occur when the excitation force exceeds a certain threshold. Table 2-3 lists the maximum response of acceleration and displacement at the CG, the occurrence of sliding or lifting off and the maximum and minimum compressive stresses at point F in Fig. 2-8(a) for various excitation levels with fixed frequency of 5 Hz, in the case of $\phi_J=30^\circ$. Sliding of the whole structure with respect to the ground did not take place, and local sliding has occured only because the shear stress generated at the contact surface reached the local yield shear stress which depends strongly on the position.

Lifting off and overturning stability were also examined. Lifting off begins when the normal stress at the structure base vanishes. It does not appear, however, even at an input excitation of 400 gal, at which normal stress would still be compressive. In addition, the same investigation carried out at an excitation level of 300 gal and a frequency of 3 Hz resulted in no lifting off or sliding at all.

Table 2-3 Responses to sinusoidal excitation (Model I-1, ϕ_J=30°, frequency: 5Hz).

Excitation amplitude (gal)	300	350	400
Maximum acceleration at the center of gravity (gal)	358	434	611
Maximum displacement at the center of gravity (gal)	4.6	5.4	6.1
Sliding at the contact surface	No occurrence	Partially occurred	Partially occurred
Lifting off	No occurrence	No occurrence	No occurrence
Pressure at point F (tf/m^2) Maximum	99.1	105.6	111.8
Pressure at point F (tf/m^2) Minimum	23.2	16.9	10.9

(b) A response analysis of Model II

Figure 2-12 compares the displacement at the top of the structure (point A in Fig. 2-9(a)) for the case of ϕ_J=30° and a 300 gal excitation level. The response of the nonlinear system is greater than that of the linear system for frequencies less than 6 Hz because there is sliding between the side wall of the structure and the soil. Separation between the side wall and the soil near the ground surface occurs at 2 Hz, and then displacement increases to a level 30 % greater than that of the linear system. In the linear system, structural motion is so strongly restrained by the surrounding soil that the response is less than that of a nonlinear system with joint elements, especially in the low frequency range.

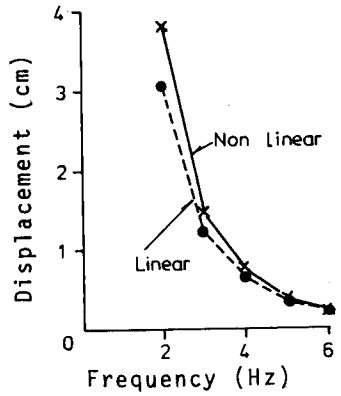

Fig. 2-12
The displacement of a structure at point A due to horizontal sinusoidal excitation (ϕ_J=30°, excitation amplitude: 300 gal).

The results of the nonlinear response analysis are listed in Table 2-4. The frequency of excitation is 2 Hz and the amplitude varies. The number in parentheses are the maximum acceleration and displacement of the linear system at point A and their percentages with respect to the nonlinear case. As the input level increases, the linear analysis

increasingly under estimates the system's response. The ratio of the linear case to the nonlinear case is not significantly affected by the input level or by the amount of separation at point B. Therefore, the structural responses become markedly nonlinear when sliding between the structure wall and soil takes place.

Table 2-4 Response to sinusoidal excitation (Model II, ϕ_J=30°, frequency: 2 Hz).

Excitation amplitude (gal)	200	300	400
Maximum acceleration at point A (gal)	378 ($^{319}_{84.3}$)	576 ($^{478}_{83.0}$)	793($^{637}_{80.4}$)
Maximum displacement at point A (cm)	2.43($^{2.09}_{84.4}$)	3.74($^{3.13}_{83.7}$)	5.19($^{4.17}_{80.4}$)
Sliding at point B (mm) Separation at point B (mm)	1.2 0	2.1 0.15	5.6 1.39

(3) Responses to seismic excitation

(a) A seismic response analysis of Model I-1

Figure 2-13 shows the horizontal displacement at point Q (Fig. 2-8(b)), where both sides of the structure and the soil share the same point before shaking begins. The solid line indicates the displacement of the side of the structure, and the broken line that of the soil. The relative displacement between the soil and structure increases from 1.7 to 2.5 sec, and after this period the structure vibrates at a constant residual deformation. In the figure, the displacement of the linear system is shown by the irregular broken line. While structural displacement increases with sliding, the soil displacement is almost identical to that in the linear system. This figure shows that the values adopted as the spring constants of the joint element are adequate to maintain sufficient accuracy because nonlinear and linear analyses are almost coincidental before sliding occurs.

Figure 2-14 illustrates the hysteresis loop for shear direction at point F. Point S denotes the start and E, the end of the analysis. At

the contact surface, the stress-strain relation is linear until 1.71 sec and sliding in the positive direction continues until 1.94 sec. Sliding

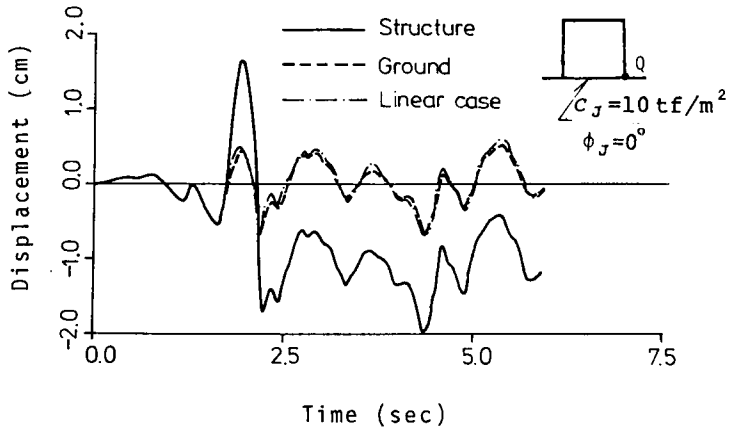

Fig. 2-13 Horizontal displacement at point Q due to El Centro accelerograms.

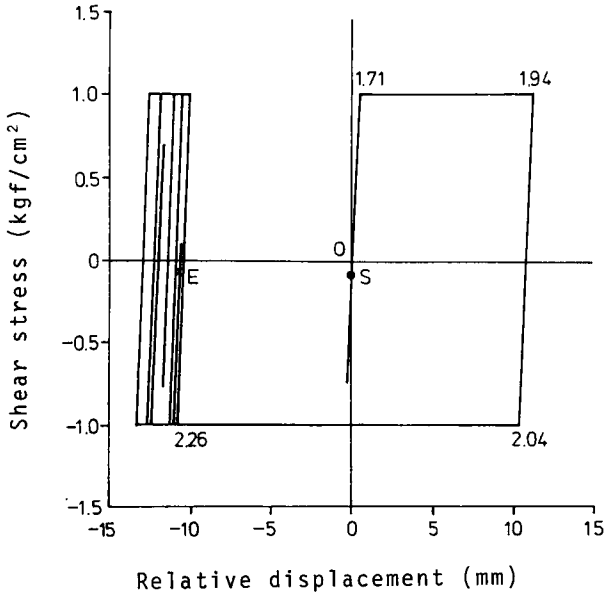

Fig. 2-14 A hysteresis loop of shear direction at point F.

in the inverse direction takes place at 2.04 sec, after which it gradually increases in the negative direction. The residual relative displacement is 11 mm.

Although the results calculated in the case where $\phi_J=30^\circ$ and $c_J=10$ tf/m^2 is not shown, neither sliding and lifting-off occurs. The minimum normal stress of 38.6 tf/m^2 at the structure base (point F) is generated at 2.2 sec, and the shear stress is 19.0 tf/m^2. Therefore, if the internal friction angle is less than 13.1°, local sliding may take place but only in the vicinity of point F.

(b) A seismic response analysis of Model II

The hysteresis loop at point B of Model II is shown in Fig.2-15 when $\phi_J=0^\circ$. Figure 2-15(a) is for the tangential direction and (b) the normal direction. Separation occurs at 2.19 sec and shear stress suddenly falls to zero (the vertical straight line in Fig. 2-15(a)). It continues until 2.37 sec, under zero shear stress. During this period, relative displacement between soil and structure is great in the vertical direction. Separation at point C (opposite B) occurs from 1.86 to 2.09 sec and from 2.70 to 2.79 sec. The contact surface between the structural wall and the soil separates repeadedly from 1.86 to 2.79 sec due to the rocking motion of the structure.

Figure 2-16 is the hysteresis loop at point C of Model II when $\phi_J=30^\circ$. Separation at this point takes place from 1.88 to 2.02 sec and the amount of sliding is remarkable during this period. The slope of the hysteresis curve of shear direction varies within the period between 2.14 and 2.24 sec, because fluctuations in normal stress over time result in changes yield shear stress of the contact surface. Separation and sliding between the structural base and the soil did not occur when $\phi_J=0^\circ$ or 30°.

The horizontal displacement at the top of the structure of Model II (point A in Fig. 2-9(a)) is shown in Fig. 2-17. The solid line is the linear case, the irregular broken line is the case where $\phi_J=0^\circ$ and the

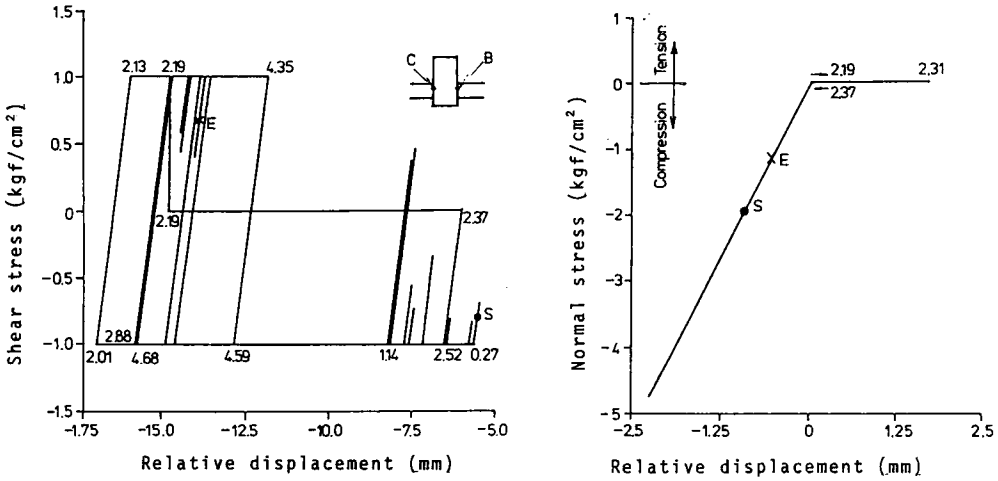

(a) Tangential direction (b) Normal direction

Fig. 2-15 A hysteresis loop at point B (Model II , ϕ_J=0°).

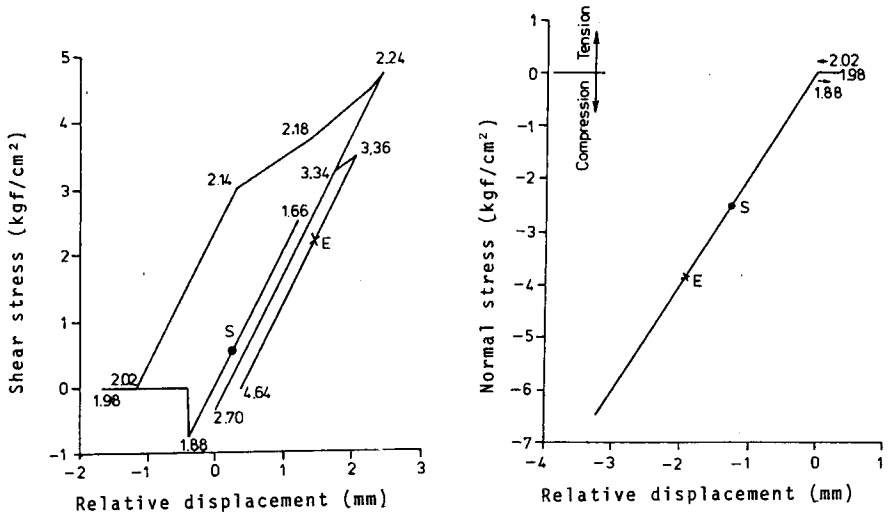

(a) Tangential direction (b) Normal direction

Fig. 2-16 A hysteresis loop at point C (Model II , ϕ_J=30°).

broken line when ϕ_J=30°. The displacement when ϕ_J=0° is 15 ∿ 30 % greater at each peak than that of the linear case, and the same is true for response acceleration. This means that an analysis assuming perfect bonding at the contact surface between the structure and soil does not correctly estimate the magnitude of structural responses, because the subsoil restricts structural movement too much.

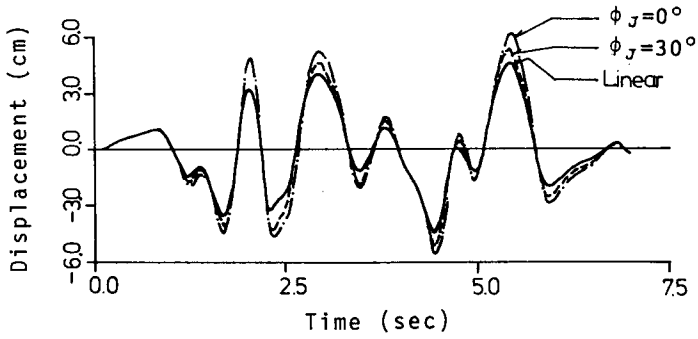

Fig. 2-17 Horizontal displacement at the top of structure (Model II , point A).

2.4 Seismic response analyses which include soil material nonlinearity

(1) The influence of soil nonlinearity on system's responses

(a) Yielding of soil due to structural motion

The shaded areas in Fig. 2-18 show the elements which yielded during the time period indicated in the upper-left-hand corner of each figure when Model I-2 is subjected to the El Centro accelerograms. It is clear that the yield zone is apt to extend obliquely downward from the bottom edges of the structure, and that the soil beneath the structure is relatively stable. This yield zone almost coincides with the area where the initial shear stress is large due to the gravity force. Figure 2-18(c) compares yield zones in the case of a model from which the structure has been removed.

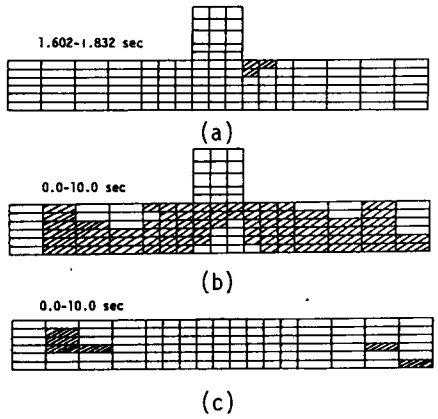

Fig. 2-18 The failure zone of the ground.

(b) Sliding of the structure and ground strain

Figure 2-19 shows hysteresis curves of the shear stress and relative displacement at the contact surface of joint element M, (Fig. 2-8(b)). Figure 2-19(a) is for Model I-1 and (b) for Model I-2. Point S designates the start and E, the end of the analysis. Hysteresis curves which are not parallel to the straight line that crosses S, represent the period when sliding occurs. The slope of these portions changes with variations in yield shear stress, τ_y, which in turn depends on normal stress, σ_n. Sliding is dominant from 2.2 to 2.3 sec (③∿④ in Figs. 2-19(a) and (b)) in both models. The structure slid 13 mm relative to the ground in Model I-1 and 2.6 mm in Model I-2, the total of local sliding plus sliding of the whole structure. The magnitude of the latter is approximately 11 mm in Model I-1 and 1.2 mm in Model I-2. That is, the magnitude of sliding in linear elastic ground is nearly ten times greater than that in nonlinear ground, when other properties and variables of the model and the excitation are kept constant.

Figures 2-20(a) and (b) show the maximum amplitude of shear stress, τ_{xy}, and shear strain, γ_{xy}, beneath the structure (elements A, B, C, D and E in Fig. 2-8(b)) of the three models. The magnitude of stress in Model I-2, where the ground is assumed to be of a nonlinear material, is smaller than that in Model I-1. On the other hand, the magnitude of strain of Model I-2 is greater than that of Model I-1, as would be ex-

pected. The same tendencies are found for stresses, σ_x, σ_y, and strain, ε_x. However, the magnitude of strain, ε_y, in Model I-2 is twice as large as that in Model I-1. This large strain amplitude is probably caused by the yielding of the ground. Figure 2-21 is the hysteresis loop of τ_{xy} and γ_{xy} of soil element C of Model I-2. The ductility factors of elements A ∿ E, tabulated in Table 2-5, are obtained from these loops.

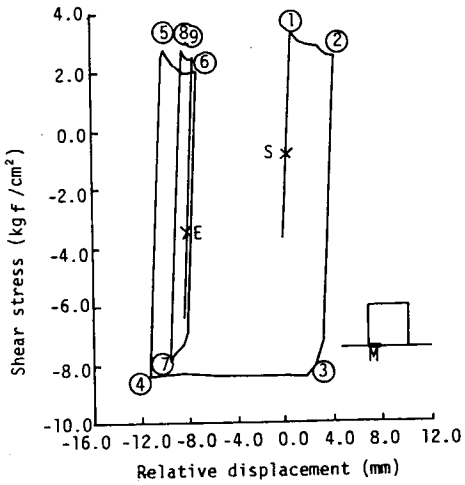

(a) Model I-1

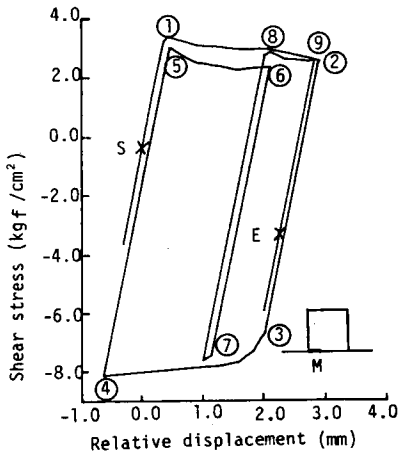

(b) Model II-2

Fig. 2-19 A hysteresis loop of shear component of joint element M.

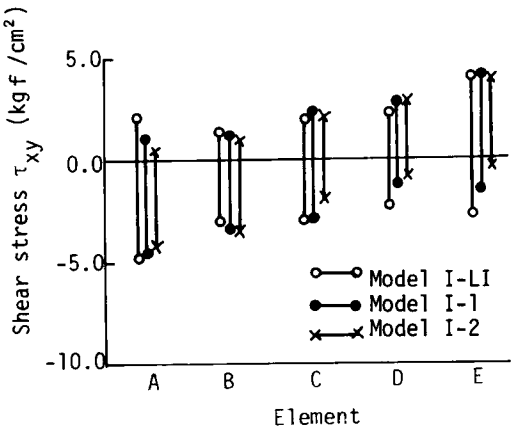

Fig. 2-20(a) Shear stress amplitude in element A∿E.

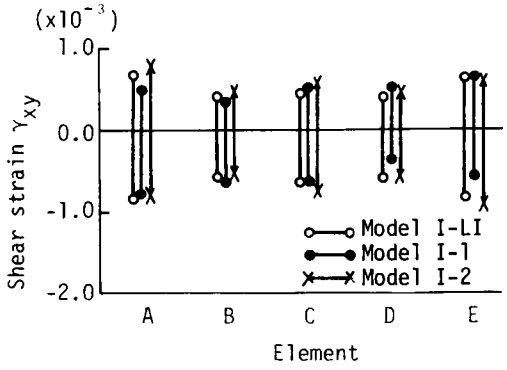

Fig. 2-20(b) Shear strain amplitude in element A∿E.

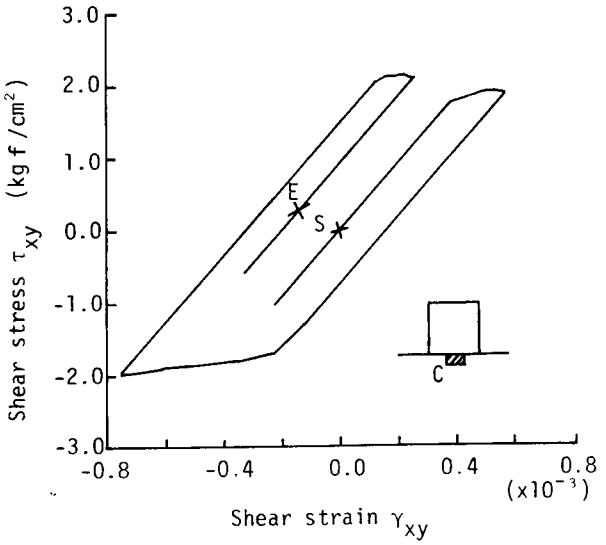

Fig. 2-21 A hysteresis loop of τ_{xy}-γ_{xy} of element C.

Table 2-5 Ductility factors of the ground beneath the structure (Model I-2).

Element	A	B	C	D	E
Ductility factor	3.4	1.7	2.0	2.5	3.0

(c) Maximum responses of the ground and structure

Table 2-6 lists the absolute maximum values of the ground surface (point S in Fig. 2-8(b)), the center of gravity of the structure (point G) and the top of the structure (point R). The horizontal displacements are almost the same at individual points of observation regardless of the model used. However, the vertical displacements of Model I-2 are greater than those of the other two models at each point.

Table 2-6 Maximum response of the ground and structure.

Point	Model	Displacement (cm)		Velocity (cm/sec)		Acceleration (gal)	
		horizontal	vertical	horizontal	vertical	horizontal	vertical
S	Model I-LI	3.92	0.19	42.2	4.0	576	185
	Model I-1	3.92	0.18	42.8	4.0	577	185
	Model I-2	3.95	0.25	37.0	4.0	542	186
G	Model I-LI	6.79	0.57	70.5	7.6	811	179
	Model I-1	7.00	0.53	63.0	7.6	683	178
	Model I-2	6.70	0.79	56.0	7.8	663	178
R	Model I-LI	9.36	1.25	103.2	16.9	1105	293
	Model I-1	9.33	1.12	91.2	15.6	957	262
	Model I-2	9.13	1.46	83.4	15.5	855	259

At the ground surface (point S), horizontal velocity and acceleration of Model I-2 are less than the corresponding values of Model I-1 and Model I-LI. At both points G and R, the response values are reduced as the model changes from LI to 1 to 2. On the other hand, vertical velocity and acceleration are almost identical for all three models, although the response of Model I-LI at point R is somewhat greater than those of the other models. The 683 gal maximum response acceleration in Model I-1 corresponds to Model I-LI, the linear model, when h=0.26. This implies that the energy dissipated during sliding at the contact surface was the cause of the increase of the damping factor by 0.06. The 663 gal maximum acceleration in Model I-2 corresponds to the linear model when h=0.27. The 0.07 increment in damping factor is due to the energy dissipation caused by the sliding at the contact surface and the yielding of soil. Most of the energy dissipated is caused by hysteresis damping

because sliding magnitude is very small when compared to the degree in Model I-1.

Figures 2-22(a) and (b) are the horizontal and vertical response displacement curves, respectively, of the ground at point P of Model I-2. In the figures, a residual displacement arose at approximately 2.0 ∿ 2.5 sec. Considering the direction of this displacement, it follows that from this point plastic deformation of the ground takes place towards the left and downward. At the opposite site, point Q, plastic deformation takes place towards the right.

When residual displacement of the ground just beneath the structure is considered, the structurally induced settlement is about 3 mm.

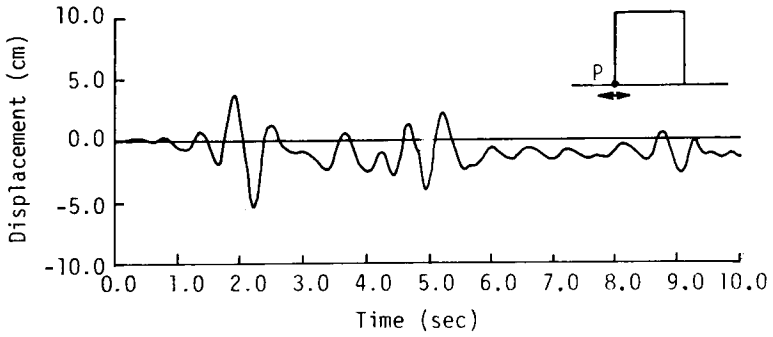

(a) Horizontal displacement at the ground side

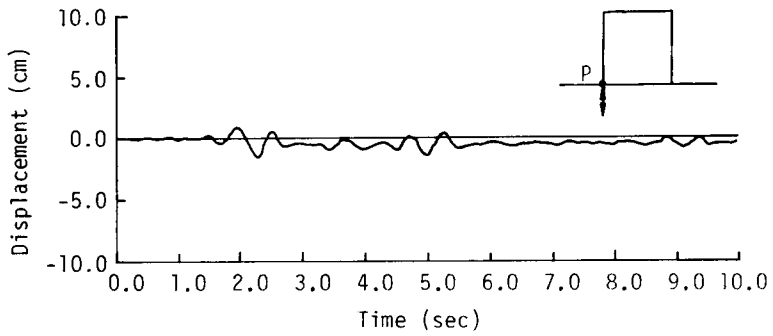

(b) Vertical displacement at the ground side

Fig. 2-22 Displacement at point P of Model I-2.

Figure 2-23 shows the instructure response spectrum[23] (IRS) at point R, where the damping factor is assumed to be 2 % of critical. The

irregular broken line is of Model I-1 and the solid line Model I-2. In general, the IRS of Model I-2 gives the lowest response value, a tendency remarkable when the period is short. Comparing the IRSs of Model I-1 and Model I-LI, both have almost the same response values in the long and middle period ranges, but in the short less than 0.22 sec, the IRS of Model I-1, in which sliding occurs, is greater than that of Model I-LI. This tendency is in accordance with what Wolf et al.[24] and Kennedy et al.[25] found when applying their own techniques to analyses of a nuclear reactor building, which consider sliding and "lifting-off".

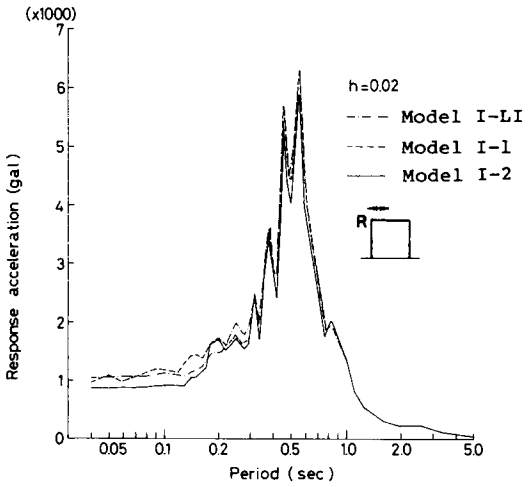

Fig. 2-23 The instructure response spectrum at point R.

2.5 Safety of the structure against sliding

(1) A definition of safety against sliding

Safety of the whole structure against sliding is usually checked by applying a static seismic force to the structure's center of gravity. In this case, the safety factor is given by the ratio of the static yield shear force F_{ys} to the static shear force F_s, F_{ys}/F_s. This ratio is referred to as static safety factor (SSF) and is given by the following

equation.

$$SSF = \frac{C_J B + W \tan \phi_J}{W \frac{\alpha}{g}} \tag{2-26}$$

where, W is the weight of the structure, B, the width of the structure base and g, the acceleration of gravity. C_J and ϕ_J are the cohesion and friction angle of the joint element, respectively. α, the maximum horizontal response acceleration at the center of gravity of the structure, obtained from a dynamic analysis of a linear model.

Safety of the whole structure against sliding under the dynamic excitation is defined as the ratio of yield shear force F_y to mobilized shear force F, F_y / F, along the contact (sliding) surface under consideration. Safety against sliding is discussed in terms of this ratio, which is referred to as the total safety factor (TSF)[26]. Namely,

$$TSF = \left| \frac{\sum_{j=1}^{N} \tau_{yj} l_j}{\sum_{j=1}^{N} \tau_j l_j} \right|_{\text{min.T}} \tag{2-27}$$

where, τ_{yj}, τ_j and l_j are the yield shear stress, the mobilized shear stress and the length of joint element j, respectively. min.T means the minimum value of the absolute value with respect to analyzed time.

(2) Dynamic stability of the structure against sliding

In order to investigate the dynamic stability of the structure against sliding, Model I-2 was subjected to the simultaneous horizontal and vertical excitations of three different accelerograms, the El Centro NS and UD components (Imperial Valley Earthq., 1940), the Jet Propulsion Laboratory (J.P.L.) S82E and UD components (San Fernando Earthq., 1971) and the Hachinohe EW and UD components (1968 tokachi-oki Earthq., 1968). Table 2-7 lists the maximum amplitudes and predominant frequency of the original accelerograms. The amplitudes have been modified for use in seismic response analyses.

Table 2-7 Maximum acceleration and predominant frequency of excitation accelerograms.

	El Centro		J.P.L		Hachinohe	
	NS	UD	S82E	UD	EW	UD
Maximum acceleration (gal)	342	206	208	126	203	96
Predominant frequency (Hz)	1.15	8.55	2.88	2.95	0.83	1.25

Based on the chapter 1 the strength parameters for soil are c=0.0 tf/m^2 and ϕ=40° and for the joint element c_J=0.0tf/m^2 and ϕ_J=30°, respectively. Figure 2-24 shows the relation between TSF and the maximum horizontal response acceleration at the center of gravity of the structure. The static safety factor is a hyperbola with respect to the response acceleration. It is shown in Fig. 2-24 as a solid line. The symbols ↓ are the response accelerations where the whole structure slid, i.e., TSF=1.0. TSF and SSF are exactly alike. This means that the safety

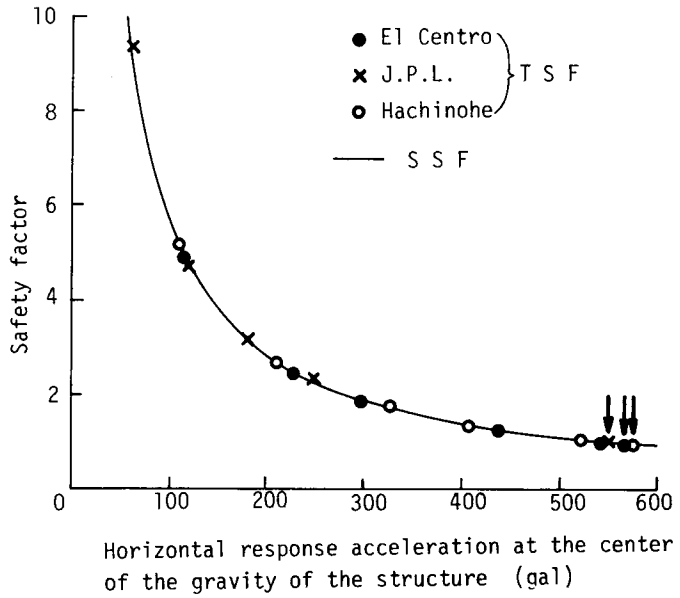

Fig. 2-24 The relationship between safety factors against sliding, and the maximum response acceleration at the center of gravity of the structure.

against sliding can be estimated by the static method as long as maximum response acceleration can be accurately obtained. This also indicates that effects of vertical excitation on safety can be disregarded because TSFs are obtained by applying both horizontal and vertical excitation, while SSF is calculated from only horizontal acceleration. Figure 2-24, however, does not imply that the factors are identical for the same excitation. Instead, they differ from each others as the level of excitation increases because SSF is calculated from a linear model whereas TSF is affected by soil nonlinearity and by local sliding. For practical purposes, it is very important to clarify the differences between them. For this purpose, Fig.2-25 plots the SSF:TSF ratio against input acceleration amplitude. As the latter increases, the ratio decreases. Overestimation of response acceleration in the linear model results in lower safety factors than there actually must be. The symbols ↓ indicate amplitudes at which TSF=1.0, below which SSF, however, is less than 1.0.

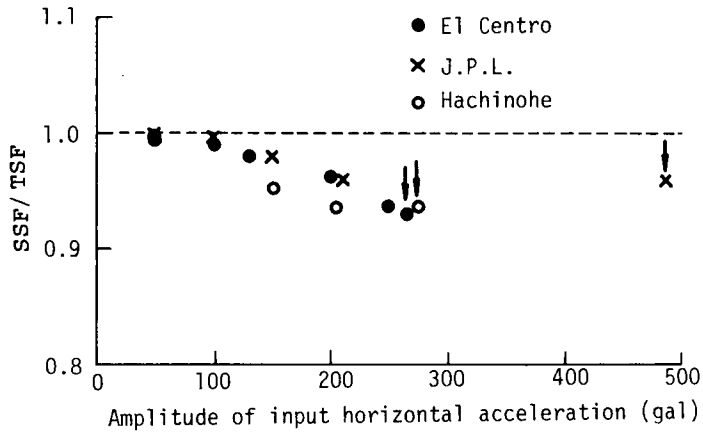

Fig. 2-25 The relationship between total and static safety factors.

Amplitude of input acceleration where SSF=1.0 are 245 gal, 257 gal and 468 gal for the El Centro, the Hachinohe and the J.P.L. accelerograms, respectively. For these amplitudes, the structure is still stable and TSFs are:

$$\left.\begin{array}{ll} TSF=1.07 & \text{for El Centro} \\ =1.04 & \text{J.P.L.} \\ =1.06 & \text{Hachinohe} \end{array}\right\} \qquad (2\text{-}28)$$

In conclusion the safety of a structure against sliding is apt to be low when estimated statically by the seismic force obtained from a linear model. However, SSF and TSF differ less than 10 % and SSF is accurate enough to check the structural stability as a first approximation.

2.6 Conclusions

A method has been presented to analyze seismic responses of a soil-structure interaction system, considering the material nonlinearity of soil as well as separation and sliding at the soil-structure contact surface. The seismic responses of two models illustrate the method's applicability in actual systems and clarify the effects of sliding and separation on dynamic stability.

The influence of soil nonlinearity on the system's response and on safety against sliding have also been discussed in detail. From the analyses presented, the following can be concluded:

(1) The load transfer method adopted to analyze nonlinear seismic response greatly reduces CPU time in comparison with other nonlinear analytical techniques. It is an extremely effective method to analyze nonlinear seismic responses.

(2) Assuming perfect bonding between soil and structure, the structure's motion is restricted by the surrounding subsoil and the analysis may not estimate the actual response correctly.

(3) There is a specified frequency, dependent on excitation level, above which separation and sliding do not/cannot occur. Separation and sliding increases as the frequency decreases below this level. Therefore, in any discussion of sliding and separation, careful consideration

should be paid to seismic excitations containing long period components.

(4) From the seismic response analysis of a soil-structure system, in which the soil is assumed to be elasto-perfect plastic, yielding extended over the whole ground area. The occurrence of yielding preceded that of local sliding between the structure and ground.

(5) The nonlinear behavior of the ground reduces the response of the system. Reduction of 3 ∿ 5 % (20 ∿ 100 gal) in horizontal acceleration and 10 ∿ 15 % (5 ∿ 8 kine) in horizontal velocity are reported in this model as opposed to a linear ground model. The sliding magnitude of the linear ground model is nearly 10 times greater than that of the nonlinear one. Nonlinear behavior of the ground was also examined using an instructure response spectrum. Ground nonlinearity generally reduced the response spectrum especially in short period range.

(6) When safety of whole structure was considered, a low safety factor was estimated when it was checked by applying the static force. However, safety factors differed by less than 10 % when obtained by the static method and the dynamic method. The static method is therefore a sufficient first approximation of a structure's stability against sliding.

Finally, ground nonlinearity reduced the response of the system and increased the safety of the structure against sliding, suggesting a basis for more rational and economical design. The method developed here provides a useful tool to examine such problems.

Chapter 2 references

1) Uchida K., T. Miyashita and S. Nagata: Earthquake response analysis of a nuclear power plant building with a circular basemat, Annual Report, Kajima Institute of Construction Technology, No.21, pp.673-678, 1973, (in Japanese).

2) Kennedy R. P., S. A. Short, D. A. Wesley and T. H. Lee: Effect on nonlinear soil-structure interaction due to base slab uplift on the seismic response of a high-temperature gas-cooled reactor (HTGR), Nucl. Eng. and Design, 38, pp.323-355, 1976.

3) Takemori T., K. Sotomura and M. Yamada: Nonlinear dynamic response of reactor containment, Nucl. Eng. and Design 38, pp.463-474, 1976.

4) Wolf J. P.: Soil-structure interaction with separation of base from soil (lifting off), Nucl. Eng. and Design 38, pp.357-348, 1976.

5) Wolf J. P. and P. E. Skrikerud: Seismic excitation with large over-turning moments, tensile capacity, projecting basemat or lifting off?, Nuc. Eng. and Design 50, pp.305-321, 1978.

6) Tsuboi Y., Y. Hangai, M. Takida and M. Honma: A simple analytical method of walled structure considering up-lift of foundation, Proc. 5th Japan Earthquake Engineering Symposium, pp.1265-1272, 1978.

7) Goodman R. E.: Methods of geological engineering, West Publishing Company, pp.320-330, 1976.

8) Drucker R. C. and W. Prager: Soil mechanics and plastic analysis or limit design, Q. J. Appl. Meth. , Vol.10, No.2, pp.157-165, 1952.

9) Zienkiewicz O. C., S. Valliappan and I. P. King: Elasto-plastic solutions of engineering problems 'Initial stress', finite element approach, International Journal for Numerical Methods in Engineering, Vol.1, pp.75-100, 1969.

10) Duncan J. M. and C. Y. Chang: Non-linear analysis of stress and strains in soils, Proc. , ASCE, No.AM5, pp.1629-1653, 1970.

11) Pender M. J.: A model for the behavior of overconsolidated soil, Geotechnique 28, No.1, pp.1-25, 1978.

12) Mroz Z., V. A. Norris and O. C. Zienkiewicz, Application of anisotropic hardening model in the analysis of elasto-plastic deformation of soils, Geotechnique 29, No.1, pp.1-34, 1979.

13) Zienkiewicz O. C.: The finite element method, McGraw Hill, 3rd Ed., pp.25-27, 1977.

14) Constantpoulos I. V., J. M. Roesset and J. T. Christian: A comparison of linear and exact nonlinear analyses of soil amplification, Proc. 5th WCEE, pp.1805-1815, 1974.

15) Seed H. B. and I. M. Idress: Influence of soil conditions and ground motions during earthquakes, Proc. ASCE, Vol.95, No.SM1, pp.99-137, 1969.

16) Schnabel P. B., J. Lysmer and H. B. Seed: 'SHAKE' a computer program for earthquake response analysis of horizontally layered sites, Report No.EERC 72-12, College of Engineering, University of California, Berkeley, California, 1972.

17) Lysmer J., T. Udaka, C. Tsai and H. B. Seed, 'FLUSH' a computer program for approximate 3-D analysis of soil structure interaction problems, Report No.EERC 75-30, College of Engineering, University of California, Berkeley, California, 1975.

18) Seed H. D., J. Lysmer and R. Hwang: Soil-structure interaction analyses for seismic response, Proc. ASCE, Vol.101, No.GT5, pp.439-457, 1975.

19) Bieber R. E.: Seismic response analysis program (SRAP user's manual, Dynamic Analysis Corporation Report No.Dec/1279, 1976.

20) Bieber R. E. and H. J. Hovland: Seismic dynamic response by approximate methods, Int. J. Earthq. Eng. Struc. Dyn., Vol.8, pp.41-53, 1980.

21) Kuhlemeyer R. L. and J. Lysmer: Finite element method accuracy for wave propagation problems, Proc. ASCE, Vol.99, No.SM5, pp.421-427,

1973.

22) Kawamoto T. and M. Hayashi: Finite element analyses in geotechnical engineering, -Approaches to soil mechanics and rock mechanics-, Baifukan, p.312, 1978, (in Japanese).

23) Atalik T. S.: An alternative definition of instructure response spectra, Int. J. Earthq. Eng. Struc. Dyn., Vol.6, pp.71-78, 1978.

24) Wolf J. P.: Soil-structure interaction with separation of base from soil (lifting off), Nucl. Eng. and Design 38, pp.357-384, 1976.

25) Kennedy R. P., S. A. Short, D. A. Wesley and T. H. Lee: Effect on nonlinear soil-structure interaction due to base slab uplift on the seismic response of a high-temperature gas-cooled reactor (HTGR), Nucl. Eng. and Design 38, pp.323-355, 1976.

26) Toki K., F. Miura and T. Otake: Nonlinear seismic response analysis of soil-structure interaction system by 3-dimensional joint element, Proc. JSCE, No.322, pp.51-62, 1982, (in Japanese).

Appendix 2-I

Derivation of Eqs. 2-9 and 2-10.

As shown in Fig. 2-A-1, the deformation of the joint element must be sufficiently small when compared to the deformations of solid elements.

(1) Shearing deformation

The nodal displacements, u_s, of the solid element shown in Fig. 2-A-2 are given by Eq. 2-A-1 when the unit nodal forces, $F=1.0$, have been applied to nodal points 1 and 2:

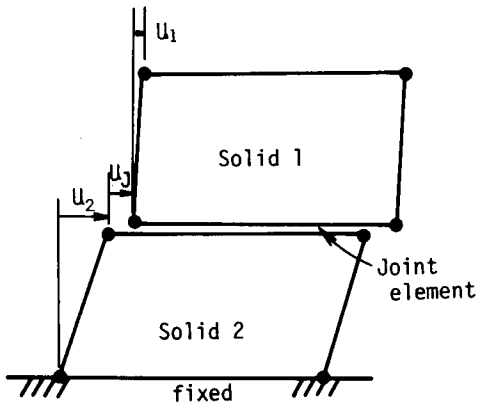

Fig. 2-A-1 The general scheme of a solid-joint system.

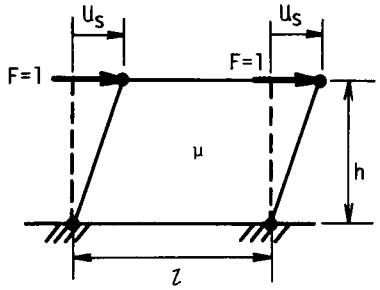

Fig. 2-A-2 Shearing deformation of a solid element.

$$u_s = \frac{2h}{\mu l} \tag{2-A-1}$$

where, μ is the rigidity, h, the height and l, the length of the solid element.

The nodal displacements, u_j, of the joint element shown in Fig. 2-A-3 are:

$$u_J = \frac{2}{k_s l} \tag{2-A-2}$$

where, k_s and l are the shear spring coefficient and the length of the joint element, respectively.

Here, the required relation is:

$$u_J \leqq \frac{1}{a} u_s \tag{2-A-3}$$

where, a is an appropriate constant which prescribes the deformation of the joint element relative to that of solid element. Substituting Eqs.

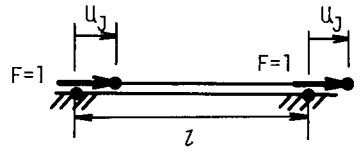

Fig. 2-A-3 Shearing deformation of a joint element.

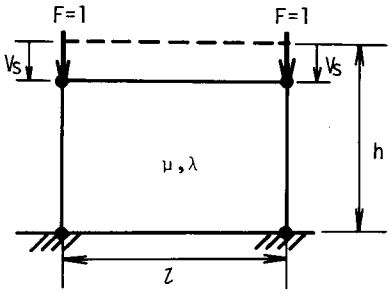

Fig. 2-A-4 Normal deformation of a solid element.

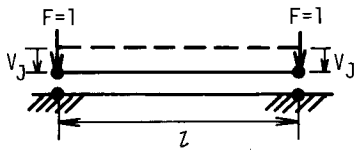

Fig. 2-A-5 Normal deformation of a joint element.

2-A-1 and 2-A-2 into Eq. 2-A-3:

$$k_s > \frac{\mu}{h} a \tag{2-9}$$

(2) Normal deformation

Nodal displacements of the solid element, v_s , in Fig. 2-A-4 are:

$$v_s = \frac{2h}{(2\mu + \lambda)\, l} \tag{2-A-4}$$

where, λ is Lamé's constant.

Nodal displacements of the joint element, v_j, (Fig. 2-A-5) are:

$$v_J = \frac{2}{k_n l} \tag{2-A-5}$$

where, k_n is the normal spring coefficient of the joint element.

The required relation is:

$$v_J \leq \frac{1}{b} v_s \tag{2-A-6}$$

Substituting Eqs. 2-A-4 and 2-A-5 into Eq. 2-A-6, the following relation is obtained.

$$k_n > \frac{2\mu + \lambda}{h} b \tag{2-10}$$

3. Three-Dimensional Nonlinear Behavior of Structures Resting on Soil

3.1 General remarks

A general method[1,2] has been proposed to analyze dynamic soil-structure interaction which uses joint elements set along the contact surface. The method was applied to test the stability of structures during strong earthquake motion. Material nonlinearity of the soil was included as a factor and its effects on the structural dynamic stability were examined[3,4]. All problems were, however, treated as two-dimensional, although many structures whose stability needs to be checked should be treated three-dimensionally. Besides, it is very important to determine the validity or limitations when a real three-dimensional system is replaced by a two-dimensional model.

The purpose of this chapter is to develop a three-dimensional joint element (3-D joint element) by an extension of the two-dimensional joint element proposed by Goodman[5], and to investigate its applicability. Although Goodman has already made a proposal[6], his 3-D joint element is not applicable for the soil-structure contact surface where no material exists, because it requires filling between two joint planes, and the stiffness matrix is obtained from the virtual work of the filling.

In the second half of this chapter, the structure's stability against sliding during strong earthquake motion is investigated in detail with relatively simple three-dimensional models.

3.2 A three-dimensional joint element

(1) Mode shapes of the 3-D joint element

Figure 3-1 shows the 3-D joint element. it consists of two re-

ctangular plates, each of which is made up of four nodal points, numbered $1 \sim 4$, and $5 \sim 8$. The length of the long side of the plate is m, and that of short side, ℓ. The local Cartesian coordinate system of the joint element is (r, s, t) and displacement components in these directions are (u, v, w).

Let (u_0, v_0, w_0) be the relative displacements at the center of the plates and (ϕ_r, ϕ_s, ϕ_t), the relative rotational angle around three symmetrical axes. The six are denoted by nodal displacements:

$$
\begin{aligned}
u_0 &= \{(u_5+u_6+u_7+u_8)-(u_1+u_2+u_3+u_4)\}/4 \\
v_0 &= \{(v_5+v_6+v_7+v_8)-(v_1+v_2+v_3+v_4)\}/4 \\
w_0 &= \{(w_5+w_6+w_7+w_8)-(w_1+w_2+w_3+w_4)\}/4 \\
\phi_s &= \{(-w_5-w_6+w_7+w_8)-(-w_1-w_2+w_3+w_4)\}/2\ell \\
\phi_r &= \{(w_5-w_6-w_7+w_8)-(w_1-w_2-w_3+w_4)\}/2m \\
\phi_t &= \{-u_1+u_2+u_3-u_4+u_5-u_6-u_7+u_8)/4m \\
&\quad +(-v_1-v_2+v_3+v_4+v_5+v_6-v_7-v_8)\}/4\ell
\end{aligned}
\tag{3-1}
$$

or

$$
\{\varepsilon_0\}_J = [L_0]\{u\}_J \tag{3-2}
$$

where,

$$
\{\varepsilon_0\}_J = \{u_0 \;\; v_0 \;\; w_0 \;\; \phi_r \;\; \phi_s \;\; \phi_t\}^T \tag{3-3}
$$

$$
\{u\}_J = \{u_1 \;\; v_1 \;\; w_1 \;\; \cdots \;\; u_8 \;\; v_8 \;\; w_8\}^T \tag{3-4}
$$

$\{\varepsilon_0\}_J$ and $\{u\}_J$ are modal and nodal displacement vectors, respectively, and $[L_0]$ is described in Appendix 3-I.

The six fundamental modes $\{\varepsilon_0\}_J$ are illustrated in Fig. 3-2. They are classified as:

(i) sliding modes - Mode 1 and Mode 2

(ii) a separation mode - Mode 3

(iii) rotational modes - Mode 4, Mode 5 and Mode 6

A contact surface modeled by this 3-D joint element can be expressed by a combination of the six modes.

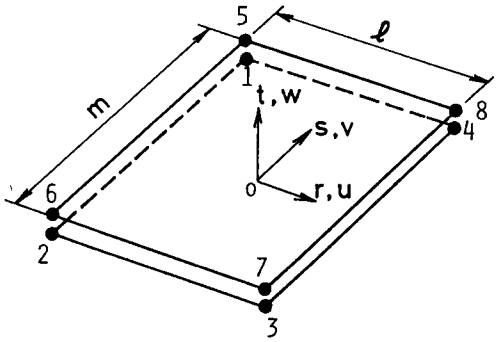

Fig. 3-1 The three-dimensional joint element.

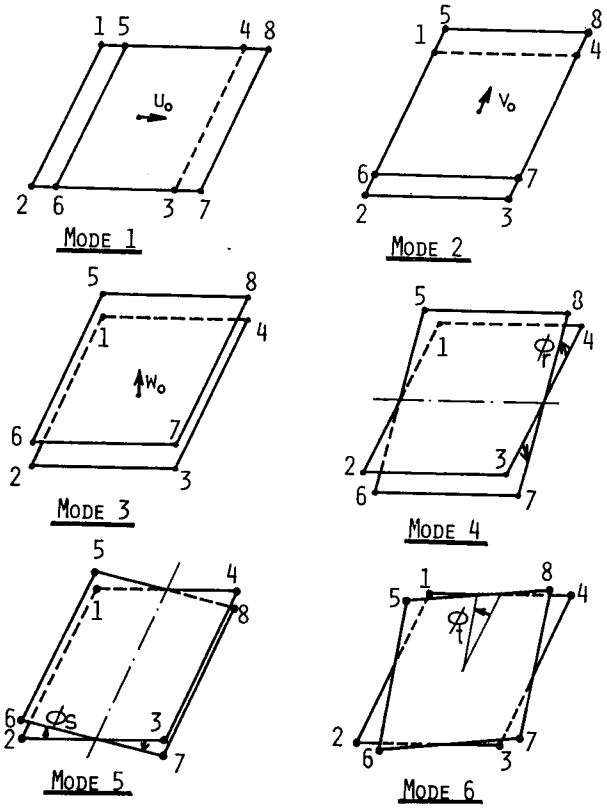

Fig. 3-2 Joint element deformation modes.

(2) Stress components of the 3-D joint element

Let σ_r and σ_s be the shear stress components corresponding to modes 1 and 2 and σ_t be the normal component corresponding to Mode 3. These components are defined as the average forces acting on the joint plane per unit area of the joint element and are given by:

$$\left.\begin{aligned}\sigma_r &= \{F_{r,5}+F_{r,6}+F_{r,7}+F_{r,8}\}/\ell m\\ \sigma_s &= \{F_{s,5}+F_{s,6}+F_{s,7}+F_{s,8}\}/\ell m\\ \sigma_t &= \{F_{t,5}+F_{t,6}+F_{t,7}+F_{t,8}\}/\ell m\end{aligned}\right\} \tag{3-5}$$

where, $F_{i,j}$ is the nodal force acting on node j in direction i. Three components of moment, M_r, M_s and M_t corresponding to modes 4, 5 and 6 are defined as:

$$\left.\begin{aligned}M_s &= \frac{\ell}{2}(F_{t,7}+F_{t,8})-\frac{\ell}{2}(F_{t,5}+F_{t,6})\\ M_r &= \frac{m}{2}(F_{t,5}+F_{t,8})-\frac{m}{2}(F_{t,6}+F_{t,7})\\ M_t &= \frac{m}{2}(F_{r,5}+F_{r,8})-\frac{m}{2}(F_{r,6}+F_{r,7})\\ &\quad+\frac{\ell}{2}(F_{s,5}+F_{s,6})-\frac{\ell}{2}(F_{s,7}+F_{s,8})\end{aligned}\right\} \tag{3-6}$$

Inverting equations 3-5 and 3-6 and stipulating that $F_{i,1}=-F_{i,5}$, $F_{i,2}=-F_{i,6}$, $F_{i,3}=-F_{i,7}$ and $F_{i,4}=-F_{i,8}$ ($i=r,\ s,\ t$), the nodal force vector $\{F\}_J$ can be written in terms of the stress vector $\{\sigma\}_J$, as

$$\{F\}_J = [B]_J\{\sigma\}_J \tag{3-7}$$

where,

$$\{F\}_J = \{F_{r,1}\ F_{s,1}\ F_{t,1}\cdots\cdots F_{r,8}\ F_{s,8}\ F_{t,8}\}^T \tag{3-8}$$

$$\{\sigma\}_J = \{\sigma_r\ \sigma_s\ \sigma_t\ M_r\ M_s\ M_t\}^T \tag{3-9}$$

$[B]$ is shown in Appendix 3-II.

(3) Relationships between stresses and strains

The stress, $\{\sigma\}_J$, and modal vectors, $\{\varepsilon_0\}_J$ are linked through joint system stiffness properties $[D]$ as follows.

$$\{\sigma\}_J = [D]\{\varepsilon_0\}_J \tag{3-10}$$

where,

$$[D] = \begin{pmatrix} k_r & & & & & \\ & k_s & & 0 & & \\ & & k_t & & & \\ & & & k_{\phi r} & & \\ & 0 & & & k_{\phi s} & \\ & & & & & k_{\phi t} \end{pmatrix} \tag{3-11}$$

k_r and k_s are shear spring coefficients in directions r and s respectively, and k_t is the normal spring coefficient. $k_{\phi r}$, $k_{\phi s}$ and $k_{\phi t}$ are rotational spring coefficients with respect to axes r, s and t, and they are derived by k_r, k_s and k_t as:

$$\left.\begin{aligned} k_{\phi r} &= \frac{\ell m^3}{4} k_t \\ k_{\phi s} &= \frac{\ell^3 m}{4} k_t \\ k_{\phi t} &= \frac{1}{12}(\ell m^3 k_r + \ell^3 m k_s) \end{aligned}\right\} \tag{3-12}$$

In this derivation, the four nodal points forming a joint plane are assumed to be on the plane even after the deformation of the joint element[7]. This assumption is valid when it models the contact surface between such hard materials as concrete structures and the ground.

(4) The stiffness matrix of the 3-D joint element

From Eqs. 3-2, 3-7 and 3-10 the relationship between nodal forces $\{F\}_J$ and nodal displacements $\{u\}_J$ is

$$\{F\}_J = [B]_J[D][L_0]\{u\}_J \tag{3-13}$$

As a matrix which gives the relationships between nodal forces and

nodal displacements is the stiffness matrix, the stiffness matrix of the 3-D joint element $[K]_J$ is given by the following equations from Eq. 3-13.

$$[K]_J=[B]_J[D][L_0] \tag{3-14}$$

$$[K]_J=\begin{bmatrix} [E]_J & -[E]_J \\ -[E]_J & [E]_J \end{bmatrix} \tag{3-15}$$

Matrix $[E]_J$ is given in the next page.

(5) Constitutive relationships of the 3-D joint element

The constitutive relationships are shown in Fig. 3-3. Fig. 3-3(a) is for the normal and (b) for the tangential component. Normal stress is not transmitted when separation occurs, and linear constitutive relationship based on stiffness, k_t, is valid when the joint element is in contact. Sliding will take place when the absolute value of the shear stress, τ, reaches yield shear stress, τ_y. When separation occurs, shear stress is not transmitted through the joint element.

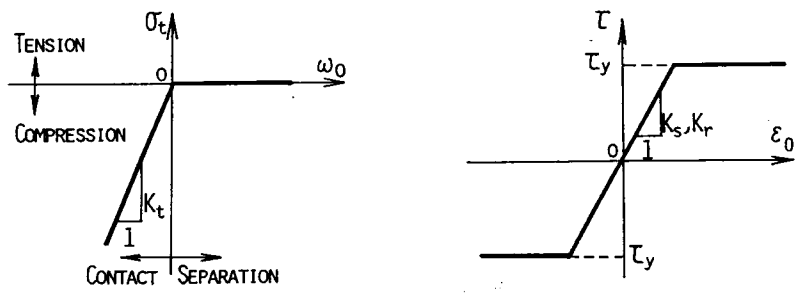

(a) Normal direction

(b) Tangential direction

Fig. 3-3 The constitutive relationship of the joint element.

$$
[E]_J = \begin{Bmatrix}
\psi_r+\varphi_m & \varphi_{\ell m} & 0 & \psi_r-\varphi_m & \varphi_{\ell m} & 0 & \psi_r-\varphi_m & -\varphi_{\ell m} & 0 & \psi_r+\varphi_m & -\varphi_{\ell m} & 0 \\
 & \psi_s+\varphi_\ell & 0 & -\varphi_{\ell m} & \psi_s+\varphi_\ell & 0 & -\varphi_{\ell m} & \psi_s-\varphi_\ell & 0 & \varphi_{\ell m} & \psi_s-\varphi_\ell & 0 \\
 & & \psi_t+\varphi_r+\varphi_s & 0 & 0 & \psi_t+\varphi_r-\varphi_s & 0 & 0 & \psi_t-\varphi_r-\varphi_s & 0 & 0 & \psi_t-\varphi_r+\varphi_s \\
 & & & \psi_r+\varphi_m & -\varphi_{\ell m} & 0 & \psi_r+\varphi_m & \varphi_{\ell m} & 0 & \psi_r-\varphi_m & \varphi_{\ell m} & 0 \\
 & & & & \psi_s+\varphi_\ell & 0 & -\varphi_{\ell m} & \psi_s-\varphi_\ell & 0 & \varphi_{\ell m} & \psi_s-\varphi_\ell & 0 \\
 & & & & & \psi_t+\varphi_r+\varphi_s & 0 & 0 & \psi_t-\varphi_r+\varphi_s & 0 & 0 & \psi_t-\varphi_r-\varphi_s \\
 & & & & & & \psi_r+\varphi_m & \varphi_{\ell m} & 0 & \psi_r-\varphi_m & \varphi_{\ell m} & 0 \\
 & & & & & & & \psi_s+\varphi_\ell & 0 & -\varphi_{\ell m} & \psi_s+\varphi_\ell & 0 \\
 & & & & & & & & \psi_t+\varphi_r+\varphi_s & 0 & 0 & \psi_t+\varphi_r-\varphi_s \\
 & & & & & & & & & \psi_r+\varphi_m & -\varphi_{\ell m} & 0 \\
 & & & & & & & & & & \psi_s+\varphi_\ell & 0 \\
 & & & & & & & & & & & \psi_t+\varphi_r+\varphi_s
\end{Bmatrix}
$$

Symmetric

..... (3-16)

$$
\left.\begin{aligned}
\psi_r &= \frac{1}{16}\ell m k_r & \varphi_\ell &= \frac{1}{16\ell^2}k_{\phi t} \\
\psi_s &= \frac{1}{16}\ell m k_s & \varphi_{\ell m} &= \frac{1}{16\ell_m}k_{\phi t} \\
\psi_t &= \frac{1}{16}\ell m k_t & \varphi_r &= \frac{1}{4\ell^2}k_{\phi r} \\
\varphi_m &= \frac{1}{16m^2}k_{\phi t} & \varphi_s &= \frac{1}{4m^2}k_{\phi s}
\end{aligned}\right\} \qquad (3\text{-}17)
$$

The yield shear stress τ_y is determined as a function of the cohesion, c_J, and friction angle, ϕ_J, of the contact surface and normal stress, σ_t, from the Mohr-Coulomb failure law,

$$\left.\begin{aligned} \tau_y &= c_J - \sigma_t \tan\phi_J \qquad (w_0 \leqq 0\text{: in contact}) \\ &= 0 \qquad\qquad\qquad\quad (w_0 > 0\text{: separation}) \end{aligned}\right\} \tag{3-18}$$

Because there are two shear stress components, σ_r and σ_s, corresponding to Mode 1 and Mode 2, the magnitude of mobilized shear stress τ is

$$\tau = \sqrt{\sigma_r^2 + \sigma_s^2} \tag{3-19}$$

or in other words, sliding takes place when mobilized shear stress reaches yield shear stress.

Since the spring coefficients of the joint element k_r, k_s and k_t are related to the fictitious relative elastic deformation at the contact surface between two solids, (which would not actually occur in a real system) they should be as large as possible. The influence on the system's response of fictitious displacement due to the joint spring coefficients cannot be overlooked when the coefficients are small. The influence of spring coefficient magnitude on the dynamic response is discussed in detail in the next section.

(6) A load transfer method to handle three-dimensional nonlinear structures

The load transfer method is a means to analyze nonlinear dynamic response. The detailed two-dimensional procedure has already been explained, and once the "de-restraining forces", additional external forces to making nonlinear and linear systems equivalent have been obtained, the load transfer method can be employed in the same manner as when two-dimensional problems are concerned. The procedure by which these forces can be measured is explained here.

As normal stress is not constant over the entire joint element be-

cause of the moments defined by Eq. 3-6, the joint element is divided into four equal subdivisions by two center lines. The possibility of sliding or separation is examined for each subdivision.

(i) The soil-structure system is assumed to be a linear elastic system and nodal displacements are obtained by solving the equation of motion at time $t=t_j$. The nodal displacement vector of the joint element at t_j is:

$$\{u\}_J^j=\{u_1 \quad v_1 \quad w_1 \cdots\cdots u_8 \quad v_8 \quad w_8\}^j \tag{3-20}$$

(ii) The nodal force vector $\{F\}_J^j$ equivalent to the stresses caused by $\{u\}_J^j$ is obtained from the stiffness matrix $[K]_J$.

$$\{F\}_J^j=[K]_J\{u\}_J^j \tag{3-21}$$

(iii) The prescribed constitutive relationships are examined to see if they are satisfied or not with respect to the nodal forces given by Eq. 3-21. Sliding at the subdivision which includes nodal point k, occurs when

$$\sqrt{F_{r,k}^2+F_{s,k}^2} > \frac{\ell m}{4} c_J - F_{t,k}\tan\phi_J \quad (k=5\sim8) \tag{3-22}$$

is satisfied. In this case, the de-restraining force, f, is obtained by subtracting the right term from the left term.

When separation is taking place at the subdivision including nodal point k,

$$F_{t,k}>0 \qquad (k=5\sim8) \tag{3-23}$$

is satisfied. The de-restraining force, f, equals $F_{t,k}$, and its vector $\{f\}$ is obtained from:

$$\left.\begin{aligned} f_{i,1}&=-f_{i,5} \qquad f_{i,2}=-f_{i,6} \\ f_{i,3}&=-f_{i,7} \qquad f_{i,4}=-f_{i,8} \end{aligned}\right\} \quad (i=r,s,t) \tag{3-24}$$

$$\{f\} = \{f_{r,1}\ f_{s,1}\ f_{t,1} \cdots\cdots f_{r,8}\ f_{s,8}\ f_{t,8}\} \tag{3-25}$$

Once $\{f\}$ is obtained, they are added to the external forces of the equation of motion, and the computation proceeds again from step (i). The iterative procedure should be continued until the constitutive relationships of all joint elements have been satisfied.

3.3 Dynamic response characteristics of soil-structure interaction systems when separation or sliding is taking place

(1) Analyzed models

Figure.3-4 is a model of a three-dimensional soil-structure interaction system. The model consists of the homogeneous elastic surface ground and a concrete cubic structure resting on it. Coarse (Fig. 3-5) and fine (Fig. 3-6) finite element meshes are used. The former, Model 1, examines the fundamental features of nonlinear dynamic responses. The latter, Model 2, examines the dynamic stability of the structure against sliding during strong ground motion. One joint element for Model 1 and nine for Model 2 model the contact surface between the structure and the ground. The modeling parameters are tabulated in Table 3-1.

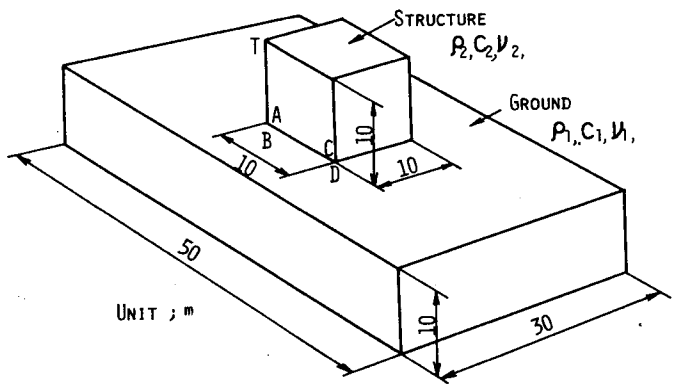

Fig. 3-4 A general view of the soil-structure system.

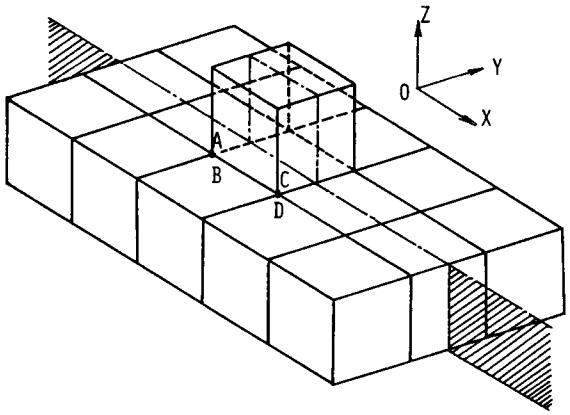

Fig. 3-5 Finite element mesh of Model 1.

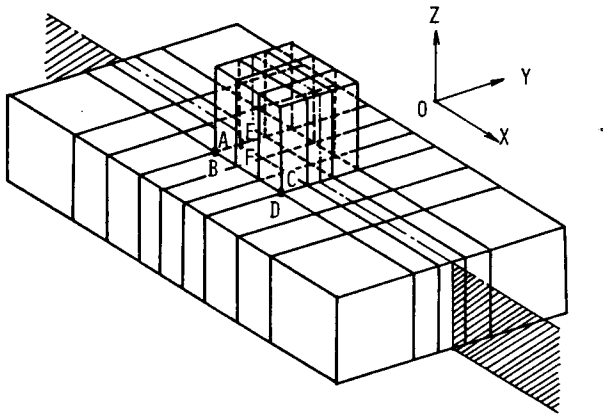

Fig. 3-6 Finite element mesh of Model 2.

Table 3-1 Modeling parameters.

	Unit weight (tf/m^3)	Shear wave velocity (m/sec)	Poisson's ratio	Damping factor
Ground	γ_1=1.98	C_1=300	ν_1=0.4	h_1=0.10
Structure	γ_2=2.35	C_2=1600	ν_2=0.2	h_2=0.10
Joint element	Spring const. $K_r=K_s=K_t=2.0\times10^5$ tf/m^3 Cohesion C_J=3.4, 10 tf/m^2 Friction angle ϕ_J=30°			

The local coordinate system of the joint element (r, s, t) corresponds to the global coordinate system (X, Y, Z). As the degrees of freedom of a three-dimensional model becomes much greater than those of the two-dimensional model when the number of elements is the same, a contrivance is necessary to overcome the disadvantage of using the three-dimensional model. Therefore, the analyses have been carried out taking advantage of geometrical symmetry with respect to the center plane (the hatched plane in Figs. 3-5 and 3-6). In other words, with respect to the center plane, it is assumed that deformations of the system are symmetrical in X and Z directions and asymmetric in the Y direction.

Nodal displacements in the Y direction are fixed on the boundary plane, parallel to the model ground's X-Z plane. When the input direction is parallel to the X-Y plane, this assumption is valid. The structure and ground are modeled by three-dimensional isoparametric elements with eight nodal points[8], and assumed to be linear elastic materials. The shape function, stiffness and mass matrices of the element are derived in Appendix 3-III.

(2) The initial stress state

Initial stresses are obtained by solving the static problem, in which the external force, $\{f_0\}$, is equivalent to the weight of the system, and can be calculated as:

$$\{f_0\} = -\int_v [N]^T \{p\} dv \qquad (3\text{-}26)$$

where, $\{p\} = \{\, 0 \;\; -\rho g \,\}^T$, ρ is mass density, g, the acceleration of gravity and $[N]$, is the shape function matrix from Appendix 3-III.

The resulting initial stress state at the bottom of Model 1 structure is 23.5 tf/m^2 for normal stress, σ_Z, and 0.0 tf/m^2 for shear stresses, σ_X and σ_Y. As the contact surface is modeled by one joint element, the initial stresses over it are constant. The initial stresses of Model 2 are shown in Fig. 3-13 and discussed in section 3.4.

(3) Adequate magnituds of joint element spring coefficients

The adequate magnitude of joint element spring coefficients is discussed for Model 1 subjected to a 100 gal sinusoidal acceleration and 7.5 Hz, the fundamental natural frequency of model ground. All coefficients k_r, k_s and k_t are equal and using the three different values 5.0×10^4 tf/m^3, 2.0×10^5 tf/m^3, and 1.0×10^6 tf/m^3, the influence of magnitude on the system's dynamic response is examined.

Figure 3-7(a) illustrates horizontal displacement at the structure's bottom corner point (nodal point A in Fig. 3-5) and Fig. 3-7(b) vertical displacement at the same point. Solid lines represent responses of the linear model in which the joint element has been removed, broken lines, responses with a spring coefficient of 5.0×10^4 tf/m^3 and dotted lines, responses with a spring coefficient of 2.0×10^5 tf/m^3. In these analyses, neither separation nor sliding takes place, therefore, the differences between broken or dotted lines and solid lines can be attributed to the fictitious elastic deformation caused by joint element springs. The figures indicate that the smaller the coefficient, the larger the difference. When the coefficient is 5.0×10^6 tf/m^3, the difference due to the fictitious deformation must be considered. This difference is negligible, however, when the coefficient is larger than 2.0×10^5 tf/m^3.

On the other hand, the larger the spring coefficient, the smaller the interval, Δt, necessary to perform the numerical integration of the equation of motion. The solution did not converge unless the interval Δt was less than 0.002 sec when the coefficient was 5.0×10^4 tf/m^3. In the same way, the maximum Δts which give convergence of the solutions are 0.001 sec and 0.0005 sec for 2.0×10^5 tf/m^3 and 1.0×10^6 tf/m^3 respectively. From the view points of economy and accuracy, the 2.0×10^5 tf/m^3 coefficient was used. The relationships between the numerical errors and Δts are summarized in Table 3-2.

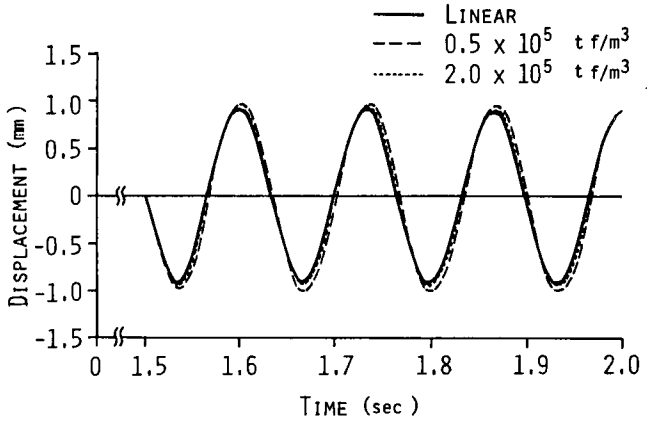

(a) Horizontal displacement

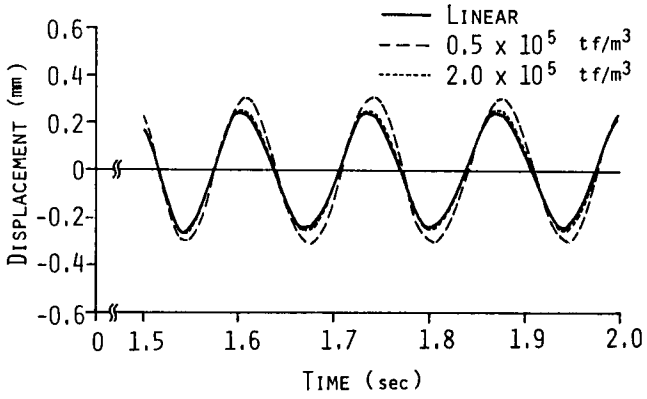

(b) Vertical displacement

Fig. 3-7 The influence of spring coefficient magnitude on dynamic response.

Table 3-2 Relationships between time interval, accuracy and magnitude of joint element spring coefficients.

Spring constant (tf/m^3)	Time interval Δt (sec)	Error (%)	
		Horizontal displacement	Vertical displacement
0.5×10^5	0.002	8.0	23.2
2.0×10^5	0.001	2.2	3.3
10.0×10^5	0.0005	0.4	0.5

(4) Sliding phenomenon at the contact surface

Model 1 is subjected to a sinusoidal acceleration of 100 gal amplitude and 4 Hz. Cohesion of the joint element is 3.4 tf/m^2 and its friction angle is 30°.

The horizontal acceleration response curve is shown by Fig. 3-8(a) and horizontal displacement by Fig. 3-8(b). In the response analysis, sliding took place first at about 0.93 sec and periodic sliding continued to occur. In Fig. 3-8(a), sharp peaks can be observed at the moments of the sliding. However, no disturbance in the displacement curve.

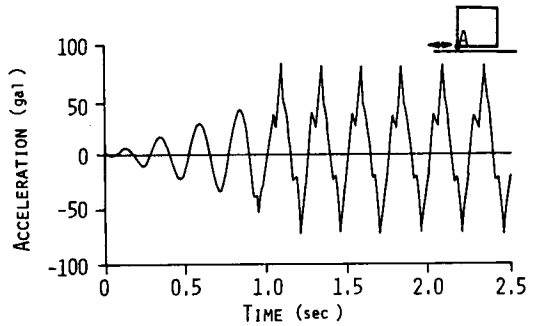

(a) Horizontal acceleration at point A

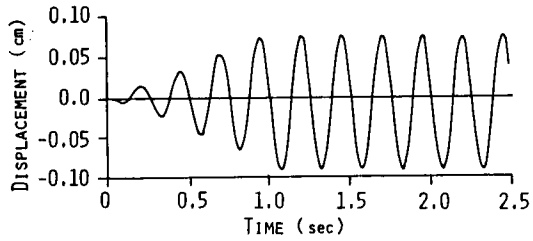

(b) Horizontal displacement at point A

Fig. 3-8 Examples of response curves during sliding due to sinusoidal excitation (Model 1 - 4 Hz, 100 gal).

Figure 3-9 shows the hysteresis curve of shear stress, and the relative displacement of the joint element. Numbers on the curve indicate the time elapsed. Although shear stress does not become negative according to the definition of Eq. 3-19, the negative sign is assigned to it when the structure slides in a negative x direction relative to the ground. The response of the system becomes stationary at about 1.05

sec, after which the shear stress-relative displacement relationship is in the form of the most external hysteresis loop.

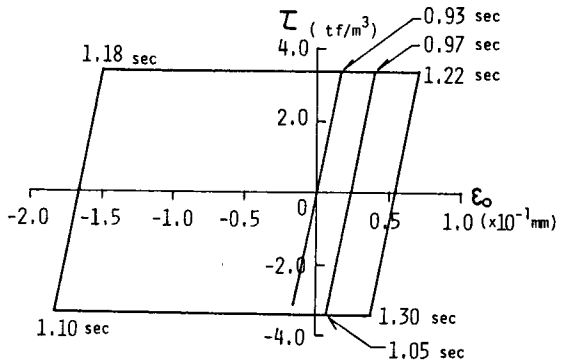

Fig. 3-9 A hysteresis loop for shear direction on the contact surface.

(5) Separation phenomenon at the contact surface

In order to examine the dynamic response characteristics of a system in which separation is taken place, the input acceleration amplitude is increased to 600 gal, and, in addition, c_y is increased to be 10 tf/m^2 to prevent the occurrence of sliding.

Figure 3-10(a) shows horizontal acceleration, (b) vertical acceleration and (c) horizontal displacement responses at point C in Fig. 3-5.

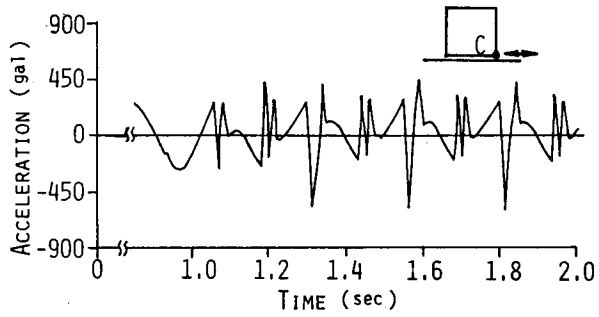

(a) Horizontal acceleration

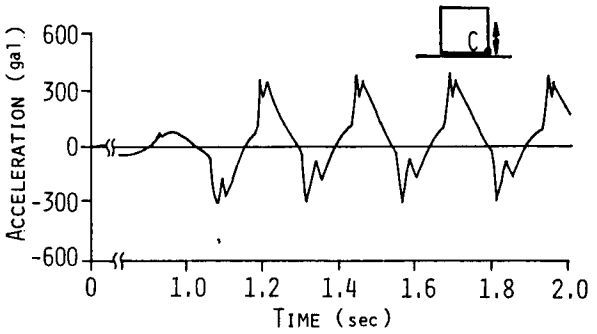

(b) Vertical acceleration

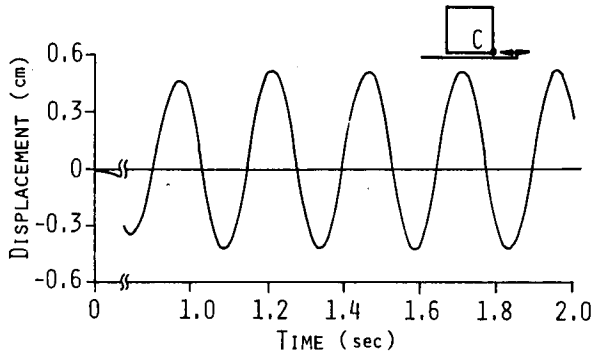

(c) Horizontal displacement

Fig. 3-10 Examples of response curves when separation is caused by sinusoidal excitation (Model 1 - 4 Hz, 600 gal).

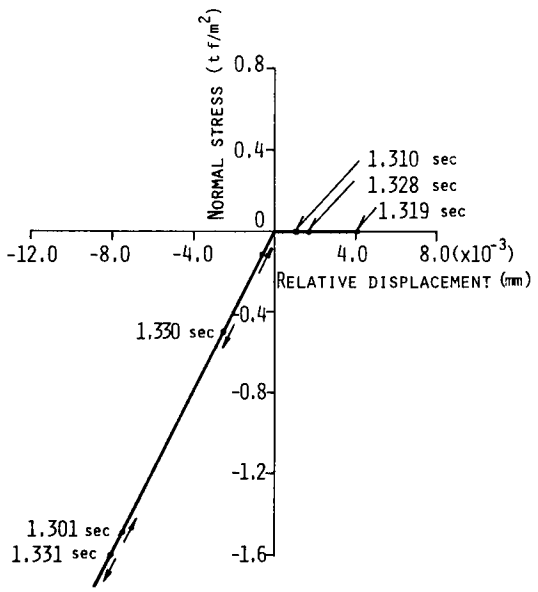

Fig. 3-11 A hysteresis curve for normal direction on the contact surface.

The first occurrence of separation was at 1.05 sec after which it re-occurs periodically. At such times, the same type of sharp peaks can be seen in acceleration curves as when sliding takes place. When sliding or separation took place, the balance of the system's dynamic force changed suddenly and there was a large increase in acceleration to compensate for this dynamic imbalance. The change did not affect the displacement response, however.

Figure 3-11 shows the hysteresis curve of joint element normal stress and relative normal displacement. From Figs.3-9 and 3-11, it has been ascertained that the assumed constitutive relationships are satisfied for both shear and normal components.

3.4 Structural dynamic stability against sliding

(1) The initial stress state of the contact surface of Model 2

Figure 3-12 shows the half plane of the contact surface between the structure and ground in Model 2. Solid circles indicate nodal points and solid line boundaries between joint elements. Broken lines denote joint element subdivision boundaries. Initial stress distributions are illustrated in Figure 3-13(a) and (b). The former shows the normal initial stress and the latter shear initial stress. Note that the initial stresses at the corner of the contact surface are larger than those in inner zones. Shear stress component does not appear to be due to restraints at the boundary of the model.

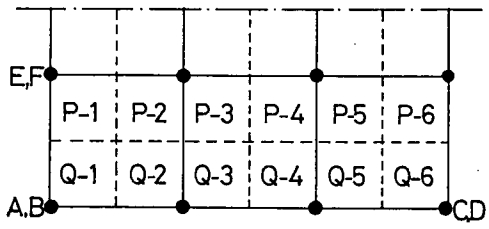

Fig. 3-12 Subdivisions of the contact surface.

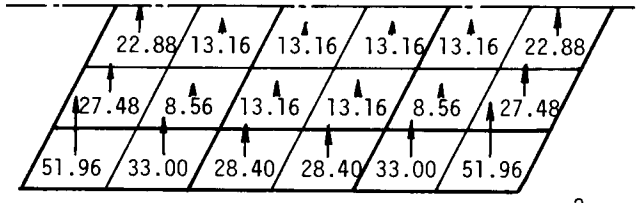

Unit ; tf/m^2

(a) Normal initial stress

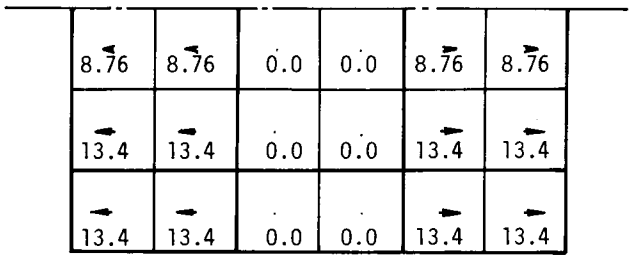

Unit ; tf/m^2

(b) shear initial stress

Fig. 3-13 Initial stresses on the contact surface caused by the gravity force.

(2) Definition of the safety factor against sliding

The safety of the structure against sliding can be examined by the ratio of yield shear stress τ_y to mobilized shear stress τ, τ_y / τ. Three safety factors are introduced in order to examine in detail structural stability against sliding. These safety factors are:

(a) The local safety factor (LSF)

The local safety factor is defined as the minimum value of the ratio τ_y / τ of all subdivisions of all joint elements, which have been obtained throughout the entire analytical period, or analyzed time. That is,

$$LSF = \left| \frac{\tau_y}{\tau} \right|_{min.T, min.S} \tag{3-27}$$

where, min.T means the minimum value with respect to the entire time analyzed and min.S the minimum value of a subdivisions.

(b) The total safety factor (TSF)

The total safety factor is defined by:

$$TSF = \left| \frac{\sum_{j=1}^{} \tau_{yj} A_j}{\sum_{j=1}^{} \tau_j A_j} \right|_{min.T} \tag{3-28}$$

where, N is the number of subdivisions forming the contact surface and τ_{yj} τ_j and A_j represent yield shear stress, mobilized shear stress and the area of a subdivision, j. TSF indicates the safety against sliding of the whole structure, while LSF indicates that of one area of the contact surface.

(c) The static safety factor (SSF)

Safety against sliding of the whole structure can be checked in practice by applying the static force equivalent to the seismic force, to the structure's center of gravity. In this case, the safety factor is defined by the ratio of yield shear force, F_{ys}, to applied static force, F_s, or,

$$SSF = \frac{F_{ys}}{F_s} = \frac{C_J A + W \tan \phi_J}{W \frac{\alpha}{g}} \tag{3-29}$$

where, A and W are the bottom area and the weight of the structure, respectively, and α, the maximum horizontal response acceleration at the center of the gravity. Here, α has been obtained from a dynamic analysis of linear model from which joint elements have been removed.

(3) Structural safety against sliding when subjected to sinusoidal excitation

Figure 3-14 shows time histories of mobilized shear stress τ and yield shear stress τ_y on subdivisions P-1, P-2 and P-3, when Model 2 has been subjected to sinusoidal excitation of 300 gal and 4 Hz. Joint element C_J and ϕ_J are 10 tf/m^2 and 30°, respectively.

In P-1, separation takes place at 1.2 sec. At this time both τ and τ_y vanishes and sliding in P-2 takes place simultaneously owing to the redistribution of shear stress. The shear stress which has vanished due

to separation may be transmitted to the adjacent subdivisions and this redistribution increased shear stress and sliding in P-2. It is worthwhile to note that detailed investigations of the mechanisms of stress redistribution as well as dynamic stability are possible.

Sliding of the whole structure does not occur because the ratio τ_y / τ is greater than 3.0 throughout the analysis.

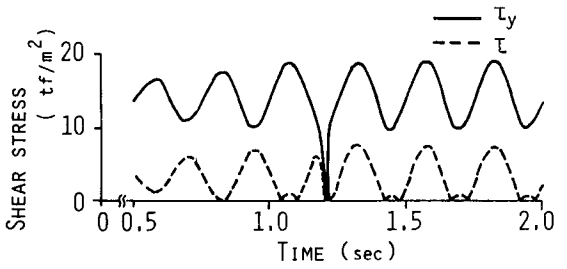

(a) P-1

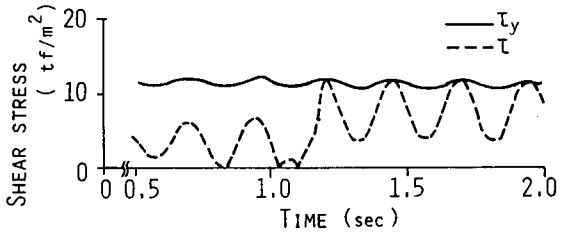

(b) P-2

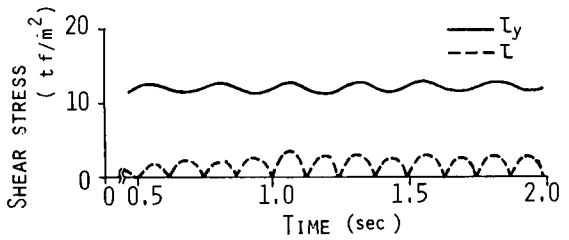

(c) P-3

Fig. 3-14 Shear and yield stresses at subdivisions P-1, P-2 and P-3.

(4) Safety against sliding when the structure is subjected to seismic excitations

Model 2 has been subjected to three accelerograms.

(a) Discussion on local sliding

The cross-hatched areas in Fig. 3-15 are the subdivisions where sliding takes place: (a) is for excitation by the El Centro accelerograms, (b) is for the J.P.L. accelerograms and (c) for the Hachinohe accelerograms. As would be expected, El Centro accelerograms with the highest maximum amplitude caused the widest sliding area. Hachinohe accelerograms, however, caused wider sliding than J.P.L. accelerograms, although the maximum horizontal acceleration of the former is lower.

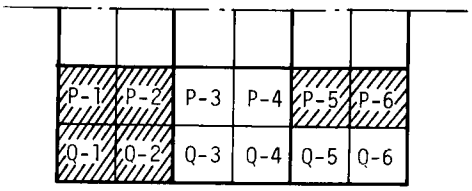

(a) El Centro accelerograms

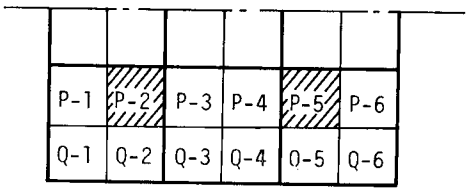

(b) J.P.L. accelerograms

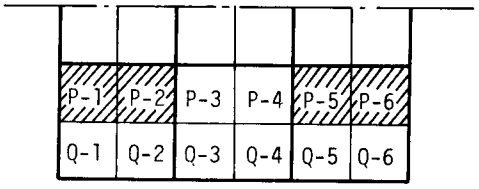

(c) Hachinohe accelerograms

Fig. 3-15 Subdivisions where sliding occurred.

This can be attributed to the predominant frequency which agree with what was found for two-dimensional problem, that is, the lower the predominant frequency of input excitation, the more the structure is apt to slide.

Sliding first occurs at inner subdivisions next to those of the edge, and the zone appears to expand outward. This is due to the initial stress state, that is, although shear stresses on P-2 and P-5 are the same as those on outer subdivisions, P-1, P-6, Q-1, Q-2, Q-5 and Q-6, the normal stresses on P-2 and P-5 are smaller, as shown in Fig. 3-13. This state gives P-2 and P-5 low safety factors. Time histories of the ratios τ_y/τ for subdivisions P-1, P-2 and Q-1 are illustrated in Figs. 3-16(a), (b) and (c) respectively, in which Model 2 has been subjected to the El Centro accelerograms. When the ratio is greater than eight, it is drawn as eight. The straight line, $\tau_y/\tau=1.0$ is drawn and when the τ_y/τ curve meets it, sliding is taking place, or, in fact, twice at P-1, only once at Q-1, but several times at P-2.

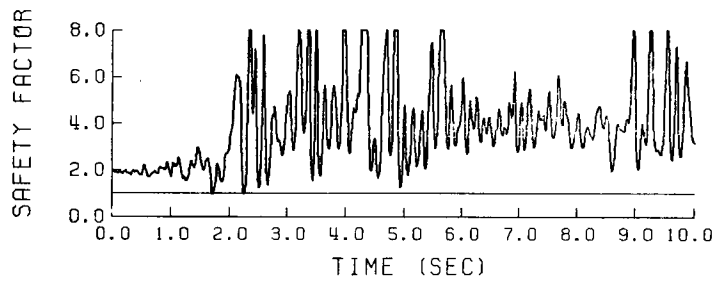

(a) P-1

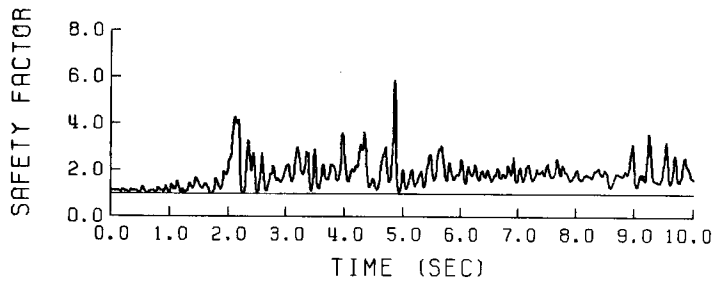

(b) P-2

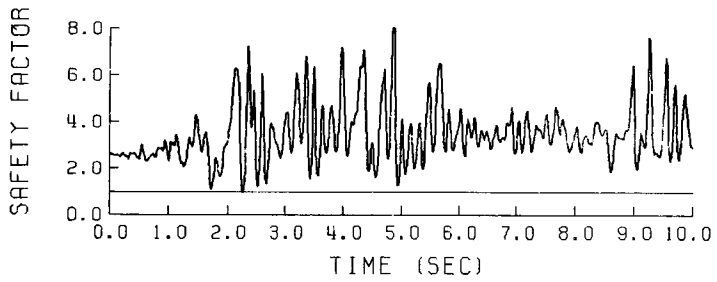

(c) Q-1

Fig. 3-16 The safety factor against sliding for each subdivision.

(b) Safety of the whole structure against sliding

TSF and SSF are tabulated in Table 3-3 when Model 2 has been subjected to the above seismic excitations. All the TSF are greater than 1.0 meaning no sliding of the whole structure. It should be noted that TSFs obtained dynamically are about twice as large as SSF obtained statically for all accelerograms.

Two two-dimensional models are introduced in order to compare TSFs with those of three-dimensional models. The shape of the former are the same as the cross section of Model 2 (the cross-hatched area in Fig.3-6). The models are labelled Model 2D and Model 2DM, respectively. Model 2D consists of the same materials as Model 2. The stiffness of Model 2DM has been, however, increased to give it have the same fundamental natural frequency as Model 2. The two-dimensional TSFs and SSFs are tabulated in Table 3-4. By comparing two-dimensional SSFs (Table 3-4) and with those of Model 2 (Table 3-3), there was good agreement between models with identical fundamental natural frequencies, but less between Model 2 and Model 2D for all accelerogram types.

When TSF has been obtained dynamically, that of Model 2 is more than double those of the two-dimensional models. The results imply that an actual three-dimensional structure would be safe against sliding even when a two-dimensionally replaced model subjected to seismic force or a

three-dimensional model subjected to static force is at the critical state for sliding.

Table 3-3 Static and dynamic analyses compared for safety factors against sliding - Model 2 - (f_1=6.46 Hz):

	El Centro	J.P.L.	Hachinohe
S S F (static)	1.85	3.47	3.06
T S F (dynamic)	4.07	7.89	6.22

Table 3-4 Static and dynamic analyses of two-dimensional models compared for safety factors against sliding for Models 2D and 2DM.

	Model 2D (f_1=5.47 Hz)	Model 2DM (f_1=6.46 Hz)		
Input	El Centro	El Centro	J.P.L.	Hachinohe
S S F (static)	1.62	1.78	3.38	2.23
T S F (dynamic)	1.62	1.80	3.45	2.36

3.5 Conclusions

A three-dimensional joint element has been developed by an expansion of the two-dimensional joint element proposed by Goodman. It was adopted to model the contact surface between a three-dimensional structure and soil.

The applicability of the joint element and the sliding stability of the structure have been examined in detail. From the analyses, the following conclusions are made:

(1) The proposed method makes it possible to estimate dynamic stresses at the contact surface and also to clarify the mechanism of stress redistribution at the contact surface when local sliding or separation has taken place.

(2) Earthquake response analyses were carried out for the El Centro NS and UD components, the J.P.L. S82E and UD components and the Hachinohe EW and UD components. Safety factors of the whole structure against sliding were about twice as great as when obtained by dynamic response analyses than by the seismic coefficient method.

(3) Safety factors were compared between the three-dimensional model and those of two-dimensional models with the same cross section as the former. The safety factors obtained from two-dimensional models were lower than those obtained from three-dimensional model for all seismic excitations.

The results imply that an actual three-dimensional structure would be safe against sliding even when a two-dimensionally replaced model subjected to seismic force or a three-dimensional model subjected to static force is at the critical state for sliding occurrence.

There are, however, several problems which remain to be solved. The four nodal points which form the joint plane in the 3-D joint element are assumed to be on the same plane even after the joint element has deformed. This requires fine finite element meshes if the arbitrarily curved surface is to be represented accurately. To eliminate this condition, the 3-D joint element must be improved.

A second problem is that the ground is assumed to be a linear elastic material here. As discussed in the previous chapter, yielding of the soil near the structure may precede separation or sliding at the contact surface or both may occur simultaneously. The material nonlinearity of the ground should not be overlooked nor should structural nonlinearity, such as sliding or separation. Therefore, soil material nonlinearity must also be taken into acount in three dimensional problems.

Finally, for practical purposes, the dynamic stability of the structure must be discussed on the basis of a more detailed model, with fine finite elements.

Chapter 3 references

1) Toki K., T. Sato and F. Miura: Separation and sliding between soil and structure during strong ground motion, Int. J. Earthq. Eng. Struc. Dyn., Vol.9, pp.263-277, 1981.

2) Toki K., T. Sato and F. Miura: Separation and sliding between soil and structure during strong earthquake motion, Proc. 7th WCEE, Istanbul, Vol.5, pp.312-220, 1980.

3) Toki K. and F. Miura: Non-linear seismic response analysis of a soil-structure interaction system, Proc. JSCE, No.317, pp.61-68, 1982, (in Japanese).

4) Toki K. and F. Miura: Nonlinear seismic response analysis of soil-structure interaction system, Int. J. Earthq. Eng. Struc. Dyn., (in press).

5) Goodman R.E.: Methods of geological engineering in discontinuous rocks, West Publishing Company, Ch.8, pp.300-368, 1976.

6) Mahtab M.A. and R. E. Goodman: Three dimensional finite element analysis of jointed rock slopes, Proc. 2nd Congr. ISRM, Belgrad, pp.7-12, 1970.

7) Toki K., F. Miura and T. Otake: nonlinear seismic response analysis of soil-structure interaction system by 3-dimensional joint element, Proc. JSCE, No.322, pp.51-61, 1982, (in Japanese).

8) Zienkiewicz O. C.: The finite element method, 3rd Ed., McGraw Hill, Ch.8, 1977.

9) Zienkiewicz O. C.: The finite element method, 3rd Ed., McGraw Hill, Ch.2, 1977.

Appendix 3-I

Matrix $[L_0]$ of Eq. 3-2:

$$
[L_0] = \begin{bmatrix}
-\frac{1}{4} & 0 & 0 & -\frac{1}{4} & 0 & 0 & -\frac{1}{4} & 0 & 0 & \frac{1}{4} & 0 & 0 & \frac{1}{4} & 0 & 0 & \frac{1}{4} & 0 & 0 & \frac{1}{4} & 0 \\
0 & -\frac{1}{4} & 0 & 0 & -\frac{1}{4} & 0 & 0 & -\frac{1}{4} & 0 & 0 & \frac{1}{4} & 0 & 0 & \frac{1}{4} & 0 & 0 & \frac{1}{4} & 0 & 0 & \frac{1}{4} \\
0 & 0 & -\frac{1}{4} & 0 & 0 & -\frac{1}{4} & 0 & 0 & -\frac{1}{4} & 0 & 0 & \frac{1}{2m} & 0 & 0 & -\frac{1}{2m} & 0 & 0 & \frac{1}{2m} & 0 & 0 \\
0 & 0 & -\frac{1}{2m} & 0 & 0 & \frac{1}{2m} & 0 & 0 & -\frac{1}{2m} & 0 & 0 & -\frac{1}{2\ell} & 0 & 0 & \frac{1}{2\ell} & 0 & 0 & \frac{1}{2\ell} & 0 & 0 \\
0 & 0 & \frac{1}{2\ell} & 0 & 0 & \frac{1}{2\ell} & 0 & 0 & -\frac{1}{2\ell} & 0 & 0 & \frac{1}{4m} & 0 & 0 & -\frac{1}{4m} & 0 & 0 & \frac{1}{4m} & -\frac{1}{4\ell} & 0 \\
-\frac{1}{4m} & -\frac{1}{4\ell} & 0 & \frac{1}{4m} & -\frac{1}{4\ell} & 0 & \frac{1}{4m} & \frac{1}{4\ell} & 0 & -\frac{1}{4m} & \frac{1}{4\ell} & 0 & -\frac{1}{4m} & \frac{1}{4\ell} & 0 & -\frac{1}{4m} & -\frac{1}{4\ell} & 0 & -\frac{1}{4m} & -\frac{1}{4\ell}
\end{bmatrix}
\quad \cdots\cdots (3\text{-A-}1)
$$

Appendix 3-II

Matrix $[B]_J$ of Eq. 3-7:

$$[B]_J = \begin{bmatrix}
-\frac{\ell m}{4} & 0 & 0 & 0 & 0 & -\frac{1}{4m} \\
0 & -\frac{\ell m}{4} & 0 & 0 & 0 & -\frac{1}{4\ell} \\
0 & 0 & -\frac{\ell m}{4} & -\frac{1}{2m} & \frac{1}{2\ell} & 0 \\
-\frac{\ell m}{4} & 0 & 0 & 0 & 0 & \frac{1}{4m} \\
0 & -\frac{\ell m}{4} & 0 & 0 & 0 & -\frac{1}{4\ell} \\
0 & 0 & -\frac{\ell m}{4} & \frac{1}{2m} & \frac{1}{2\ell} & 0 \\
-\frac{\ell m}{4} & 0 & 0 & 0 & 0 & \frac{1}{4m} \\
0 & -\frac{\ell m}{4} & 0 & 0 & 0 & \frac{1}{4\ell} \\
0 & 0 & -\frac{\ell m}{4} & \frac{1}{2m} & -\frac{1}{2\ell} & 0 \\
-\frac{\ell m}{4} & 0 & 0 & 0 & 0 & -\frac{1}{4m} \\
0 & -\frac{\ell m}{4} & 0 & 0 & 0 & \frac{1}{4\ell} \\
0 & 0 & -\frac{\ell m}{4} & -\frac{1}{2m} & -\frac{1}{2\ell} & 0 \\
\frac{\ell m}{4} & 0 & 0 & 0 & 0 & \frac{1}{4m} \\
0 & \frac{\ell m}{4} & 0 & 0 & 0 & \frac{1}{4\ell} \\
0 & 0 & \frac{\ell m}{4} & \frac{1}{2m} & -\frac{1}{2\ell} & 0 \\
\frac{\ell m}{4} & 0 & 0 & 0 & 0 & -\frac{1}{4m} \\
0 & \frac{\ell m}{4} & 0 & 0 & 0 & \frac{1}{4\ell} \\
0 & 0 & \frac{\ell m}{4} & -\frac{1}{2m} & -\frac{1}{2\ell} & 0 \\
\frac{\ell m}{4} & 0 & 0 & 0 & 0 & -\frac{1}{4m} \\
0 & \frac{\ell m}{4} & 0 & 0 & 0 & -\frac{1}{4\ell} \\
0 & 0 & \frac{\ell m}{4} & -\frac{1}{2m} & \frac{1}{2\ell} & 0 \\
\frac{\ell m}{4} & 0 & 0 & 0 & 0 & \frac{1}{4m} \\
0 & \frac{\ell m}{4} & 0 & 0 & 0 & -\frac{1}{4\ell} \\
0 & 0 & \frac{\ell m}{4} & \frac{1}{2m} & \frac{1}{2\ell} & 0
\end{bmatrix} \qquad (3\text{-A-}2)$$

Appendix 3-III

The three-dimensional isoparametrix element is shown in Fig. 3-A-1. The shape function matrix $[N]$ employed in this study is given as:

$$[N] = \begin{bmatrix} h_1 & 0 & 0 & h_2 & 0 & 0 & \cdots\cdots & h_8 & 0 & 0 \\ 0 & h_1 & 0 & 0 & h_2 & 0 & \cdots\cdots & 0 & h_8 & 0 \\ 0 & 0 & h_1 & 0 & 0 & h_2 & \cdots\cdots & 0 & 0 & h_8 \end{bmatrix} \tag{3-A-3}$$

$$\left.\begin{aligned} h_1 &= (1-a)(1+b)(1+c)/8 \\ h_2 &= (1-a)(1+b)(1-c)/8 \\ h_3 &= (1-a)(1-b)(1-c)/8 \\ h_4 &= (1-a)(1-b)(1+c)/8 \\ h_5 &= (1+a)(1+b)(1+c)/8 \\ h_6 &= (1+a)(1+b)(1-c)/8 \\ h_7 &= (1+a)(1-b)(1-c)/8 \\ h_8 &= (1+a)(1-b)(1+c)/8 \end{aligned}\right\} \tag{3-A-4}$$

The relationships between strain, $\{\varepsilon\}$, and nodal displacement vectors, $\{\delta\}$, are:

$$\{\varepsilon\} = [B]\{\delta\} \tag{3-A-5}$$

where,

$$\{\varepsilon\} = \{\varepsilon_X \ \varepsilon_Y \ \varepsilon_Z \ \gamma_{XY} \ \gamma_{YZ} \ \gamma_{ZX}\}^T \tag{3-A-6}$$

$$\{\delta\} = \{u_1 \ v_1 \ w_1 \ u_2 \ v_2 \ w_2 \cdots u_8 \ v_8 \ w_8\}^T \tag{3-A-7}$$

The stress-strain relationships are:

$$\{\sigma\} = [D]\{\varepsilon\} \tag{3-A-8}$$

where,

$$\{\sigma\} = \{\sigma_X \ \sigma_Y \ \sigma_Z \ \tau_{XY} \ \tau_{YZ} \ \tau_{ZX}\}^T \tag{3-A-9}$$

$$[D] = \begin{bmatrix} \lambda+2\mu & \lambda & \lambda & 0 & 0 & 0 \\ \lambda & \lambda+2\mu & \lambda & 0 & 0 & 0 \\ \lambda & \lambda & \lambda+2\mu & 0 & 0 & 0 \\ 0 & 0 & 0 & \mu & 0 & 0 \\ 0 & 0 & 0 & 0 & \mu & 0 \\ 0 & 0 & 0 & 0 & 0 & \mu \end{bmatrix} \qquad (3\text{-A-}10)$$

λ, μ: Lamé's constants

The stiffness $[k]^e$, and mass matrices of the element, $[m]^e$ are given by the equations:

$$[k]^e = \int_v [B]^T [D][B] dv$$
$$= \int_{-1}^{1}\int_{-1}^{1}\int_{-1}^{1} [B]^T [D][B] |J| \, da \, db \, dc \qquad (3\text{-A-}11)$$

$$[m]^e = \int [N] \, \rho[N] dv$$
$$= \int_{-1}^{1}\int_{-1}^{1}\int_{-1}^{1} [N]^T \rho[N] |J| \, da \, db \, dc \qquad (3\text{-A-}12)$$

where, $|J|$ is Jacobian, and the integrations are performed by Gaussian integration.

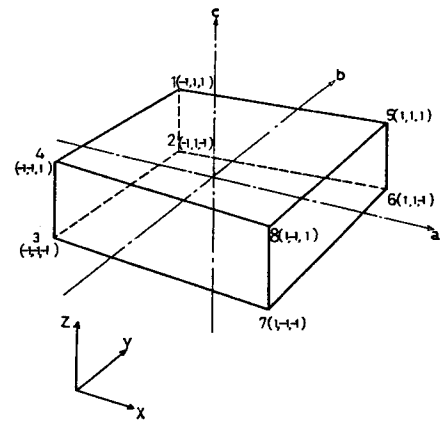

Fig. 3-A-1 An eight-nodal-point isoparametric element.

THE DYNAMIC BEHAVIOR OF INTERACTION SYSTEMS
DURING SEISMIC EXCITATION

4. Soil-Structure Systems

4.1 General remarks

Structural foundations can be classified into three categories - mat foundations, caisson foundations and pile foundations. Pile foundations are most widely used because there are a variety of types, and usable materials as well as applications. This is the result of many experimental and analytical studies of the lateral and vertical bearing capacity of a pile or a group of piles. As a pile foundation is a statically indeterminate structure in nature and the surrounding soil is very complex, even at the present time, many unknown factors still remain when a pile foundation is being designed. When the dynamic behavior and stability of pile foundation structures are investigated, dynamic soil-structure interaction should be taken into consideration and this adds further complexity and difficulty.

Theoretical studies have been based on the lumped mass model [1,2], continuum models [3-12], and the finite element method [13-18], and many experimental studies [19-22] have been performed so that much information has been accumulated. At the same time, many problems to be soilved have been left. Problems which remain include:

(i) Quantitative estimation of the shearing resistance of the pile surface,

(ii) The effects of embedment of the footing on the behavior of the structural system,

(iii) The efficiency of a group of piles.

Although it is generally recognized that the above must be clarified for dynamic excitation, most research has been performed with the static method [23-26].

The purpose of this chapter is to give a quantitative discussion of these aspects by applying the method proposed, which takes into account separation and sliding at the contact surface between soil and structure and estimates dynamic stresses on that surface [27-30].

4.2 A procedure to analyze nonlinear seismic response

(1) Modeling the soil-structure interaction system

The ground and such structures as piles, the footing and pier are assumed to be linear elastic materials which are modeled by an ordinal isoparametric element with four nodal points. The contact surface is modeled by the joint elements shown in Fig. 2-1. The stress-strain relationships of the joint element are those in Figs. 2-2(a) and (b) for normal component and tangential component, respectively.

(2) Initial stress state

In this study, the initial stress state is calculated by the following steps while giving consideration to the construction process in the field.

(i) First, the initial stresses in the ground are calculated by giving the structures below ground (the piles and the footing) the same material constants as those of the ground surrounding them. This state corresponds to the initial stress state of the ground at rest, before the pile foundation structure is constructed.

(ii) Second, the stresses for the load equivalent to the total weight of the above-ground structure, and the difference between the weight of the portion underground and that of the soil replaced by the structure. This step can be thought of as corresponding to construction

without stress disturbances in the ground.

(iii) The desired initial stress state is obtained by summing up the above stresses.

4.3 The effects of embedment of the footing on the dynamic responses of the pile-foundation structure

(1) Models analyzed

In this section, eight models, consisting of piles, the footing, the pier and the ground have been adopted in order to clarify the effects of the embedment of the footing on the dynamic responses of the system. A general view of the model is illustrated in Fig. 4-1 and their finite element meshes in Figs. 4-2 and 4-3. Table 4-1 lists the material properties, and Table 4-2 summarizes the setting conditions.

(i) Model 1- The footing is embedded. There is normal resistance on the lateral surfaces (front side) and shearing resistance on the bottom surface of the footing. Joint elements (45 elements) are arranged along all of the contact surfaces between the ground and pile-supported foundation.

(ii) Model 2- The footing is set on the surface of the ground, and there is only shearing resistance on its bottom surface. Piles have been lengthened 8 m due to the placement of the footing. Forty-nine joint elements have been used.

(iii) Model 3- Although the footing is set on the ground surface, there is no shearing resistance of the joint elements which are arranged between the footing and ground. Instead, only the piles resist horizontal force acting on the footing and the pier. The piles are 56 m in length.

(iv) Model 4- The footing is embedded, but joint elements on both sides of it have been removed. The ground and footing can thus move freely across the interface and there is no normal resistance on lateral surfaces of the footing. 43 joint elements have been used.

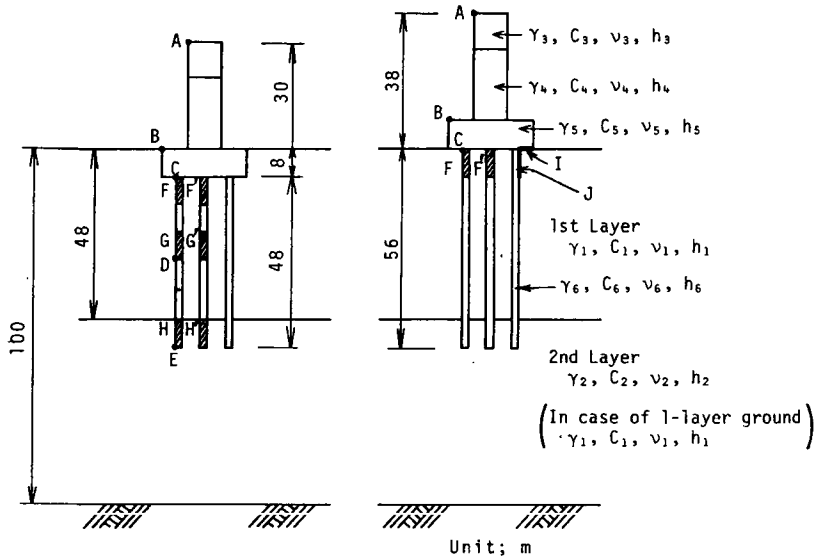

Fig. 4-1 A general view of soil-pile-structure system.

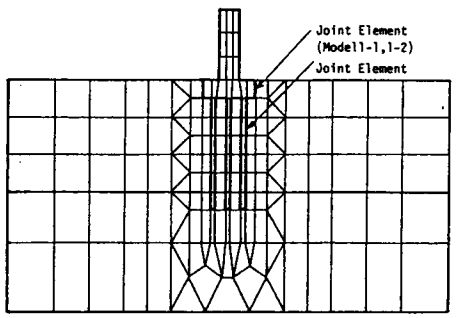

Fig. 4-2 Finite element mesh of Models 1-1, 1-2, 4-1 and 4-2.

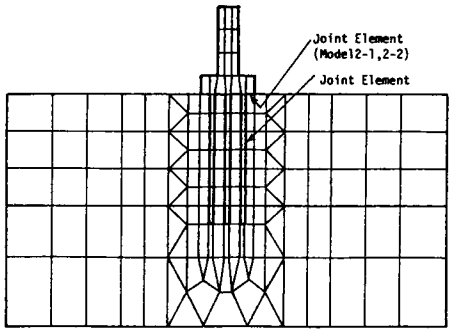

Fig. 4-3 Finite element mesh of Models 2-1, 2-2, 3-1 and 3-2.

Two types of ground composition are assumed all of the models. The first is composed of a single homogenious layer and the second of two horizontal layers. Model 1, for example, with uni-layered ground is labelled "Model 1-1" and that with bi-layered ground "Model 1-2". The shear wave velocities and thicknesses of these layers which have been listed in Table 4-1 are determined so that the two ground models have the same fundamental natural frequencies.

Table 4-1 Physical properties of the model.

	Unit weight (tf/m^3)	Shear wave velocity (m/sec)	Poisson's ratio	Damping factor
Uni-layered ground	γ_1=1.8	C_1=180	ν_1=0.333	h_1=0.20
Bi-layered ground	γ_1=1.7 γ_2=1.8	C_1=100 C_2=300	ν_1=0.333 ν_2=0.333	h_1=0.20 h_2=0.20
Sub-structure	γ_3=3.0 γ_4=2.4	C_3=1600 C_4=1600	ν_3=0.167 ν_4=0.167	h_3=0.05 h_4=0.05
Footing	γ_5=2.4	C_5=1600	ν_5=0.167	h_5=0.05
Pile	γ_6=2.4	C_6=1600	ν_6=0.167	h_6=0.05
Joint element	Normal spring const. K_n=1.0x10^6 tf/m^3 Shear spring const. K_s=3.0x10^5 tf/m^3 Cohesion C_J=10 tf/m^2 Friction angle ϕ_J=30°			

Table 4-2 Setting conditions of the models.

Condition \ Model	1	2	3	4
position of the footing (Below or on the ground surface)	below	on	on	below
Normal resistance of the front wall of the footing	exist	not exist	not exist	not exist
Shear resistance at the bottom of the footing	exist	exist	not exist	exist
Length of a pile (m)	48	56	56	48

The natural frequencies of models from which the joint elements have been removed are listed in Table 4-3. The translation mode due to shear deformation of the ground is predominant in the fundamental mode. Rocking predominant modes are those underlined in the table.

Table 4-3 Natural frequencies of the models (Hz).

Surface ground / Model / Mode	Uni-layered ground		Bi-layered ground	
	Model 1-1	Model 2-1	Model 1-2	Model 2-2
1	0.430	0.481	0.449	0.473
2	0.652	0.513	0.771	0.553
3	0.936	0.888	0.898	0.841
4	0.962	0.958	1.061	0.904
5	1.006	1.003	1.076	1.000
6	1.029	1.104	1.106	1.010
7	1.448	1.119	1.321	1.056
8	1.510	1.228	1.447	1.202

(2) The effects on structural responses

The eight models were subjected to simultaneous excitation of NS and UD components of the El Centro accelerograms under the conditions of initial stress to be discussed in section 4.4(1). The maximum accelerations were reduced to be 200 gal (NS) and 117 gal (UD). Separation for 0.2 sec took place at the contact surface between the bottom of the footing and the ground (element I in Fig 4-1) approximately 4.5 sec after excitation began, and simultaneously, sliding occurred near the pile head (element J in Fig. 4-1) in Models 2-2 and 3-2.

Figure 4-4 shows the maximum structural responses of Models 1-1, 2-1 and 4-1 normalized by those of 3-1 for uni-layered ground models and of Models 1-2, 2-2 and 4-2 normalized by those of 3-2 for bi-layered ground. Figure 4-4(a) shows the responses at the top of the pier (point A in Fig. 4-1) and (b) shows those at the top of the footing (point B in Fig. 4-1). Open circles denote normalized horizontal acceleration, triangles normalized horizontal velocity and solid circles normalized

horizontal displacement. In Fig. 4-4(a), no reduction can be seen for either Model 2-1 or Model 2-2, as compared to Models 3-1 and 3-2 in which there was no shearing resistance on the footing's bottom surface. This means that this resistance does not affect structural dynamic responses.

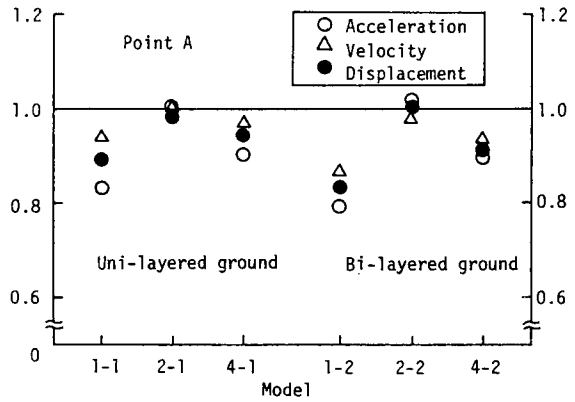

(a) Point A - Top of the pier

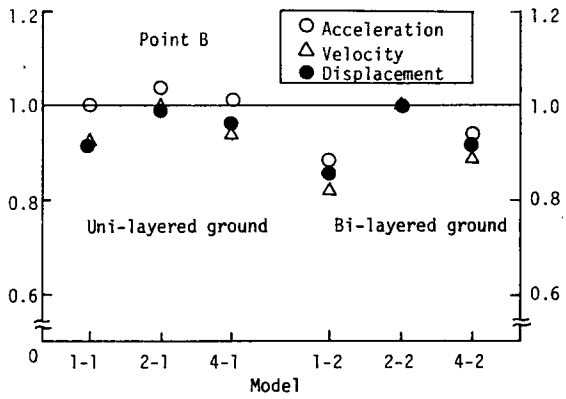

(b) Point B - On the footing

Fig. 4-4 Maximum response values normalized by those of Models 3-1 or 3-2.

There are two causes of reductions in responses of Models 1-1, 1-2, 4-1 and 4-2 over those of 3-1 and 3-2. One is the effect of the embedment of the footing and the other is the effect of differences in pile length. A reduction of 5 ∿ 10 % can be seen in Models 4-1 and 4-2, which may be attributed to differences in pile length because normal resistance on the lateral walls of the footing does not exist in these models. Namely, these two models can be regarded as those in which the footing has been constructed above the ground.

In the case of Models 1-1 and 1-2, a reduction in the response has obviously been caused by both of embedment of the footing and pile length differences. As the reduction due to the latter is, however, no more than the degree for Models 4-1 and 2-1, the differences between 4-1 and of 1-1 (or between 4-2 and 1-2) is due to embedment giving rates lower by 5 ∿ 10 %. Besides, the reductions are caused by normal resistance on the lateral walls of the footing since shearing resistance on its bottom surface cannot be expected.

These tendencies are dominant in the decreasing order of acceleration, displacement and velocity, and are more remarkable for bi-layered than uni-layered ground. The maximum response values are listed in Table 4-4.

Table 4-4 Maximum response values.

Position \ Item \ Model		1-1	2-1	3-1	4-1	1-2	2-2	3-2	4-2
Point A	Acceleration (gal)	105	127	126	112	183	235	230	201
	Velocity (kine)	47	50	50	48	50	57	58	51
	Displacement (cm)	13.4	14.9	15.0	14.1	17.3	20.6	20.7	18.3
Point B	Acceleration (gal)	87	91	87	88	107	122	121	111
	Velocity (kine)	40	43	43	41	37	45	45	38
	Displacement (cm)	11.2	12.0	12.1	11.5	12.7	14.7	14.7	13.1
Point C	Displacement (cm)	10.7	11.4	11.4	10.9	11.6	13.3	13.3	11.9
Point D		8.4	9.0	9.0	8.4	6.3	8.0	8.0	6.3
Point E		5.7	5.6	5.6	5.7	2.2	2.2	2.2	2.2

(3) The effects on dynamic stresses in piles

Figure 4-5 shows the dynamic stresses developed in the element near the pile head (element F in Fig. 4-1) normalized by those of Models 3-1 or 3-2 which correspond to the composition of the ground. The normal stress σ_y, i.e., the compressive stress is denoted by open circles and the shear stress, τ_{xy}, by triangles. Remarkable amount of stress reduction can be observed in Models 1-1 and 1-2 which have embedded footings. The stress reduction of τ_{xy} is greater than that of normal stress, σ_y, especially for Model 1-1. Reductions of approximately 10 % are observed in Models 4-1 and 4-2 for the same reason mentioned above. On the other hand, Models 2-1 and 2-2 show only slight reduction in stress. Judging from this, the normal resistance on the lateral walls of the footing plays an important role in reducing pile stresses.

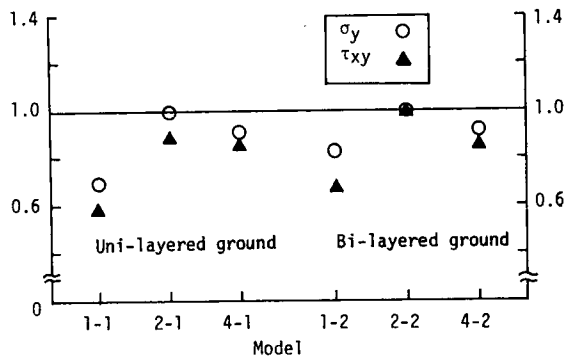

Fig. 4-5 Maximum response stresses at the pile head normalized by those of Models 3-1 or 3-2.

(4) The effects on the bending moment in piles

In order to estimate the bending moment which develops in the piles. New models in which a pile is modeled by two rows of elements have to be introduced. Figure 4-6 schematic diagram of the method by which the bending moment has been calculated. The relationships between the bending moment, M, and normal stresses, σ_a and σ_b, in elements A and B (Fig. 4-6) are given by:

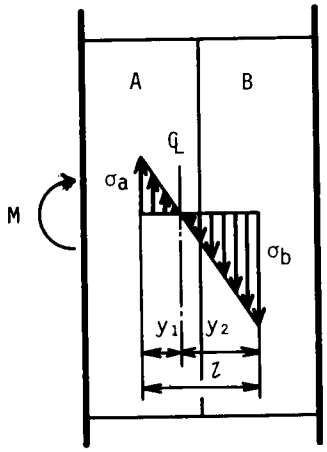

Fig. 4-6 The relationship between bending moment, M, and normal stresses, σ_a and σ_b.

$$\left.\begin{aligned}\sigma_a &= -\frac{M}{I} y_1 \\ \sigma_b &= \frac{M}{I} y_2\end{aligned}\right\} \qquad (4\text{-}1)$$

From Eq. 4-1 and with the stipulation that $y_1+y_2 = l$, the bending moment, M, is given by Eq. 4-2.

$$M = \frac{I}{l}(-\sigma_a+\sigma_b) \qquad (4\text{-}2)$$

where, I is the moment of inertia of area of the pile and l, the distance between the centers of elements A and B.

Figures 4-7 and 4-8 show the distributions of maximum dynamic bending moment along the piles. Figure 4-7 is for the bi-layered ground models and Fig. 4-8 is for the uni-layered ground models. Models 1-1 and 1-2 are shown in (a) and Models 3-1 and 3-2 in (b).

By comparing Figs. 4-7(a) and (b), the bending moment of Model 1-2 is found to be less than half of Model 3-2, the effect of embedment of the footing. This, however, does not always reduce the bending moment, as it is true in Fig. 4-8.

Attention should be paid to the fact that a large amount of moment develops near the interface between the layers of bi-layered ground.

4.4 Load sharing mechanisms of piles and footing

(1) The initial stress state on the surfaces of piles and footing

The initial vertical stresses on the surfaces of the piles and footing are illustrated in Fig. 4-9. Shear stress corresponds to those on the vertical, and normal stress to those on the horizontal contact surfaces. Figure 4-9(a) shows Model 1-1 and (b) Model 1-2. These stresses are caused by the structure's dead load or the load in step(ii)

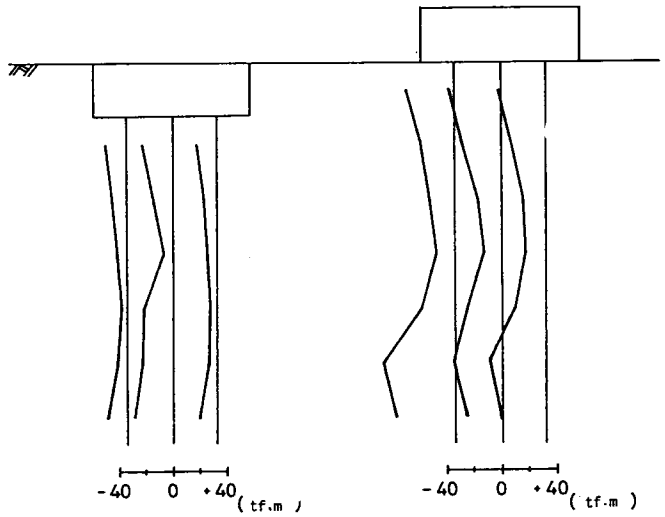

(a) Model 1-2 (b) Model 3-2

Fig. 4-7 Maximum bending moment distribution.

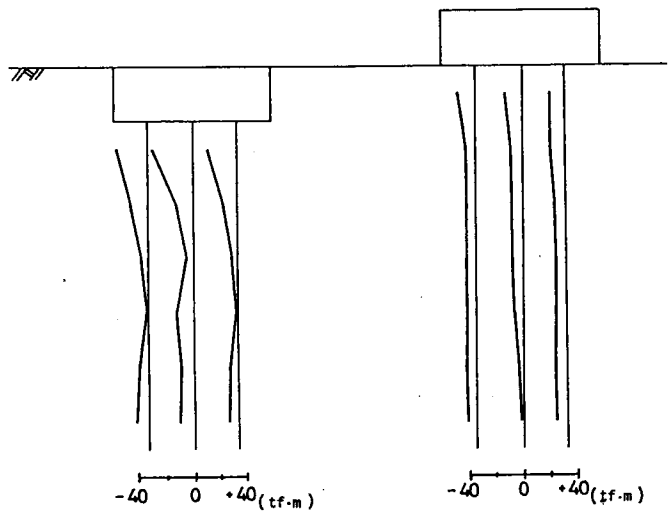

(a) Model 1-1 (b) Model 3-1

Fig. 4-8 Maximum bending moment distribution.

(section 4.2.(2)). Differences can be observed in the shear stress distributions of the two models - it is approximately uniform over the contact surfaces in Model 1-1, but is concentrated near the pile tip in Model 1-2.

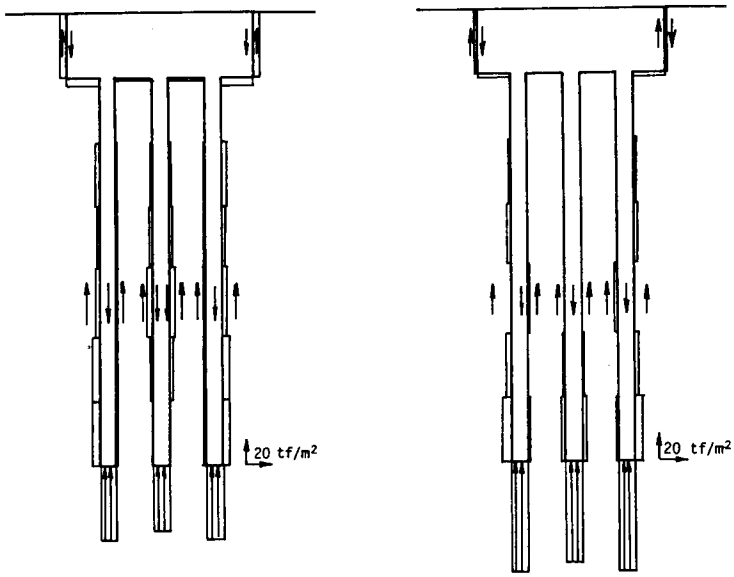

(a) Model 1-1 (b) Model 1-2

Fig. 4-9 Initial stress distribution along the contact surface.

The forces on the contact surfaces are obtained by multiplying the length of the joint element by the stress in the element. The forces are divided into four components, the shearing and the normal resistance forces of the footing and the piles. These four components are shown in percentages in Fig. 4-10. The numbers in parentheses are the shared forces (tf/m). The shared rate at pile tips is about 38 % and the 62 % remainder is of the footing and pile surfaces in Model 1-1. The shared rate at pile tips is about 64 % in Model 1-2. Pile foundation of Model 1-1 where the ground has only one layer can be divided into friction piles and pile foundation in Model 1-2 which has two layers can be divided into the point bearing piles. Other models can also be divided according to these two pile supporting mechanisms based on ground composition.

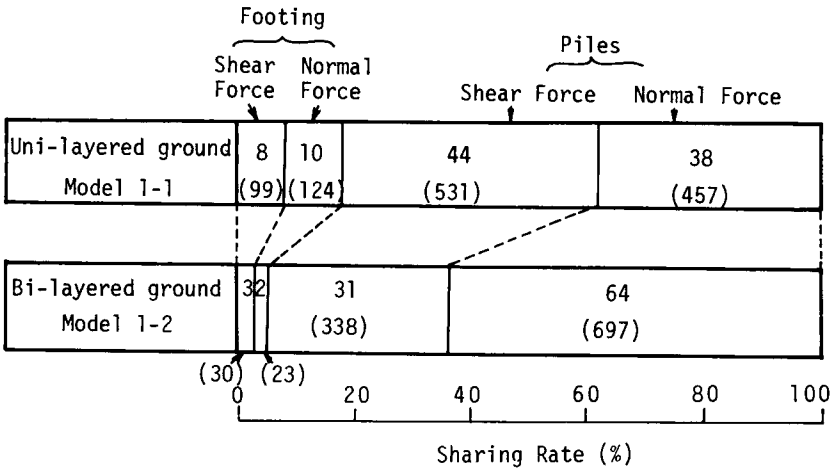

Fig. 4-10 The shared rate of the dead load.

(2) The mechanism of sharing among piles in a foundation

Resistance of vertical load by the pile footing foundation can be classified into several components:

(i) the normal resistance on the pile tip,

(ii) the shearing resistance on the pile surface,

(iii) the normal resistance on the bottom surface of the footing.

(iv) the shearing resistance on the lateral walls of the footing,

Those of horizontal load are:

(v) the normal resistance on the pile surface,

(vi) the shearing resistance on the pile tip,

(vii) the normal resistance on the lateral walls of the footing,

(viii) the shearing resistance on the lateral walls of the footing,

(ix) the shearing resistance on the bottom surface of the footing.

As the system is modeled for two-dimensional plane strain, component (viii) is not treated because it can only be evaluated precisely by the three-dimensional model.

(a) The mechanisms to share vertical seismic forces

The maximum vertical dynamic stresses on pile and footing surfaces

are illustrated in Fig. 4-11. Figure 4-11(a) shows Model 1-1 and (b) Model 1-2. The stresses at the bottom of the footing and pile tips are normal stresses and those at the lateral walls of the footing and pile surfaces are the shear stresses.

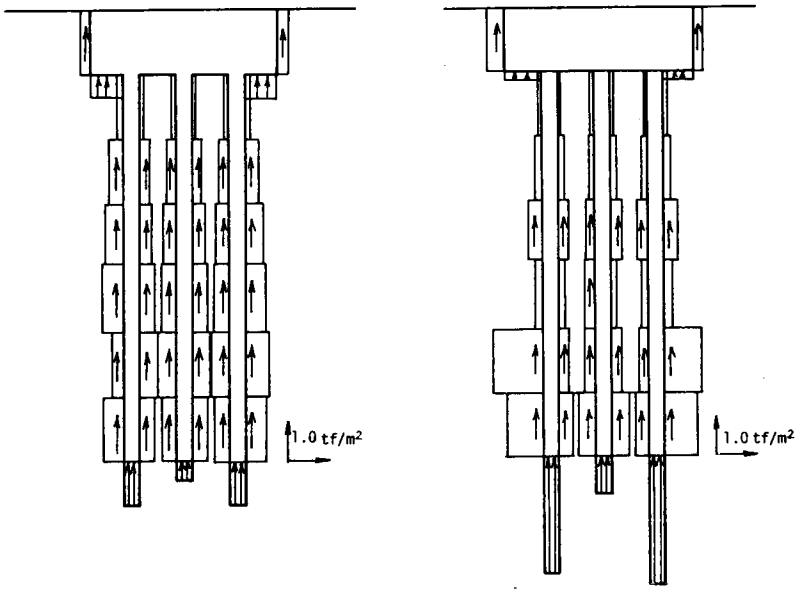

(a) Model 1-1 (b) Model 1-2

Fig. 4-11 Dynamic stress distribution along the contact surface.

Sharing rate at the pile tips of Model 1-2 is greater than that of Model 1-1. The stress distribution again concentrates near the pile tip in Model 1-2, but is approximately uniform over the entire surface in Model 1-1. As in the case of dead load, there are four components and the sharing rates obtained from the dynamic stresses are shown in Fig. 4-12. Although there are shearing resistances on the lateral walls of the footing in Models 1-1 and 1-2, the rates are less than 4 ∿ 6 % and they may therefore be disregarded. However, the normal resistance on the bottom surface of the footing is less than 10 % and for all models the total rates, the sum of shearing and normal resistances, at the footing are no greater than 10 %.

Most of the seismic force is shared by the piles and most of it consists of shearing resistance on pile surfaces. The rate is 80 ∿ 85 % for the uni-layered ground models and 70 ∿ 80 % for the bi-layered ground model. The sharing rates of the footing and piles as much as 90 % for the uni-layered ground models and 75 ∿ 80 % for bi-layered ground models. The remaining 10 %, or 15 ∿ 25 % is shared by the pile tips, and the values have been extremely reduced when the values of 38 % and 64 % obtained for the dead load are considered.

(b) The mechanisms to share horizontal seismic forces

Figure 4-13 shows the sharing rates among horizontal components.

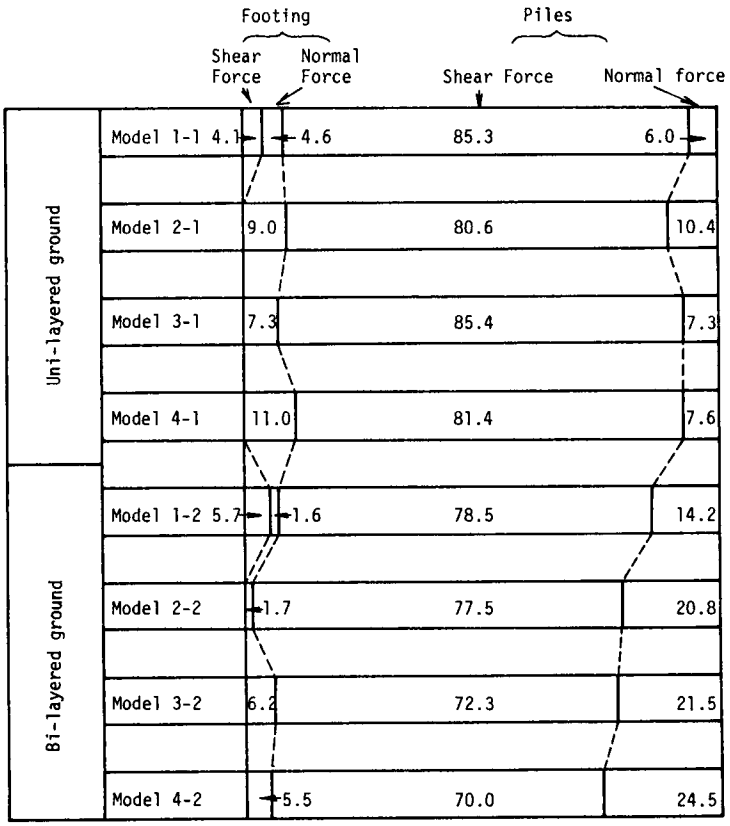

Fig. 4-12 The rate of vertical seismic force which is shared.

The normal resistances on the lateral walls of the footing for both Models 1-1 and 1-2 are about 20 %, but the shearing resistances on the bottom surface of the footing are an insignificant 1 ∿ 2 %.

In Models 2-1 and 2-2, shearing resistances on the bottom surface of the footing range from 50 to 100 % of normal resistances on the lateral walls of Models 1-1 and 1-2. However, the influence of shearing resistance on structural responses can be disregarded whether the shearing resistance is taken into account. However, in the case of designing piles which have large radii, there is some indication that the shearing resistance at the pile tip should be taken into consideration[31], although here it was not deemed necessary.

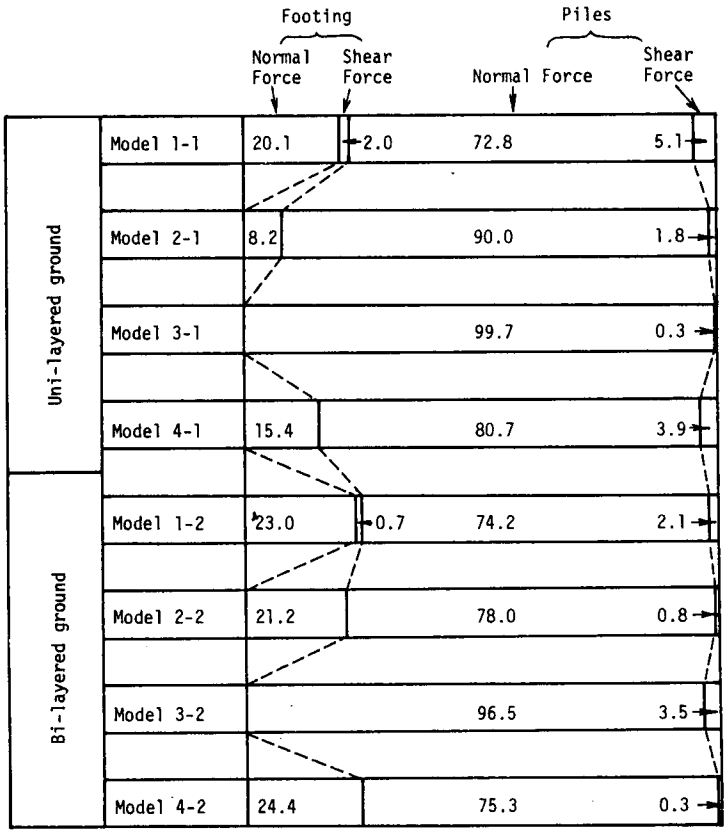

Fig. 4-13 The rate of horizontal seismic force which is shared.

4.5 A comparison of responses obtained by the seismic coefficient method and those by the method proposed

(1) Models and assumptions of the seismic coefficient method

In this section, structural responses obtained by the proposed method are compared with those obtained by the seismic coefficient method which is practically used for designing. For this purpose, two models have been introduced (Figs. 4-14(a) and (b)). The first is Model S1 and it is set up with the same pier and footing as of previous models and modified piles and ground. The pile length is 33 m, the thickness of the ground is 50 m and the shear wave velocity of the upper layer is raised to 150 m/sec. The second is Model S2. The footing and pier have been reduced as shown in Fig. 4-14(b) in order to examine the influence of the scale of the structure on its responses. The fundamental natural period of the ground is about 0.93 sec, while those of previous ground models were in the range of 2.0 sec.

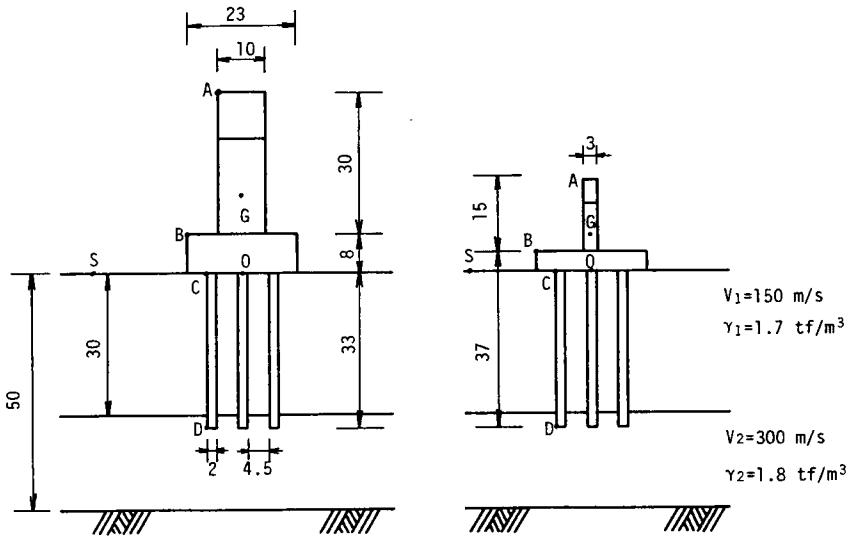

(a) Model S1 (b) Model S2

Fig. 4-14 A general view of soil-pile-structure models.

The analyses by the seismic coefficient method are performed under the following conditions[32]:

(i) that the thickness of a pile is 2 m, and equal to the diameter of the pile,

(ii) that the horizontal seismic coefficient is 0.2 and is applied only to the structure above the ground surface. The vertical seismic coefficient is disregarded.

(iii) and that the coefficient of horizontal subgrade reaction is calculated from the N value and the N value is calculated by the equations from the shear wave velocity[33]:

for cohesive soil:

$$V_s = 80N^{\frac{1}{3}} \quad (1 \leqq N \leqq 50) \tag{4-3}$$

for sandy soil:

$$V_s = 100N^{\frac{1}{3}} \quad (1 \leqq N \leqq 25) \tag{4-4}$$

Dynamic response analyses were also performed on the present models. They were subjected to horizontal seismic excitation (the El Centro (1940) NS component) whose maximum amplitude was lowered to 100 gal.

(2) Results and discussion

Table 4-5 lists the maximum responses for each point in Fig. 4-14, and Table 4-6 lists the displacements, rotational angles of the footing and the vertical reaction at the pile head obtained by both dynamic and static analyses.

Table 4-5 Maximum response values for Models S1 and S2.

Model	Item	Point					
		G	A	B	C	D	S
S1	Acceleration (gal)	174	303	128	89	85	169
	Velocity (kine)	32.2	52.7	25.0	18.7	6.2	22.5
	Displacement (cm)	5.29	8.78	4.08	3.14	0.61	2.20
S2	Acceleration (gal)	184	249	180	173	87	152
	Velocity (kine)	27.2	32.9	26.7	25.6	5.5	22.9
	Displacement (cm)	3.74	4.49	3.67	3.52	0.7	2.85

Judging from the data, the structure and the surrounding soil vibrate at the same rate, although structural responses of Model S2 slightly more than those of soil. However, the responses of the footing of Model S1 differ from those of the surrounding soil due to its greater structural inertia. As shown in Table 4-6, the dynamic analysis relative displacement between the pile head and the surrounding soil (point C - point S) is 0.94 cm, a value smaller than the value by static analysis. The divergence is attributed to the large structural mass which constrains the behavior of the ground. In Model S2, agreement is good as the displacements are 0.67 cm and 0.77 cm respectively.

Table 4-6 A comparison of the maximum response values from the dynamic and static analyses.

Model	Item	Dynamic analysis	Static analysis
S1	Relative displacement between point C and S	0.94	2.96
	Rotational angle of the footing	0.149×10^{-2}	0.133×10^{-2}
	Reaction at the pile head	724	697
S2	Relative displacement between point C and S	0.67	0.77
	Rotational angle of the footing	0.511×10^{-3}	0.197×10^{-3}
	Reaction at the pile head	138	103

The vertical loads at the pile head of the left pile in Fig. 4-14 have been tabulated in Table 4-7, divided into two components- the shearing resistance on the pile surface and the normal resistance at the pile tip. Although the shared rate at the pile tip is larger than that on the pile surface for dead load, for seismic load, this situation is reversed, a tendency which agrees with the results from section 4.4.

The total load which acts on the pile during earthquakes equals dead plus seismic loads. The loads shared by the pile surfaces and the pile tip are 717 tf/m and 843 tf/m respectively in Model S1. If the

structure is hit by stronger earthquakes, the shared load on the pile surface may exceed that on the pile tip. Furthermore, since the rate on the pile surface in uni-layered ground is higher than that in bi-layered ground, the load shared on the pile surface is dominant during strong earthquakes. This means that ground in which there is a large amount of resistance is advantageous if the pile foundation structure during earthquakes is to be maintained.

Nevertheless, the Specifications for Highway Bridges which was recently revised do not refer to either individual bearing capacities of the pile surface's shearing resistance or to normal resistance at the pile tip. Although the safety factor obtained by the specifications is for the total load at the pile head, the safety factor of the shearing resistance and that of the normal resistance can be separately assessed by the proposed method [32]. In other words, this new method provides for rational design. It is therefore necessary to perform detailed examinations of the mechanisms by which piles share dead and seismic loads, depending on the composition and property of the ground.

Table 4-7 A comparison of the reaction at the pile head from dynamic and static analyses.

Model \ Analysis method / Load		Dynamic analysis			Static analysis
		Pile surface	Pile tip	Total	
S1	Dead load	203 (24.3%)	633 (75.7%)	836	762
	Seismic load	514 (71.0%)	210 (29.0%)	724	697
	Total	717	843	1560	1459
S2	Dead load	60 (24.1%)	189 (75.9%)	249	225
	Seismic load	87 (63.0%)	51 (37.0%)	138	103
	Total	147	240	387	328

4.6 Dynamic characteristics of a group of piles

(1) Models

In order to clarify the dynamic characteristics of a group of piles, dynamic response analyses have been performed for models of foundations with either one single pile or a group of piles. A pile-supported footing model will be introduced here. Its finite element mesh is shown in Fig. 4-15. The model consists of five piles are named Model G5. The piles are numbered No.1, ∿ 5 respectively. Joint elements are arranged along the bottom surface of the footing. This type of mesh is used even for models with a single pile (Model G1), two piles (Model G2) and three piles (Model G3). Pile material constants are No.3 in Model G1, No.1 and No.5 in Model G2 and No.1, No.3 and No.5 in Model G3 and the remaining figures refer to ground material constants. The ground is composed of two layers and the material constants are listed in Table 4-2. The pile diameter, D, is 2 m and its spacing, d, is 6.5 m (d/D=3.25).

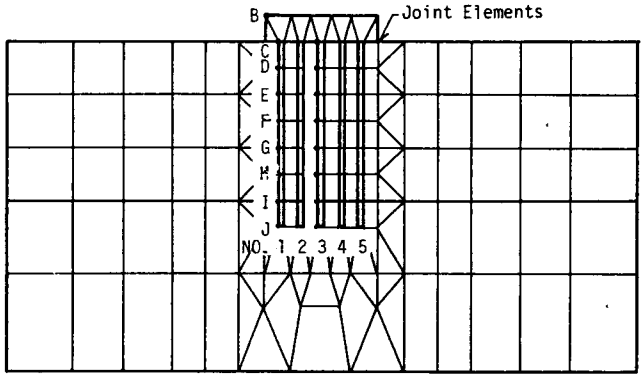

Fig. 4-15 The finite element mesh of a group of piles.

(2) Dynamic lateral group efficiency

The maximum responses are summarized in Fig. 4-16. In these analyses, NS (max. 200 gal) and UD (max. 117 gal) components of the El Centro (1940) accelerograms are the input excitations, with (a), the horizontal

acceleration, (b), the horizontal velocity and (c), the horizontal displacement at each point (point B ∿ J in Fig. 4-15). Horizontal displacements are shown in Fig. (d) where the footing has been subjected to a static force equivalent to a 0.2 seismic coefficient. Shearing resistance on the bottom surface of the footing has not been taken into account here and, therefore, the entire force acting on the footing is resisted by the piles alone.

As can be seen from Fig. 4-16, there is a slight difference between the velocity and displacement responses, although the magnitude of the values are apt to decrease as the pile numbers increase in the dynamic analyses. Moreover, there is no difference in acceleration. While, there are significant differences in static analyses (Fig. 4-16(d)).

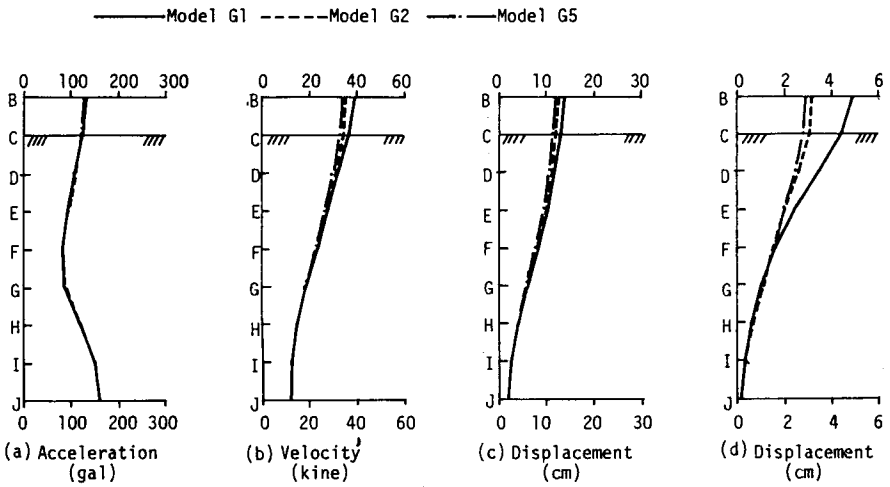

Fig. 4-16 A comparison of the maximum response where shearing resistance between the bottom of the footing and the ground does not exist.

Once dynamic lateral group efficiency has been determined for each model from the displacements at the pile head, dynamic characteristics of the group of piles can be compared to the results of static analyses. There are some definitions of the lateral group efficiency[7] and the one defined by Eq. 4-7 has been adopted in this study.

$$e=\frac{y_0}{ny_G} \tag{4-7}$$

where, e the lateral group efficiency, y_0, the displacement at the pile head of a single pile, n, number of piles in the group, and y_G, the displacement at the pile head of the group. According to the definition, $e=1$ when an individual pile in the group independently resist the load as much as would a single pile, and $e=1/n$ when the entire group resist the load to the same degree as would a single pile. In general, the value of e falls between 1 and $1/n$.

The maximum horizontal displacements at the pile head are listed in Table 4-8 for four models and e, calculated from the displacements are listed in Table 4-9. The efficiencies for seismic load nearly equal $1/n$, and are smaller than those obtained for static load. This dissimilarity is because when there is static load, as the ground is at rest, there are soil reactions to each pile, while, when the load is seismic, as the piles move simultaneously with the ground, there is no soil reaction for each pile, and lower efficiencies result.

Table 4-8 Maximum response displacement where shearing resistance between the bottom of the footing and the ground does not exist.

External force \ Model	G1	G2	G3	G5
Seismic force	13.05	11.92	11.59	11.09
Static force	4.34	3.04	2.90	2.74

Table 4-9 A comparison of lateral group efficiencies where shearing resistance between the bottom of the footing and the ground does not exist.

External force \ Model	G2	G3	G5
Seismic force	0.547	0.375	0.235
Static force	0.714	0.499	0.317
1/n	0.500	0.333	0.200

Figure 4-17 shows soil reactions on each pile surface at the moment when the lateral seismic load is at a maximum for the eight models from section 4.4(1). Most of the seismic load is shared by the front pile and the rear pile hardly react. This is a means to explain the reduction of lateral group efficiency during dynamic load.

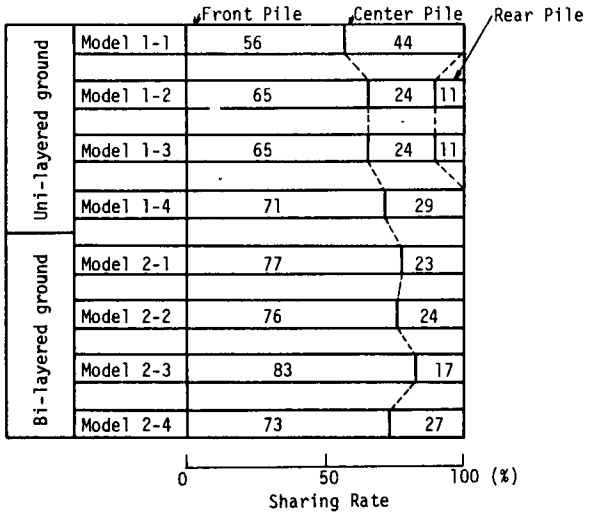

Fig. 4-17 A comparison of the rate of horizontal seismic force shared.

Finally, in order to examine the influence of the pier on lateral group efficiency, the pier in Fig. 4-1 is attached to the footing shown in Fig. 4-15 and the analyses are repeated. Figure 4-18 shows the maximum responses. Point A indicates the top of the pier, and the shearing resistance on the bottom of the footing is taken into account. These models are called by the same names, such as Model G1, etc. Differences in response arise even for dynamic excitation, and the phenomenon would not have been observed in the models without a pier. Besides, the responses of Model G5 are, in general, not less than those of Model G2. Acceleration and displacement of Model G5 are 30 % greater than those of Model G2 at the top of the pier (point A) and 15 % greater at the pile

head (point C). The responses of Model G1 are the smallest of all for acceleration and velocity, and even for displacement, this is true at the top of all piers except that of Model G2. That is, an increase in the number of piles increases rather than reduces structural responses. For static load, however, the displacement decreases with an increase in pile numbers.

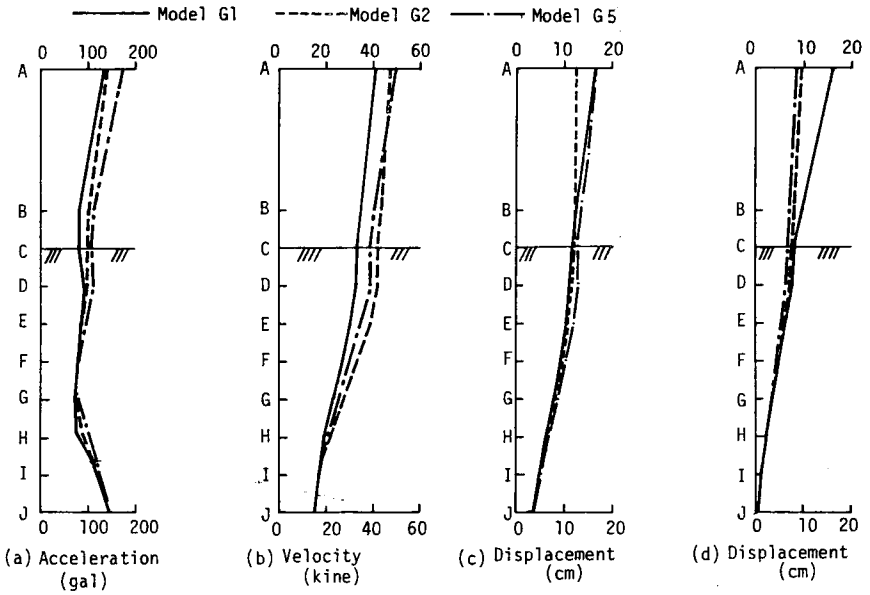

Fig. 4-18 A comparison of maximum responses.

Table 4-10 lists lateral group efficiencies and those obtained for sinusoidal excitation (200 gal, 1.0 Hz), the S82E and UD components of the J.P.L. accelerograms and the EW and UD component of the Hachinohe accelerograms have also been tabulated. In the cases of sinusoidal excitation and the El Centro accelerograms, lateral group efficiencies are less than $1/n$, but the Hachinohe efficiency for Model G2 equals $1/n$.

The results here indicate that it is necessary to take into the effects of dynamic lateral group efficiency consideration when pile foundations have been designed by the seismic coefficient method, because

the lateral group efficiency for dynamic excitation is essentially different from that for static load.

Table 4-10 A comparison of lateral group efficiencies where the pier's influence is taken into account.

External force \ Model		G2	G5
Seismic force	El centro	0.447	0.159
	Hachinohe	0.500	0.217
	J.P.L.	0.532	0.222
Sinusoidal force		0.432	0.190
Static force		0.573	0.237
1/n		0.500	0.200

4.7 Conclusions

The dynamic characteristics of pile-foundation structures were examined by the finite element method in order:

(i) to clarify the effects of embedment of the footing on dynamic structural responses,

(ii) to estimate quantitatively the frictional resistance of pile surfaces,

(iii) to determine the dynamic lateral efficiency of a group of piles.

The results obtained follow.

(1) By embedding the footing, there was a response reduction of approximately 5 ∿ 10 %. Stresses which had developed in the pile were also reduced and for the pile head in particular, a 40 % reduction in shear stress was observed.

(2) For dynamic load, the total shared rates of shearing resistance on the pile surface and normal resistance of the footing were 80 ∿ 85 % for vertical load when the footing was embedded, while 40 ∿ 60 % in the case of dead load.

(3) After a detailed investigation of shearing resistance on the pile surface and normal resistance at the pile tip, the shared rate of normal stress is predominant for dead load, on the contrary, the shearing resistance is predominant for dynamic load.

(4) The safety factor of shearing and normal resistance can be separately assessed by the proposed method, offering the possibility of a more rational and ecomomical design of the pile foundation.

(5) Relatively good agreement was found between the present and seismic coefficient methods for displacement of pile foundations and the vertical load acting on the pile head.

(6) Very different results were obtained for lateral group efficiency during dynamic or static load. As the number of piles increased, for static load, the displacement decreased but, for dynamic load, structural responses increased. Therefore, it is necessary to take the dynamic lateral group efficiency into consideration when pile foundations are designed by the seismic coefficient method.

Although this system is modeled two-dimensionally, the results are both significant and suggestive. The next task, however, is to model foundation structures more realistically or on the basis of a typical three-dimensional structures.

Chapter 4 references

1) Penzien J., C. F. Scheffey and R. A. Parmelee: Seismic analysis of bridges on long piles, Proc. ASCE, Vol.90, No.EM3, pp.223-254, 1964.

2) Penzien J.: Soil-pile foundation interaction, Earthquake Engineering, R. L. Wiegel, et al., Eds., Prentice-Hall, Inc., Englewood Cliffs, N. J., pp.349-381, 1970.

3) Novak M.: Dynamic stiffness and damping of piles, Can., Geotech, J., Vol.11, pp.574-598, 1974.

4) Satter M. A.: Dynamic behavior of partially embedded pile, Proc. ASCE, No.GT7, July., pp.775-785, 1976.

5) Nogami T. and M. Novak: Soil-pile interaction in vertical vibration, Int. J. Earthq. Eng. Struc. Dyn., Vol.4, pp.277-293, 1976.

6) Novak M.: Vertical vibration of floating piles, Proc. ASCE, No.EM1, Feb., pp.153-168, 1977.

7) Novak M. and J. F. Howell: Torsional vibration of pile foundations, Proc. ASCE, No.GT4, April, pp.271-285, 1977.

8) Nogami T. and M. Novak: Resistance of soil to horizontally vibrating piles, Int. J. Earthq. Eng. Struc. Dyn., Vol.5, pp.249-261, 1977.

9) Novak M. and T. Nogami: Soil-pile interaction in horizontal vibration, Int. J. Earthq. Eng. Struc. Dyn., Vol.5, pp.263-281, 1977.

10) Novak M. and J. A. Ella: Impedance functions of piles in layered media, Proc. ASCE, No.EM3, June, pp.643-661, 1978.

11) Kuhlemeyer R. L.: Vertical vibration of piles, Proc. ASCE, No.GT2, Feb., pp.273-287, 1979.

12) Kagawa T. and L. M. Kraft: Dynamic characteristics of lateral load-deflection relationships of flexible piles, Int. J. Earthq. Eng. Struc. Dyn., Vol.9, pp.53-68, 1981.

13) Kausel E. and J. M. Roesset: Dynamic stiffness of circular foundations, Proc. ASCE, Vol.101, No.EM6, Dec., pp.771-785, 1975.

14) Nagaoka H., E. Yoshida and N. Sasaki: Finite element vibration anal-

ysis of a well foundation composed of steel piles and comparison with field test result, Proc. JSCE, No.254, Oct., pp.61-72, 1976. (in Japanese).

15) Randolph M. F. and C. P. Wroth: Analysis of deformation of vertically loaded piles, Proc. ASCE, No.GT12, Dec., pp.1465-1488, 1978.

16) Ottaviane M.: Observed and predicted test pile behaviour, Int. J. for Numerical and Analytical Methods in Geomechanics, Vol.3, pp.131-143, 1979.

17) Toki K., F. Miura and M. Noguchi: Point bearing force and friction force of pile foundation during strong earthquake excitation, 35th Proc. Ann. Meeting of JSCE, I-231, 1980, (in Japanese).

18) Toki K., F. Miura, M. Noguchi, Non-linear behaviour of pile foundation during strong earthquake motion, Ann. of Disas. Prev. Res. Inst., Kyoto Univ., No.24, B-2, pp.1-22, 1981, (in Japanese).

19) Novak M. and R. F. Grigg: Dynamic experiments with small pile foundation, Can. Geotech., J., Vol.13, pp.372-385, 1976.

20) Kim J. B. and R. J. Brungraber: Full-scalled lateral load tests of pile groups, Proc. ASCE, No.GT1, Jan., pp.87-105, 1976.

21) Kim J. B., L. P. Singh and R. J. Brungraber: Pile cap soil interaction from full-scale lateral load tests, Proc. ASCE, No.GT5, May, pp.643-653, 1979.

22) Garg K. G.: Bored pile groups under vertical load in sand, Proc. ASCE, No.GT8, Aug., pp.939-956, 1979.

23) Iseta T., Y. Tanahashi and T. Higuchi: The estimation of friction force on pile surface by the finite element method, 14th Proc. Ann. Meeting of JSSMFE, pp.989-992, 1979, (in Japanese).

24) Yamashita K., M. Hanno and E. Yoshida: Examples of analyses of the stress increments in the ground due to friction piles, 14th Proc. Ann. Meeting of JSSMFE, pp.777-780, 1979, (in Japanese).

25) Yoshida I., H. Tada and T. Yamane: The lateral group efficiency of large scale pile foundations, 27th Proc. Ann. Meeting of JSCE,

pp.403-406, 1972, (in Japanese).

26) Taga N. and Y. Togashi: Dynamic analysis of the fundamental characteristics of the ground and pile groups by the finite element method, 13th Proc. Ann. Meeting of JSSMFE, pp.1077-1080, 1978, (in Japanese).

27) Toki K., T. Sato and F. Miura: Separation and sliding between soil and structure during strong earthquake motion, Proc. 7th WCEE, Istanbul, Vol.5, pp.213-220, 1980.

28) Toki K., T. Sato and F. Miura: Separation and sliding between soil and structure during strong ground motion, Int. J. Earthq. Eng. Struc. Dyn., Vol.9, pp.263-277, 1981.

29) Toki K. and F. Miura: Non-linear seismic response analysis of soil-structure interaction systems, Proc. JSCE, No.317, pp.61-68, 1982, (in Japanese).

30) Toki K., F. Miura and T. Otake: Non-linear seismic response analysis of soil-structure interaction system by 3-dimensional joint element, Proc. JSCE, No.322, pp.51-61, 1982, (in Japanese).

31) Asanuma H.: Problems of 'Specifications for the design of highway bridges- Part IV (Substructures)' and its future directions, Civil Engineering Journal, Public Works Research Center, Vol.22, No.5, pp.12-14, 1980, (in Japanese).

32) Toki K., S. Emi and F. Miura: Nonlinear behavior of pile foundations during strong earthquake motion, the Bridge and Foundation Engineering, Vol.16, No.9, pp.47-51, 1982, (in Japanese).

33) Specifications for the design of highway bridges, Part IV, (Substructures), the Japan Road Association, 1980, (in Japanese).

5. Soil-Rock Systems

5.1 General remarks

The failure of numerous slopes are reported after almost every major earthquake in Japan. There has been a great deal of damage not only to property but also to people due to slope failures[1-4]. The rate of casualties has increased in suburban hills where the population has increased most rapidly. Slope failures often accompanied by the failure of life-line systems such as water and gas supply systems. Breakdowns in the transportation system due to slope failure further delay relief and repair services.

The influence of slope failure on daily life is greater each year[5], and a rational method to dynamically estimate the slope stability during earthquakes is of increasing importance. At present that most commonly used is the sliding circle method which is based on the seismic coefficient method. After the Izuhanto-oki earthquake in 1974 in which more than twenty peoples were killed by the slope failure[6], dynamic analyses were initiated using numerical methods[7-9]. These, however, were limited to linear analyses. Toki et al.[10] examined the stability of the existing slope at the critical states by employing joint elements.

The stability of the same slope as Toki examined is quantitatively investigated in detail by examining soil material nonlinearity and the effect of ground water with a simple model of pore water pressure buildup. The assessment of the slope stability is made after sheetpiles have been driven into the slope.

5.2 Static analyses of slope stability using the finite element method

(1) The model analyzed

For an analysis of slope stability, the sliding circle, Bishop's and Janbu's methods are practically used, the choice of method depending on the shape of sliding surface[11]. Although all are valid for static force, slope stability during dynamic forces can no longer be estimated by these classical methods. The finite element method, however, makes it possible to estimate the dynamic stability of slopes during earthquakes, and the safety factor against sliding of the slope can, in particular, be directly estimated by adopting joint elements set along an arbitrary sliding surface.

Before any dynamic stability analysis is performed, static analyses are made by the finite element method and the results are compared with those obtained from classical methods in order to check their compatibility.

Figure 5-1 is a cross section of an actual slope analyzed in this study. The slope is composed of banking and weathered rock under which lie slate basal rock, as determined by boring tests[12]. The shear, v_s, and volumetric, v_p, wave velocities of each layer were obtained by P-S tests. The material constants obtained by laboratory tests are listed in Table 5-1. However, the cohesion is parametrically changed to 0.02, 0.05 and 0.1 kgf/cm^2 in the following analyses.

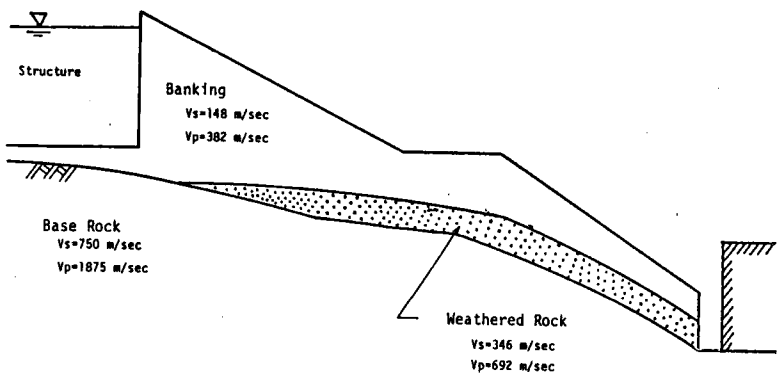

Fig. 5-1 A cross-section of the slope analyzed.

Table 5-1 Material constants and strength parameters of the slope.

	Unit weight (tf/m^3)	Shear wave velocity (m/sec)	Poisson's ratio	Cohesion (kgf/m^2)	Angle of internal friction
Banking	1.6	150	0.4	0.1	29°
Weathered rock	1.9	300	0.4	0.1	45°
Joint element	Normal spring const. 3.0×10^5 tf/m^3 Shear spring const. 3.0×10^5 tf/m^3 ①Cohesion 0.1 kgf/cm^2 Friction angle 35° ②Cohesion 0.1 kgf/cm^2 Friction angle 25°				

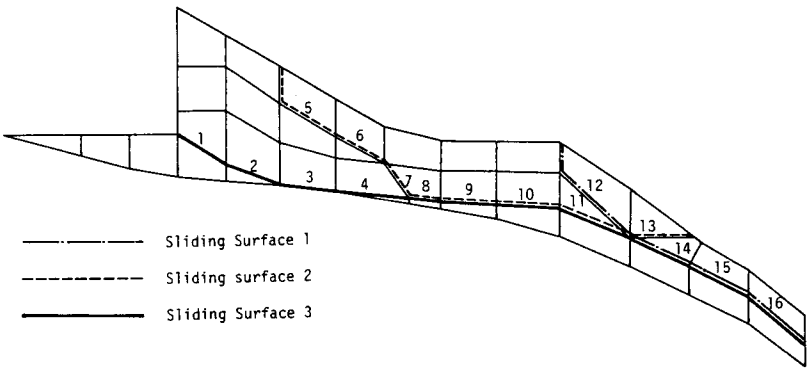

Fig. 5-2 Finite element mesh of the model and of its sliding surfaces.

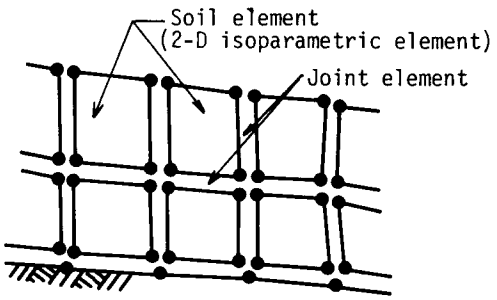

Fig. 5-3 Discretization of the slope by solid and joint elements.

The finite element mesh of the model slope is shown in Fig.5-2. Joint elements are employed at every interface between the soil elements as shown schematically in Fig. 5-3. Accordingly, each soil element is allowed to move in parallel, perpendicular and rotationally to the others, namely, they can express the sort of sliding and separation which occur in the actual situation. The solid, broken and irregular broken lines in Fig. 5-2 designate sliding surfaces for which the safety factors have been calculated. These surfaces were decided with reference to those in a previous report[13]. The numbers are the element numbers forming the sliding surface.

(2) The results of static analyses

(a) A definition of safety factor in slope stability

In order to estimate the stress state of the slope, the initial stresses due to the gravity force are first calculated and then, the stresses due to seismic force equivalent to the specified seismic coefficient are calculated under the initial stress states.

Slope stability is discussed based on the total safety factor (TSF) defined by Eq. 2-27. The safety factor indicates the safety against sliding of the entire area above the sliding surface under consideration.

Sliding first occurs locally at some point in the slope and then propagates accompanied by stress redistribution. Accordingly, the local safety factor (LSF) defined by Eq.3-27 is also used to assess the slope stability.

(b) A comparison of the results obtained by Janbu's and the finite element methods

As Fig. 5-2 shows, sliding surfaces are not circular arcs, and hence, the sliding circular method, based on the equilibrium of moment around the center of a sliding circle, cannot be applied here. Janbu's method[14] is employed to estimate the safety factor, applicable to irregularly-shaped sliding surfaces. Sliding surfaces identical in shape

and in element numbers were used to aboid differences in results due simply to differences in sliding surface shapes.

A comparison of safety factors in cases where cohesions, c=0.1 kgf/cm^2 is made in Fig. 5-4. Perfect agreement was obtained for Sliding surface 1, both monotonous and shortest. Sliding surfaces 2 and 3 which are longer and more complicated gave differences of 15 $\sim$20 % for the two methods used. One reason may be that inter-element stresses are not included in Janbu's method but are in the finite element method. An error may accumulate throughout the sliding surface and caused the differences in Fig. 5-4. In general, however, the methods are in fairly close agreement.

(c) Slope stability for static force

TSFs are obtained for three sliding surfaces by changing the cohesion of the joint element c parametrically from 0.02 to 0.1 kgf/cm^2. The results are shown in Fig. 5-5. Figure 5-5(a) shows c=0.02, (b) 0.05 and (c) 0.1 kgf/cm^2. The TSF of Sliding surface 1 is less than 1.0 at normal condition (k_H=0.0) and sliding will be caused by gravity force only when c=0.02 kgf/cm^2. When c=0.05 kgf/cm^2, Sliding surface 1 is in a critical state at normal conditions and will slide at k_H=0.1. The slope will slide if the cohesion is less than 0.05 kgf/cm^2, even when there is no seismic force. Judging from the fact that the slope remains stable, the cohesion must be a non-zero value although it was zero in laboratory tests. Therefore, 0.1 kgf/cm^2 is specified as the cohesion in the following analyses.

As the seismic coefficient increases, local sliding takes place and accompanies stress redistribution to the vicinity of the sliding surface after LSF=1.0, and when TSF=1.0 the sliding along the whole surface takes place.

Fig. 5-6 shows the TSFs and LSFs for three sliding surfaces. There is the possibility that Sliding surface 3 will slide locally even at normal conditions (Fig. 5-6(c)). However, sliding along the entire sur-

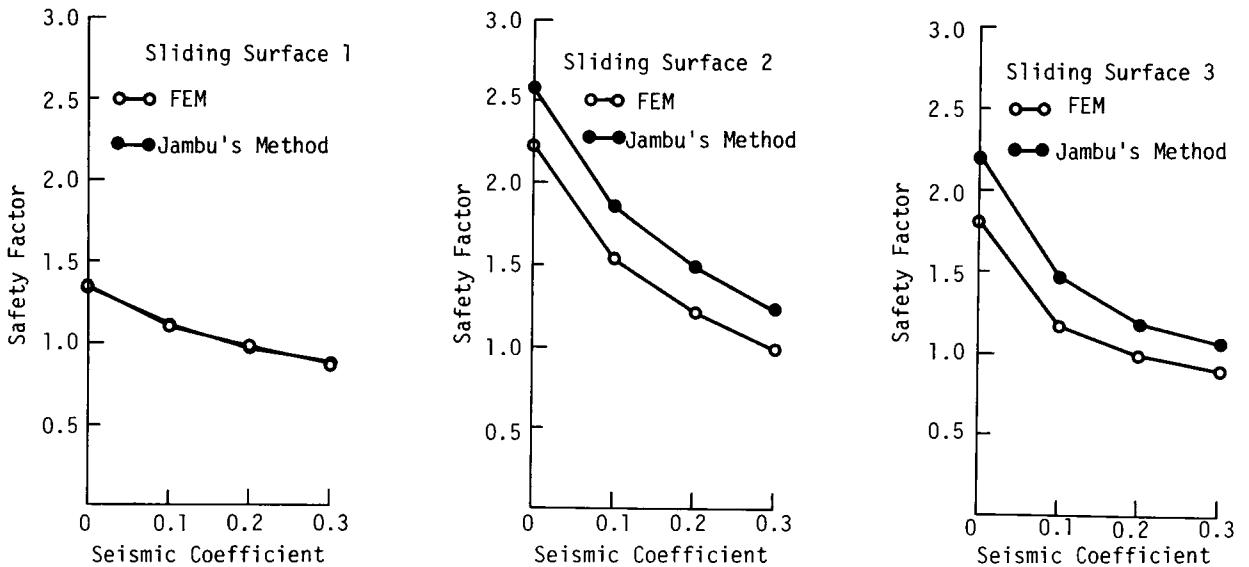

(a) Sliding surface 1 (b) Sliding surface 2 (c) Sliding surface 3

Fig. 5-4 A comparison of safety factors from the seismic coefficient and proposed methods.

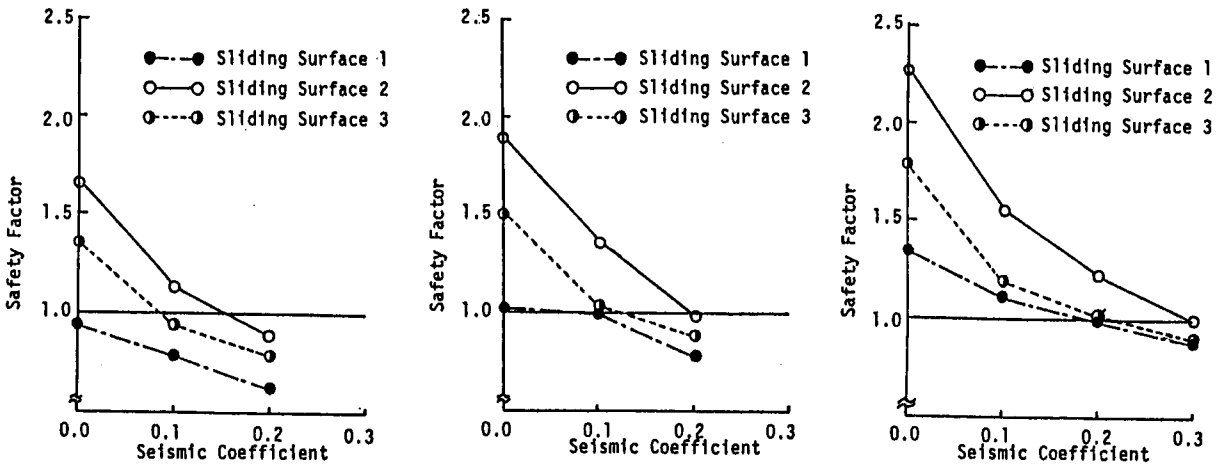

(a) C_J=0.02 kgf/cm^2 (b) C_J=0.05 kgf/cm^2 (c) C_J=0.1 kgf/cm^2

Fig. 5-5 The relationships between the TSFs of three sliding surfaces and the seismic coefficient for various levels of cohesion.

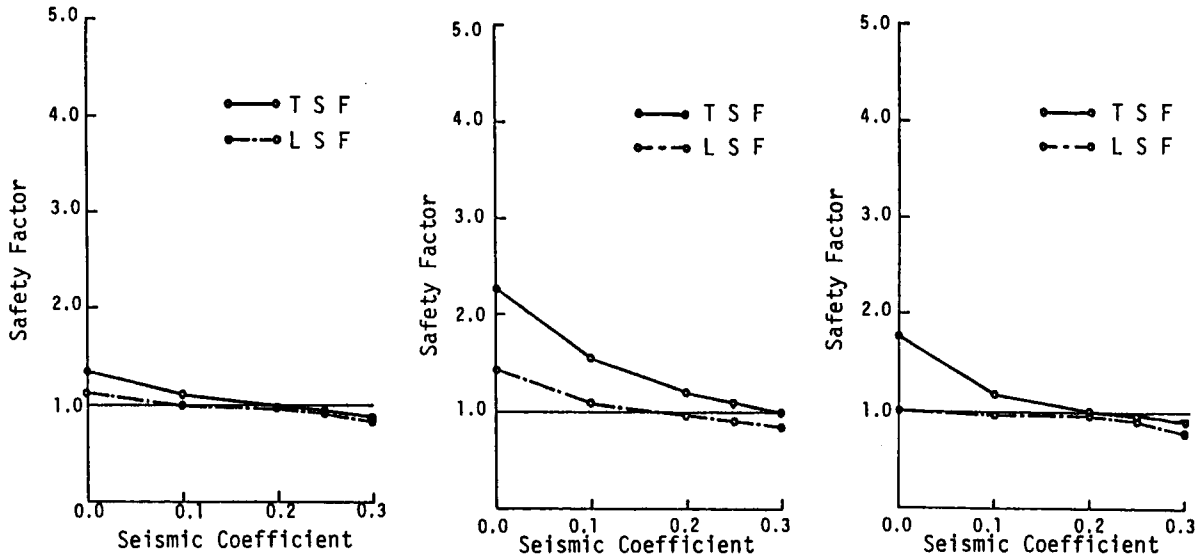

(a) Sliding surface 1 (b) Sliding surface 2 (c) Sliding surface 3

Fig. 5-6 The relationship between TSF and LSF and the seismic coefficient (C_J=0.1 kgf/cm^2).

face does not take place because there is resistance of other elements of up to k_H=0.2. As for Sliding surface 1, the zone between LSF=1.0 and TSF=1.0 is so narrow that sliding of the whole sliding surface can easily take place once there is some local sliding. Thus, Sliding surface 1 is most likely to slide, followed by surface 3 and surface 2 is the most stable.

5.3 Dynamic analyses of slope stability using the finite element method

(1) Dynamic behavior of the slope during strong earthquake motion

Prior to seismic response analyses, natural frequencies were obtained and the fundamental natural frequency was 10.16 Hz.

Figure 5-7 shows joint elements which slide and/or separate during the period of 2.0 ∿2.5 sec, or the main shock of the horizontal input acceleration, the NS component of the El Centro accelerogram. In this case (Case 1), acceleration amplitudes were not modified. In all joint elements sliding occurred along Sliding surface 1. Separation penetrated the slope from point A on the surface to point B at the base. Sliding was also observed along the interface between weathered and basal rock

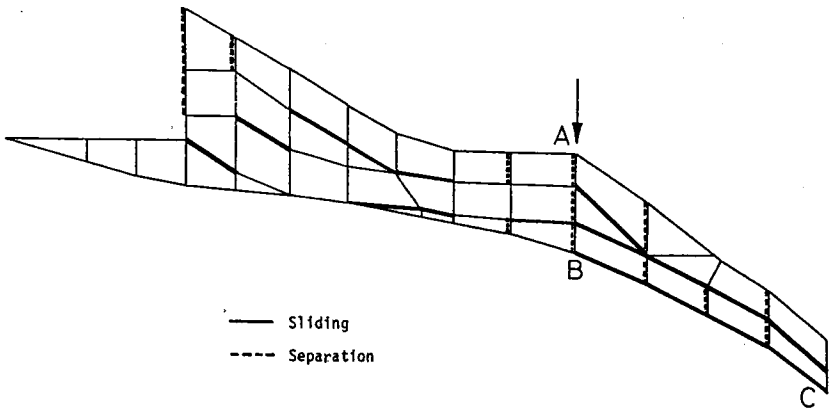

Fig. 5-7 Joint element showing sliding or separation (El Centro (1940), 340 gal, t=2.0∿2.5 sec).

(the B-C line). Furthermore, all vertical joint elements show separation in the steep right-hand region of the slope, indicating the probability of collapse here. Sliding surfaces 2 and 3 are not sliding as a whole, although their sliding appears imminent.

Figure 5-8 shows joint elements sliding and/or separating when the slope has been subjected to the El Centro accelerograms whose amplitudes are reduced to 200 gal in the NS component and 117 gal in the UD component (Case 2). Not all of the joint elements are sliding and the stability is maintained along Sliding surface 1. When compared to Case 1, the number of joint elements which are sliding or separating in Case 2 are extremely reduced. The slope as a whole remains stable if the maximum horizontal input acceleration is less than 200 gal, although local sliding takes place and the slope begins sliding and the toe area collapses if the input acceleration exceeds the 200 gal level.

The maximum response distribution for Case 1 is shown in Fig. 5-9. (a) shows horizontal acceleration, (b) horizontal velocity and (c) horizontal displacement. The response acceleration is amplified to more than 500 gal at the horizontal surface around the center of the slope. On the other hand, little amplification is observed in the right-hand region.

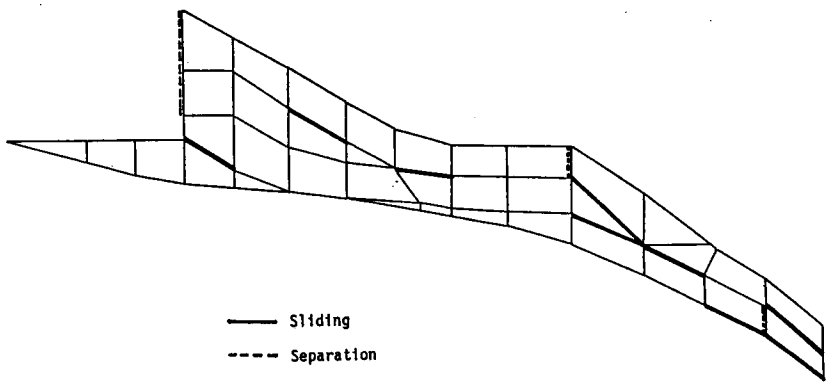

Fig. 5-8 Joint element showing sliding or separation
(El Centro (1940), 200 gal, t=2.0∿2.5 sec).

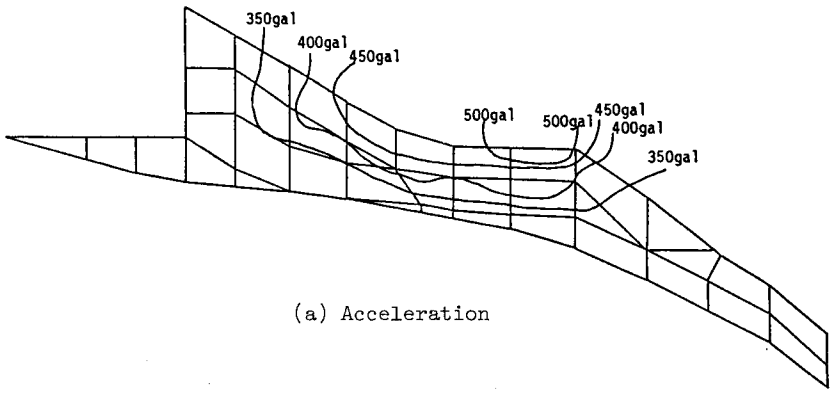

(a) Acceleration

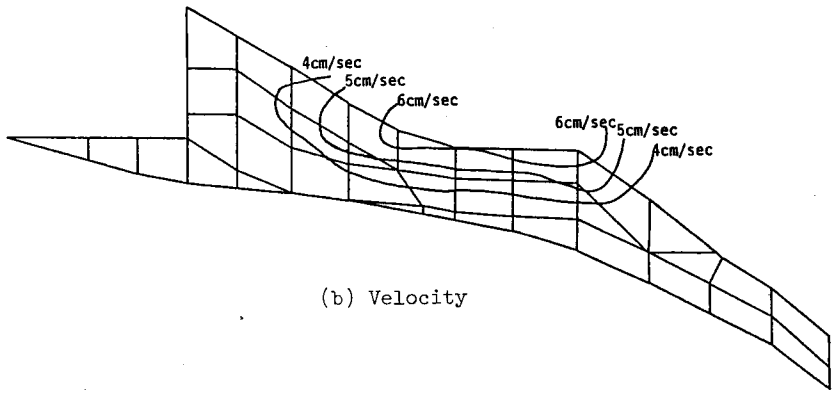

(b) Velocity

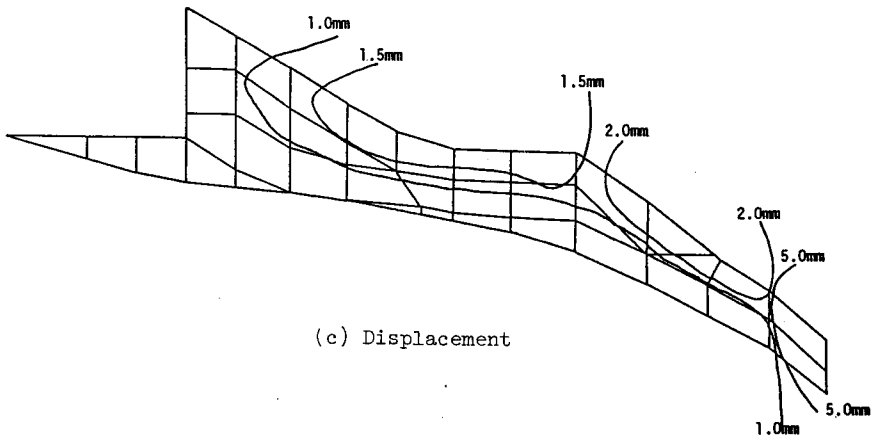

(c) Displacement

Fig. 5-9 The distribution of maximum horizontal responses (El Centro 340 gal).

The velocity distribution is almost identical to acceleration. Maximum response values appear at or close to the area where geometrical change is remarkable. Large displacement is observed in the right-hand region especially at the toe where there was only slight amplification of acceleration and velocity responses. Sliding causes this large displacement.

(2) The influence of the predominant frequency of the excitation on slope stability

The slope was subjected to the J.P.L. (Case 3) and the Hachinohe (Case 4) accelerograms in addition to the El Centro accelerograms (Cases 1 and 2). Time histories of the safety factor whose minimum value is the TSF are shown in Fig. 5-10 for Sliding surface 1. Fig. 5-10(a) is Case 1, (b) Case 2, (c) Case 3 and (d) Case 4. Sliding occurrences are denoted by the symbol ↓. It occurred five times in Case 1 and twice in Case 4. In Case 1, sliding continued for a while in the first three occurrences but was instantaneous in the last two. In Case 4, sliding took place twice and continued for a while. The sliding magnitudes at the first three events in Case 1 and at the two events in Case 4 are greater than those at the last two events in Case 1 because sliding magnitude strongly depends on the sliding duration time. It is worthwhile to note that the periods of input accelerograms on those occasions when sliding continued were relatively long. Sliding of the entire Sliding surface 1 did not take place in Cases 2 and 3 nor in any case of Sliding surfaces 2 and 3.

TSFs are summarized in Table 5-2 and they increased as the sliding surface changed, in all cases, in the order of Sliding surfaces 1, 3 and 2. This order coincides with that obtained from static analyses.

TSFs were compared for each sliding surface. Case 1 had the lowest TSF and it increases in the order of Case 4, 2 and 3 for all sliding surfaces. The lowest TSF in Case 1 in all sliding surfaces is due to its

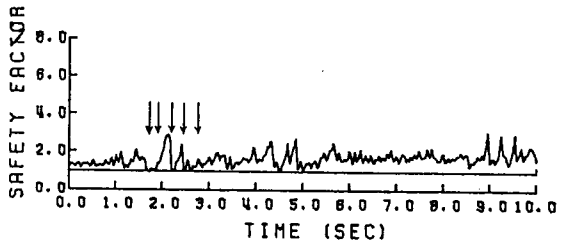

Case 1

(a) El Centro 340 gal

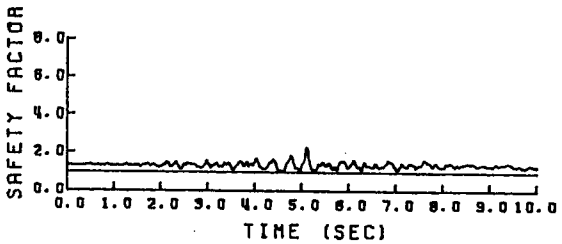

Case 3

(c) J.P.L.

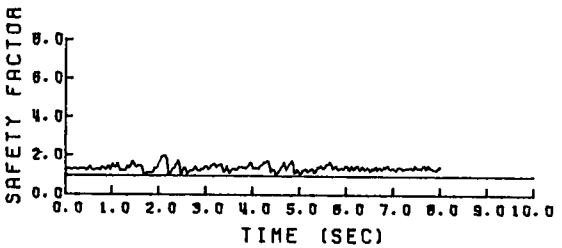

Case 2

(b) El Centro 200 gal

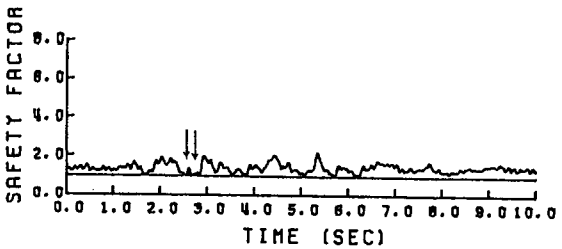

Case 4

(d) Hachinohe

Fig. 5-10 The relationships between TSF and input accelerograms (sliding surface 1).

having the largest input acceleration amplitude.

The amplitude of horizontal acceleration in Cases 2, 3 and 4 are almost the same but the predominant frequencies differ. Therefore, TSF differences are caused by the differences in the predominant frequency of input accelerograms. The largest TSF is obtained in Case 3, which has the highest predominant frequency. The lowest TSFs were obtained in Case 4 with the lowest predominant frequency. The lower the predominant frequency, the more the slope is apt to slide, and slope stability strongly depends on predominant frequency. When slope stability is in question, attention, therefore, should be paid to the frequency content as well as to the input acceleration amplitude. In the static method, the safety factor is evaluated only by the maximum acceleration, or the seismic coefficient but in dynamic analyses, the predominant frequency of the acceleration as well as its maximum value is significant.

Table 5-2 TSFs of the three sliding surfaces in the four cases.

Case	Sliding surface 1	Sliding surface 2	Sliding surface 3
Case 1	Sliding (1.0)	1.150	1.057
Case 2	1.017	1.384	1.244
Case 3	1.125	1.508	1.308
Case 4	Sliding (1.0)	1.298	1.149

(3) The effects of the material nonlinearity of soil on slope stability

The shaded areas in Figs. 5-11 and 5-12 show the elements which yielded during the time period of 2.0 ∿ 2.5 sec in Cases 1 and 2. A wide area has yielded in Case 1, but it is limited to the steep right-hand region in Case 2.

Figure 5-13 shows maximum response distribution. (a) is horizontal acceleration, (b) horizontal velocity and (c) horizontal displacement. The maximum response acceleration is about 450 gal and the area of 400 gal and over is limited to the surface surrounding the center of the

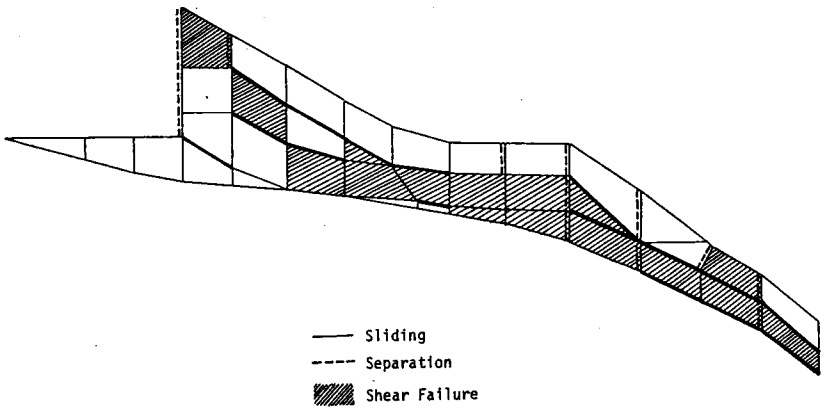

Fig. 5-11 Case 1 - Shear failure zones, and joint elements showing sliding or separation (El Centro 340 gal).

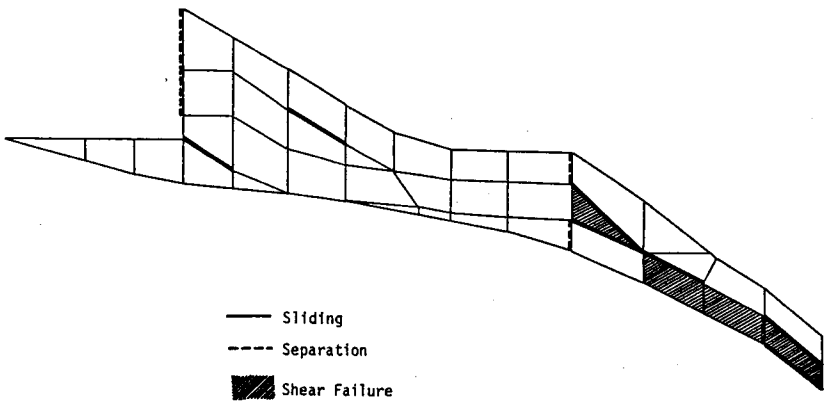

Fig. 5-12 Case 2 - Shear failure zones, and joint elements showing sliding or separation (El Centro 200 gal).

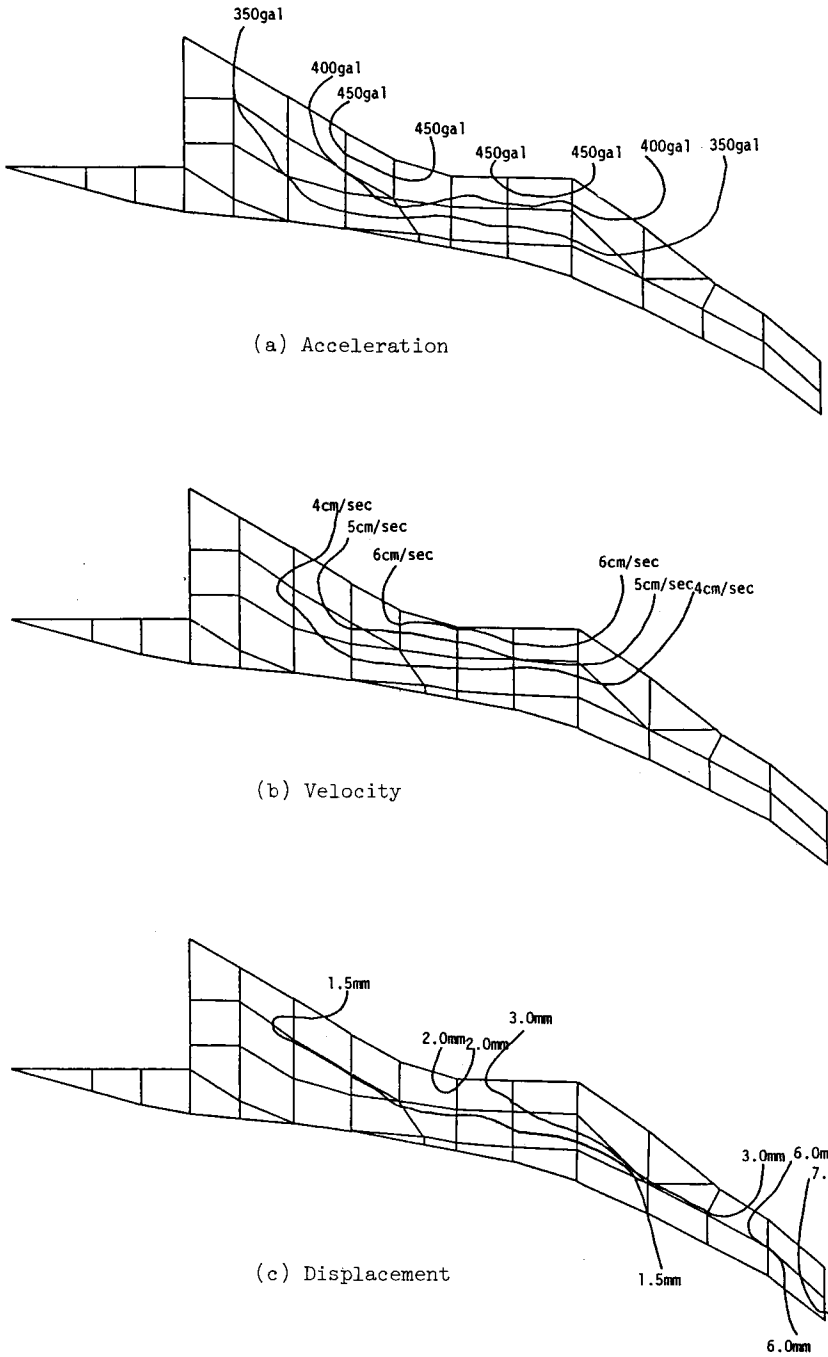

Fig. 5-13 The maximum horizontal response distribution when soil nonlinearity is taken into account (El Centro 340 gal).

slope. As the maximum value in the linear ground model was about 530 gal, soil nonlinearity reduced the maximum value by about 15 %. The similarity between the two velocity distributions, Figs. 5-9(b) and 5-13(b), indicate that soil nonlinearity does not affect response velocity. A comparison of Figs.5-9(c) and 5-13(c) indicate that displacement is about 1.5 times greater than in the case where soil is a linear elastic material.

TSFs in Case 1 are tabulated in Table 5-3. Although Sliding surface 1 slides as a whole in both types of soil. TSFs in nonlinear soil are 10 % larger for Sliding surfaces 2 and 3. This implies that a lower TSF than there actually is is estimated when soil is assumed to be a linear elastic material.

When results here are compared to static analyses, the critical seismic coefficient k_H is 0.21 (206 gal) for Sliding surface 3 (Fig. 5-6). However, it does not slide but the TSF is greater than 1.0 (Table 5-3) even when as large an amplitude as 340 gal is applied. Sliding surface 1 is stable as shown in Fig. 5-12 when the amplitude of excitation is 200 gal, although the critical seismic coefficient is 0.18 (176 gal). Again, lower TSFs than must actually exist are found by static methods, such as the seismic coefficient method.

Table 5-3 The effects of soil nonlinearity on TSF.

Case	Sliding surface 1	Sliding surface 2	Sliding surface 3
Linear Case (Case 1)	Sliding (1.0)	1.150	1.057
Non-linear Case	Sliding (1.0)	1.251	1.111

5.4 The effects of ground water on dynamic stability of the slope

(1) A procedure to estimate the pore water pressure buildup

In static and dynamic analyses of slope stability stresses were es-

timated based on the total stress and the influence of ground water was ignored, although ground water issued from the toe of the slope (see section 5.2). A complete analysis must, therefore, estimate its effect in some way.

In recent years much progress has been made in developing procedures to evaluate the pore water pressure buildup. Seismic response analyses concerned with the effects of ground water have been performed and they are classified into four categories as follows[15];

(i) total stress analyses which do not consider permeability,

(ii) total stress analyses which consider permeability,

(iii) effective stress analyses which do not consider permeability,

(iv) effective stress analyses which consider permeability.

The method proposed by Ishihara et al.[16,17] which belongs to the first type is developed and employed in this study.

(a) A model for the pore water pressure buildup

A model which assesses the pore water pressure buildup is described. The effective stress path is determined in order to assess the buildup on the basis of postulates based on previous experiments[17,18].

(i) The failure line can be approximated by a family of straight lines with sufficient accuracy, regardless of the density of sand.

(ii) The effective stress path is approximated by circular arcs in the σ_{oct}-τ_{oct} plane.

(iii) The excess pore water pressure is produced by changes in shear strain.

(iv) Constant stress ratio lines (τ_{oct}/σ_{oct}' = const.) represent yield loci. Yielding occurs and concomitantly pore water pressure increases only when the effective stress path is first traced in the direction in which the stress ratio increases. When the stress ratio decreases, the soil is assumed to behave as an elastic material and the stress path moves perpendicularly to the τ_{oct} axis, and hence, no pore water pressure is produced.

(v) When the stress ratio τ_{oct}/σ'_{oct} touches the failure line, liquefaction is initiated.

These postulates are slightly modified to the octahedral stress expression from those originally expressed for one-dimensionality by Ishihara et al.

According to the postulates, the effective stress path is as shown in Fig. 5-14. Parameter ϕ^* in the figure is the angle of internal friction in the $\sigma_{oct}-\tau_{oct}$ plane and is related to ϕ' in the two-dimensional plane by the following equation.

$$\phi^* = \frac{4\sin\phi'}{\sqrt{2}(3-\sin\phi')} \qquad (5\text{-}1)$$

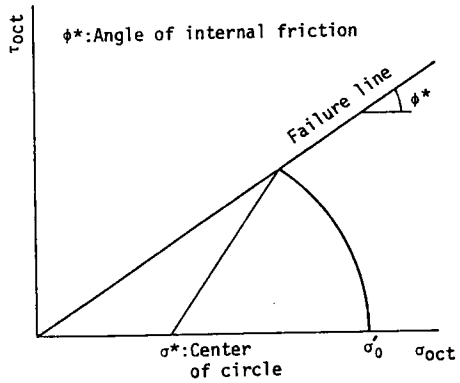

Fig. 5-14 Assumed effective stress path.

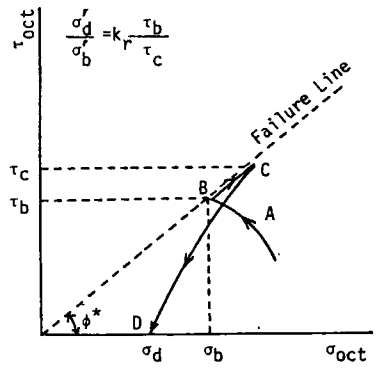

Fig. 5-15 The effective stress path after liquefaction.

When cohesion exists, the failure line moves in parallel by c^*, the two-dimensional plane cohesion, from:

$$c^* = \frac{4c' \cos\phi'}{\sqrt{2}(3-\sin\phi')} \tag{5-2}$$

where, c' is the cohesion in two-dimensional plane.

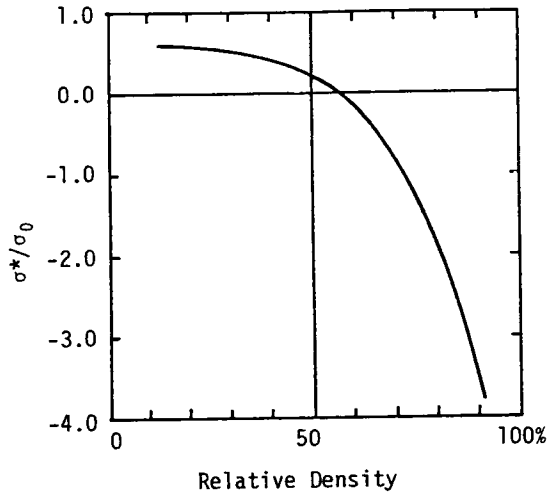

(a) The relationship between σ* and relative density.

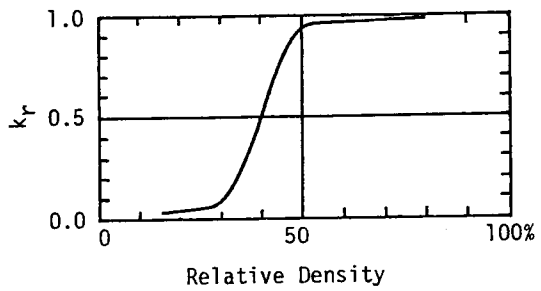

(b) The relationship between k_r and relative density.

Fig. 5-16 The relationships between pore water pressure buildup model and relative density. After Ishihara et al.[16]

The center of the effective stress path, σ^*, is a function of the relative density and is shown in Fig. 5-16(a)[16]. Fig. 5-15 shows the effective stress path after reaching the failure line, which moves along the path A-B-C-D[16]. The increment of pore water pressure at that time is $\sigma_b' - \sigma_d'$ and is assessed by[16]:

$$\frac{\sigma_{d'}}{\sigma_{b'}} = k_r \frac{\tau_{b'}}{\tau_{c'}} \tag{5-3}$$

where, k_r is a function of relative density of the soil and is shown in Fig. 5-16(b).

From the blow counts of standard penetration tests[12] at the site, $\sigma^*/\sigma_b' = 0.4$ and $k_r = 0.25$ are obtained and these values together with $C' = 0.1$ kgf/cm^2 and $\phi' = 35^\circ$ are used here.

(b) The dynamic analysis procedure

The observed water table is shown in Fig. 5-17(a) and its idealized model in Fig. 5-17(b). Where the area under the ground water table is larger than the remaining area, the elements assumed to be perfectly saturated.

The procedure is:

(i) The initial stress state due to the gravity force is calculated by making $\gamma - \gamma_w$ the unit weight of the soil beneath the ground water table, where, γ and γ_w are unit weights of soil and water respectively. The initial effective stress σ_0' for each element is then calculated from the initial stress state.

(ii) The seismic response analysis are performed under the initial stress condition obtained in the previous step and the time history of τ_{oct} is calculated for each element.

(iii) The pore water pressure buildup is assessed in each soil element by applying the pore water pressure buildup model to the time history of τ_{oct}.

(iv) Pore water pressure on the joint element U_J is, in principle,

calculated by interpolation from the pressures of neighboring soil elements. For joint elements on the boundary denoted by dotted lines and on the idealized water table below the actual one shown in Fig. 5-17, U_J is equated with the pore water pressure of the soil element with which it is in contact. U_J is, however, set at zero if the idealized water table is above the actual one.

(v) The yield shear stress of the joint element is calculated with the pore water pressure, U_J.

$$\tau_y = C_J + (\sigma_n - U_J)\tan\phi_J \tag{5-4}$$

The stability of the sliding surface is checked by substituting Eq.5-4 into Eqs.2-27 and 3-27.

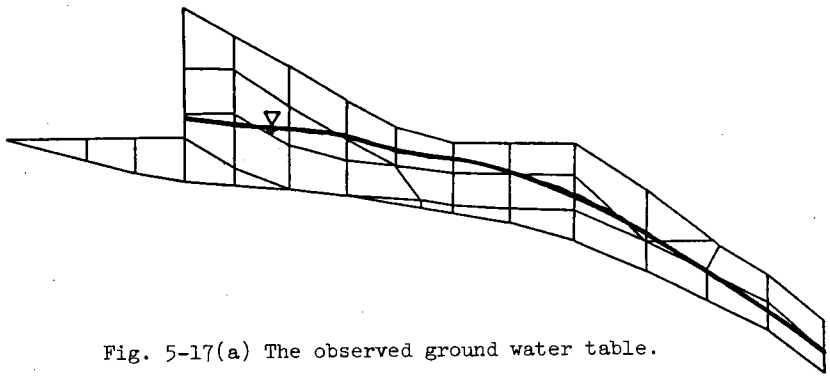

Fig. 5-17(a) The observed ground water table.

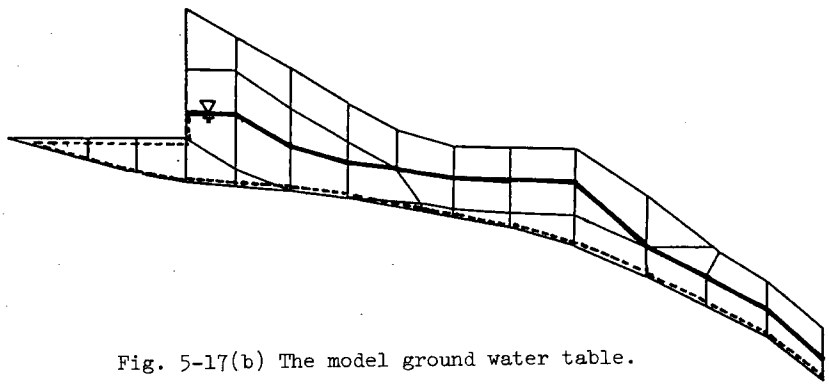

Fig. 5-17(b) The model ground water table.

(2) The influence of ground water on slope stability

Input accelerograms were the El Centro NS and UD components. The maximum amplitude of the NS component is reduced to 200 gal and 150 gal and the UD component is reduced propotionately. Two ground water tables are assumed; the one in Fig. 5-17(b) and the other which coincides with the surface of the slope, that is, the slope is fully saturated. Based on these conditions, three cases were investigated.

Case I; with a maximum horizontal input acceleration of 200 gal and the ground water table of Fig. 5-17(b).

Case II; with a maximum horizontal input acceleration of 150 gal and the ground water table of Fig. 5-17(b).

Case III; with a maximum horizontal input acceleration of 150 gal and the ground water table coincides with the slope surface.

Figure 5-18 is a time history of the pore water pressure buildup in the element illustrated in the inserted sketch. The instances of a sharp buildup in the pressure correspond to the remarkable peaks in the horizontal accelerogram and the resulting u/σ_0' ratio was 12.8 %. Figure 5-19 shows the corresponding effective stress path. The process of the pore water pressure buildup can be observed by combining the two figures. Since u/σ_0' is less than 1.0, liquefaction did not occur in the element.

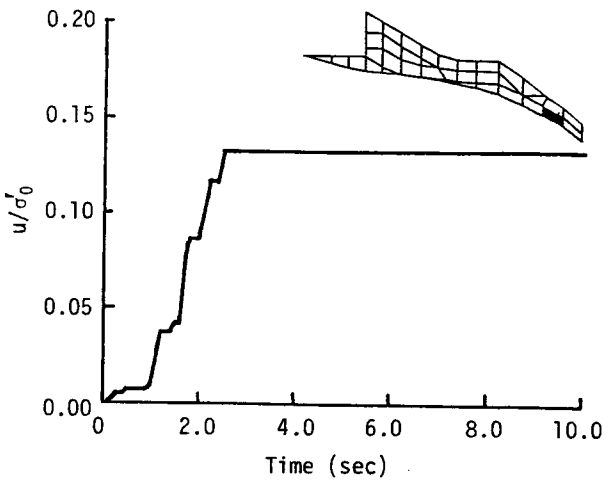

Fig. 5-18 A time history of pore water pressure normalized by initial effective stress.

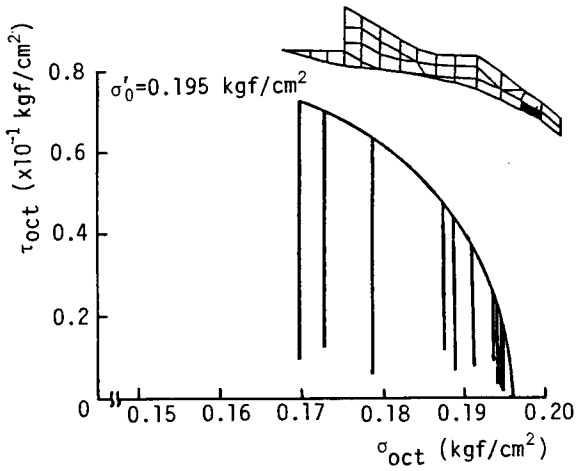

Fig. 5-19 The resultant effective stress path.

TSF obtained for each case is summarized in Table 5-4. Sliding does not take place along Sliding surface 1 in either Case I or II. TSF in Case I nearly equals to that in Case 2 in which the excitation amplitude is equal to that in Case I but ground water does not exist, since most of ground water table is below Sliding surface 1. Whole scale sliding does not take place along Sliding surface 2 for Case I or II. TSF in Case I, however, is lower than that in Case 2 due to the presence of ground water in the former.

In Sliding surface 3, sliding takes place in Case I and the TSF in Case II is 1.095 which is close to 1.0. This implies that sliding will

Table 5-4 TSF for each analytical case based on the effect of ground water.

Case	Sliding surface 1	Sliding surface 2	Sliding surface 3
Case I (200 gal)	1.002	1.179	Sliding (1.0)
Case II (150 gal)	1.066	1.331	1.095
Case III (150 gal)	Sliding (1.0)	Sliding (1.0)	Sliding (1.0)
Case 2 (200 gal)	1.017	1.384	1.244

occur along Sliding surface 3 when the excitation amplitude exceeds 150 gal provided that the ground water table is that in Fig. 5-17. TSFs are compared in Cases II and III whose excitation amplitudes are equal. Sliding does not take place in any sliding surfaces in Case II, but it does in all surfaces in Case III. The differences in water tables are the cause.

The above results suggest that every of effort should be made to keep the ground water table as low as possible in order to keep the slope stable.

5.5 Countermeasures to improve slope stability

(1) Modeling of the sheetpile

There are, at present, several measures used to improve the slope stability, such as driving a wall of piles, constructing a retaining wall and draining ground water away[19] . In this section, sheetpiles were driven into the slope as a countermeasure and slope stability is evaluated for both static and dynamic loads.

The sheetpile is modeled by the beam element[20-22]. The stiffness and mass matrices are derived in Appendix 5-I.

The element arrangement is illustrated in Fig. 5-20. Beam elements which are sandwiched between joint elements are denoted by the thick solid lines. YSP-II and YSP-III sheetpiles were used in the analysis. A cross section of the sheetpile is shown in Fig. 5-21 and the material constants per width of 1 m are given in Table 5-5[23] . The locations of sheetpile are designated in Fig. 5-22.

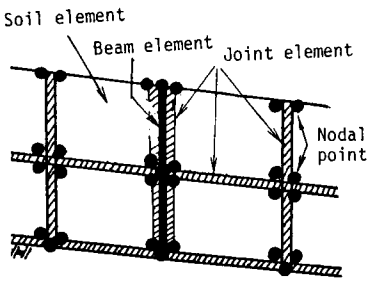

Fig. 5-20 A schematic arrangement of elements.

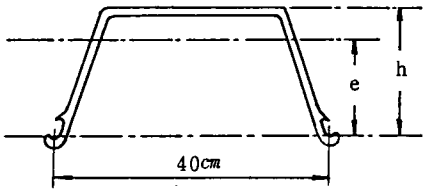

Fig. 5-21 Cross section of a sheetpile.

Table 5-5 Sheetpile constants.

	Area of section A (cm^2)	Moment of inertia of area I (cm^4)	h (cm)	e (cm)
YSP-II	153	8690	10.0	8.18
YSP-III	191	16400	12.5	9.74

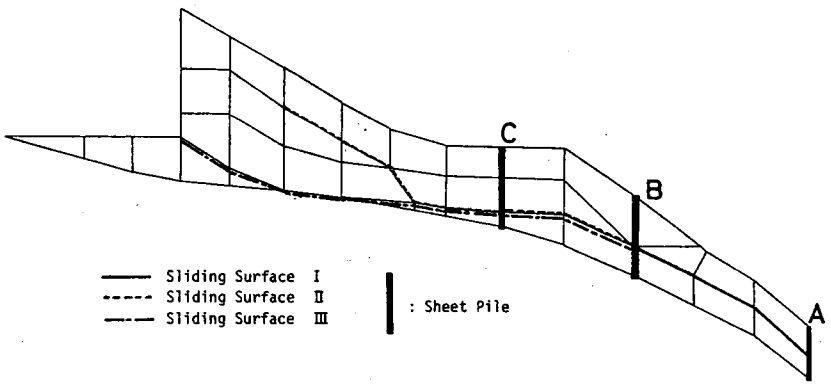

Fig. 5-22 Finite element mesh of the model with sheetpiles.

(2) Static slope stability

The bending moment and stress at the foot of the sheetpiles are calculated for static forces when the YSP-II type has been driven in at point A in Fig. 5-22 and the YSP-II or YSP-III type at point B. The obtained bending moments and stresses are shown in Fig. 5-23(a) and (b) respectively. The solid circles are the value of YSP-II sheetpile at point A and the open circles are those at point B. YSP-III stress at point B is denoted by solid triangles. The irregular broken line indicate allowable stresses of the sheetpile for seismic force, 2400 kgf/cm^2, and the regular broken line, static force, 1800 kgf/cm^2.

Figure 5-23(b) shows that the bending stress of YSP-II at point B has already exceeded the allowable stress at normal conditions (k_H=0.0). YSP-III stress at point B has reached the allowable stress at k_H=0.1. Accordingly, the stress state at point B is considered to be at the critical state in which sliding or collapse will occur.

On the other hand, YSP-II stress at point A is small, and the sheetpile is safe and stable.

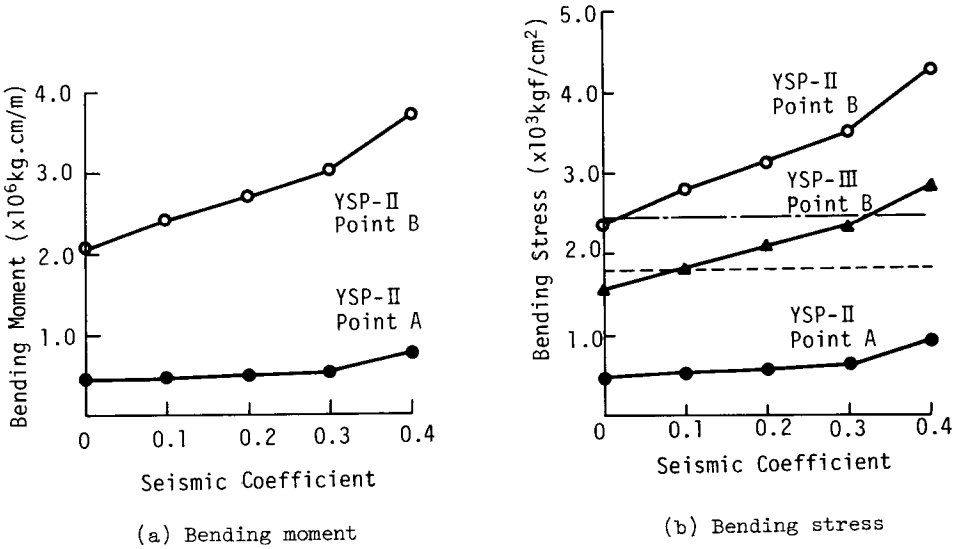

(a) Bending moment

(b) Bending stress

Fig. 5-23 The relationships between bending moments or stresses in sheetpiles and seismic coefficients.

(3) Slope stability during earthquakes

(a) The stability of the slope subjected to the reduced El Centro accelerograms

Figure 5-24 shows joint elements during sliding and/or separation. YSP-II sheetpiles were driven in at points A and B in a slope that has been subjected to the reduced accelerograms (200 gal NS, 117 gal UD). In comparison with the slope in Fig. 5-8 which had no sheetpiles, here the number of joint elements which slide or separate is greatly reduced.

Table 5-6 compares the maximum bending moments and stresses obtained from the seismic coefficient method (k_H=0.2) and from seismic response analyses. For a sheetpile at point B, static stress is greater than the yield stress level, 3000 kgf/cm^2, while dynamic stress is just at the allowable stress level. Furthermore, this 2463 kgf/cm^2 value is instantaneous, and hence, the sheetpile is considered to be safe.

It can be said that the slope will remain stable if sheetpiles are driven in at points A and B if the seismic excitation whose amplitude is 200 gal or less, while the static analysis showed that the slope would not remain stable for a seismic coefficient of 0.2 since the stress exceeded the yield stress level.

(b) The stability of the slope subjected to the original El Centro accelerograms

Judging from the above result, it is easily expected that the sheetpile at point B will yield when the slope is subjected to the original El Centro accelerograms whose maximum horizontal acceleration is 340 gal. Accordingly, additional YSP-II sheetpile has been driven into the slope at point C to reduce the seismic load upon the one at point B.

The bending stresses of sheetpiles at points B and C were 3590 kgf/cm^2 and 2750 kgf/cm^2 respectively. Both sheetpiles exceed the allowable stress level and thus, stiffer and stronger ones are required

Table 5-6 The comparison of the bending moments and stresses obtained from dynamic and static analyses.

	Bending moment YSP-II		Bending stress YSP-II	
	Point A (kgf.cm/m)	Point B (kgf.cm/m)	Point A (kgf/cm^2)	Point B (kgf/cm^2)
Static	4.90×10^5	2.71×10^6	563.9	3120
Dynamic El Centro (200 gal)	4.46×10^5	2.14×10^6	512.7	2463

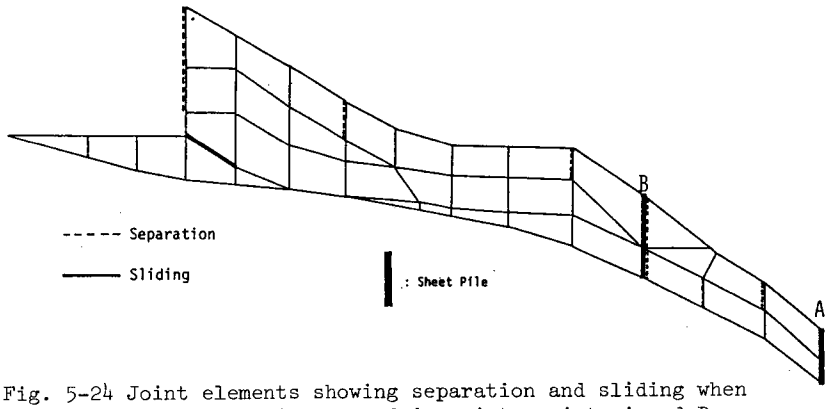

Fig. 5-24 Joint elements showing separation and sliding when YSP-II sheetpiles are driven into points A and B.

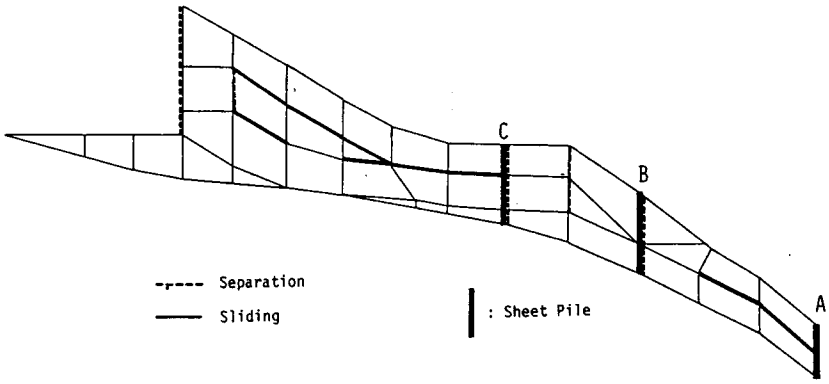

Fig. 5-25 Joint elements showing separation and sliding when three sheetpiles are driven into points A, B and C.

at both points, so YSP-III sheetpiles are driven in at points B and C in place of the YSP-II type.

Figure 5-25 shows joint elements which slid or separated between 2.0 and 2.5 sec as in Fig.5-8. A comparison of the two figures shows that those joint elements disappear, especially in deep areas which have sheetpiles driven into them, a phenomenon actually observed in the experiments[24].

The maximum stresses are 419 kgf/cm^2, 2683 kgf/cm^2 and 1906 kgf/cm^2 for the respective sheetpiles at points A, B and C. Although the stress of sheetpile at point B exceeds the allowable level by 10 %, this stress is instantaneous. Furthermore, the remaining two sheetpiles stay sufficiently below allowable stress. Judging from these results, it can be concluded that the slope will keep its stability in this case, even if it has been subjected to the original El Centro accelerograms.

5.6 Conclusions

The stability of the present slope was quantitatively assessed for static and dynamic forces. From the analyses presented, the followings can be concluded:

(1) When safety against sliding was compared for Janbu's and the finite element methods, fairly good agreement was obtained, though in general the latter resulted in lower safety factors.

(2) Material nonlinearity of soil decreased response acceleration by 15 % and increased displacement. Higher safety factors of 5 ∿8 % were obtained when compared to the factors found when the slope was assumed to be linear elastic material.

(3) Although the critacal seismic coefficient is 0.21 (206 gal) for the entire slope sliding (Sliding surface 3), it does not slide even when as large an amplitude as 340 gal is applied. For the local collapse (Sliding surface 1), it is stable when the excitation amplitude is 200 gal, although the critical seismic coefficient is 0.18 (176 gal).

(4) Safety factors strongly depends on the predominant frequency as well as the amplitude of the horizontal input accelerogram. The lower the predominant frequency, the lower the safety factor.

(5) Ground water significantly decreases slope stability, so, the drainage of ground water is a indispensable countermeasure to maintain the slope stable.

(6) Bending stresses of sheetpiles driven into the slope were 10 ∿ 20 % larger for the seismic coefficient method than dynamic analyses.

(7) Slope failure was reduced by driving in sheetpiles. Sliding in the deep areas disappeared and was seen only near the surface.

(8) The slope remained stable if YSP-II sheetpiles at the toe and at the top of the steep right-hand region of the slope during reduced El Centro accelerograms of 200 gal horizontal acceleration.

For the original El Centro accelerograms, YSP-II sheetpiles were replaced with YSP-III sheetpile at the top of the steep right-hand region and an additional YSP-III sheetpile was added to the middle part of the slope as this was necessary to remain stable.

Although analytical examples have presented many useful information, there are still important problems to be solved or investigated. First, the model of the pore water pressure buildup is only an approximate one and there was no feedback of built-up pore water pressure effects on the dynamic behavior of the soil. Moreover, neither the permeability of ground water nor changes in the ground water table during excitation were studied or accounted for. The behavior of ground water is supposed to be extremely complex when there is partial sliding and/or separation. Therefore, effort is needed to overcome these difficulties in order to investigate slope stability more accurately.

Although the cross section of the sheetpile was increased in area to obtain greater stability by objectively prescribing places most suitable for sheetpiles, research is needed to determine the optimum

points for sheetpiles.

Finally, safety factors were calculated along prescribed sliding surfaces. However, the most critical area changes every second, so that, safety factors must be estimated along sliding surfaces which vary over time in order to learn the weakest line against sliding.

Chapter 5 references

1) Akutagawa S., R. Yoshinaka and T. Yasue: The relationship between the seismic disaster and topographic and geologic features. 4. Examples in mountaneous regions, Tsuchi-to-kiso , JSSMFE, Vol.28, No.6, pp.95-102, 1980, (in Japanese).

2) Hanmachi Y.: Slope failures due to earthquakes, Doboku-gijutsu-shiryo, Vol.20, No.12, pp.30-35, 1978, (in Japanese).

3) General report on the 1968 Tokachi-oki earthquake, Investigation Committee of the 1968 Tokachi-oki earthquake, 1968, (in Japanese).

4) Osawa Y. and K. Tsumura: General report on the disasters by the 1978 Izuoshima-kinkai earthquake, 15th symposium on the natural disaster science, pp.17-20, 1978, (in Japanese).

5) General report on the 1978 Miyagiken-oki earthquake, Investigation committee of the 1978 Miyagiken-oki earthquake at Tohoku Branch of JSCE, 1980, (in Japanese).

6) 1974 Izuhanto-oki earthquake, 11th symposium on the natural disaster science, pp.144-169, 1974, (in Japanese).

7) Iwasaki T., K. Kawashima and I. Moritani: Seismic response characteristics of a slope, 35th Proc. of annual meeting of JSCE, pp.584-585, 1980, (in Japanese).

8) Ishida T., H. Watanabe, H. Ito, Y. Kitahara and M. Matsumoto: Numerical analysis on dynamic mechanism of slope failure, Central Research Institute of Electric Power Industry, Report No.381003, 1981, (in Japanese).

9) Watanabe H. and K. Baba: A study on the sliding stability analysis of the fill dam based on the dynamic analysis, Large Dam, No.97, pp.1-4, 1981, (in Japanese).

10) Toki K., Y. Iwasaki, M. Tai and H. Kishimoto: Slope stability analysis during strong earthquake motion by the joint element, Report of 16th meeting of earthquake engineering, pp.109-112, 1981, (in

Japanese).

11) Chowdhury R. N.: Slope analysis, Elsevier Scientific Publishing Company, Ch.1, 1978.

12) Research works on the aseismic countermeasure of the purification plant -No.1-, Department of waterworks of Kyoto city and Osaka soil test laboratory, 1980, (in Japanese).

13) Research works on the aseismic countermeasure of the purification plant -No.2-, Department of waterworks of Kyoto city and Osaka soil test laboratory, 1981, (in Japanese).

14) Chowdhury R. N.: Slope analysis, Elsevier Scientific Publishing Company, pp.143-154, 1978.

15) Ishihara K.: Analysis method of ground motion considering the lique-faction, Tsuchi-to-kiso, Vol.29, No.11, pp.85-91, 1981, (in Japanese).

16) Ishihara K., J. Lysmer, S. Yasuda and H. Hirao: Prediction of liquefaction in sand deposits during earthquakes, Soils and Foundations, Vol.16, No.1, pp.1-16, 1976.

17) Ishihara K., F. Tatsuoka and S. Yasuda: Undrained deformation and liquefaction of sand under cyclic stresses, Soils and Foundations, Vol.15, No.1, pp.29-44, 1975.

18) Ishihara K. and S. Yasuda: Sand liquefaction in hollow cylinder torsion under irregular excitation, Soils and Foundations, Vol.15, No.1, pp.45-59, 1975.

19) Matsui T.: Slope stability analysis considering the effect of the pile wall, Text of 'The examples of the stability analysis of soil structures', Kansai Branch of JSCE, 1980, (in Japanese).

20) Yamada Y.: Material mechanics by matrix algorithm, The chair of the structural engineering by the computer code, No. I-3-A, Baifukan, pp.148-160, 1970, (in Japanese).

21) Zienkiewicz O. C.: The finite element method in engineering science, 3rd Ed., Mc Graw Hill, London, Ch.2, pp.37-39, 1972.

22) Toki K.: Aseismic analysis for civil engineering structures, JSCE, Gihodo, p.133, 1981, (in Japanese).

23) Handbook of civil engineering, JSCE, Gihodo, p.1812, 1964, (in Japanese).

24) Ishida T., H. Watanabe, H. Ito, Y. Kitahara and M. Matsumoto: Numerical analysis on static mechanism of slope failure in model test, Central Research Institute of Electric Power Industry, Report No.380057, 1981, (in Japanese).

Appendix 5-I

Derivation of stiffness and mass matrices of the beam element

The beam element and its local co-ordinate system are shown in Fig. 5-A-1. The deflection , w, and displacement , δ, parallel with the axis at point x are related to the nodal displacement vector $\{d_k\}$ with a shape function matrix $[N]$

$$\begin{Bmatrix} \delta \\ w \end{Bmatrix} = [N]\{d_k\} \tag{5-A-1}$$

where,

$$\{d_k\} = \{u_i \;\; v_i \;\; \theta_i \;\; u_j \;\; v_j \;\; \theta_j\}^T \tag{5-A-2}$$

$$[N] = \begin{bmatrix} 1-\frac{x}{\ell} & 0 & 0 & \frac{x}{\ell} & 0 & 0 \\ 0 & 1-3(\frac{x}{\ell})^2+2(\frac{x}{\ell})^3 & x-\frac{2}{\ell}x^2+\frac{x^3}{\ell^2} & 0 & 3(\frac{x}{\ell})^2-2(\frac{x}{\ell})^3 & -\frac{x^2}{\ell}+\frac{x^3}{\ell^2} \end{bmatrix} \tag{5-A-3}$$

u_k, v_k and θ_k $(k = i, j)$ are nodal displacements in directions x and y and the rotational angle at nodal point k. ℓ is the length of the beam element.

The generalized 'strain' here is the curvature, κ, and corresponding generalized 'stress' is the bending moment, M. Thus,

$$\kappa = -\frac{d^2w}{dx^2} \qquad M = -EI\frac{d^2w}{dx^2} = EI\kappa \tag{5-A-4}$$

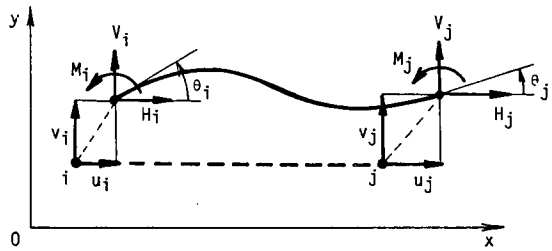

Fig. 5-A-1 Nodal forces and displacements of the beam element.

where, EI is flexural rigidity.

In the axial direction, axial strain, ε, and stress, σ, are

$$\varepsilon = \frac{d\delta}{dx}$$
$$\sigma = E\varepsilon \tag{5-A-5}$$

The relationship between the strain vector $\{\varepsilon\}=\{\kappa\ \varepsilon\}^T$ and the nodal displacement vector $\{d_k\}$ are expressed as follows, stipulating that $\theta = dw/dx$.

$$\{\varepsilon\} = [B]\{d_k\} \tag{5-A-6}$$

where,

$$[B] = \begin{bmatrix} -\frac{1}{\ell} & 0 & 0 & \frac{1}{\ell} & 0 & 0 \\ 0 & \frac{6}{\ell^2}-\frac{12}{\ell^3}x & \frac{4}{\ell}-\frac{6}{\ell^2}x & 0 & -\frac{6}{\ell^2}+\frac{12}{\ell^3}x & \frac{2}{\ell}-\frac{6}{\ell^2}x \end{bmatrix} \tag{5-A-7}$$

The stiffness $[k]^e$ and mass matrices $[m]^e$ are:

$$[k]^e = \int_0^\ell [B]^T[D][B]\,dx$$
$$[m]^e = A\int_0^\ell [N]^T\rho[N]\,dx \tag{5-A-8}$$

where,

$$[D] = \begin{bmatrix} EA & 0 \\ 0 & EI \end{bmatrix} \tag{5-A-9}$$

That is,

$$[k]^e = \begin{bmatrix} EA/\ell & 0 & 0 & -EA/\ell & 0 & 0 \\ & 12EI/\ell^3 & 6EI/\ell^2 & 0 & -12EI/\ell^3 & 6EI/\ell^2 \\ & & 4EI/\ell & 0 & -6EI/\ell^2 & 2EI/\ell \\ & & & EA/\ell & 0 & 0 \\ & & & & 12EI/\ell^3 & -6EI/\ell^3 \\ & \text{Symmetric} & & & & 4EI/\ell \end{bmatrix} \tag{5-A-10}$$

$$[m]^e = \frac{\rho\ell}{420}\begin{bmatrix} 140 & 0 & 0 & 70 & 0 & 0 \\ & 156 & 22\ell & 0 & 54 & -13\ell \\ & & 4\ell^2 & 0 & 13\ell & -3\ell^2 \\ & & & 140 & 0 & 0 \\ & \text{Symmetric} & & & 156 & -22\ell \\ & & & & & 4\ell^2 \end{bmatrix} \tag{5-A-11}$$

Since these matrices are derived for the local coordinate system, they must be translated into the global coordinate system in the same manner as was the joint element.

6. Soil-Structure-Water Systems

6.1 General remarks

With increasing industrial development in recent decades, important and large-scale structures have been constructed on coastal areas or reclaimed areas, and there have been numerous projects to recover land from the sea or to construct airports or power plants. Reclamation and the principles underlying it are extremely important and as a results, revetment structures are built on a larger scale than ever before.

Revetment structures are subjected to hydrodynamic pressure as well as inertia force during earthquakes and the former may affect the dynamic stability of the structure. Hydrodynamic pressure acting on walls was first examined by Westergaard[1] and the approximate equation is still used in design. Zienkiewicz et al.[2] used the finite element method to analyze the pressure acting on dams during earthquakes and found that it was of sufficient accuracy. Chopra et al.[3] applied the substructure method to dynamic response analyses of water-structure interaction systems.

On the other hand, some research works have been performed to investigate the dynamic behavior of quaywall-subsoil interaction systems neglecting the influence of hydrodynamic pressure[4,5]. There are, in fact, very few works on the dynamic characteristics or dynamic stability of revetment structures considering effects of both hydrodynamic pressure and surrounding soil.

This chapter concerned with dynamic analyses of water-soil revetment structure interaction systems. Using the finite element method,

linear and nonlinear dynamic response analyses have been performed to investigate the effect of hydrodynamic pressure on responses of the structure.

6.2 The equation of motion for soil-structure-water interaction systems

(1) Hydrodynamic aspects

From the Navier-Stokes equation and the equation of continuity, neglecting the viscous and convective acceleration terms, hydrodynamic pressure, p, is governed by the wave equation:

$$\nabla^2 p = \frac{1}{C^2}\ddot{p} \tag{6-1}$$

where, ∇^2 is the Laplacian operator in two dimension, C is the velocity of sound in water and dots represent differentiation with respect to time. Employing the Galerkin method, Eq. 6-1 can be discretized to give a matrix equation of the form:

$$[Q]\{\ddot{p}\} + [H]\{p\} = \{B\} \tag{6-2}$$

where,

$$\left.\begin{aligned} Q_{kl} &= \Sigma q_{kl} \\ H_{kl} &= \Sigma h_{kl} \\ B_k &= \Sigma b_k \end{aligned}\right\} \tag{6-3}$$

and

$$\left.\begin{aligned} h_{ij} &= \int_v \left(\frac{\partial N_i}{\partial x}\frac{\partial N_j}{\partial x} + \frac{\partial N_i}{\partial y}\frac{\partial N_j}{\partial y}\right) dv \\ q_{ij} &= \frac{1}{C^2}\int_v N_i N_j \, dv \\ b_i &= \int_s N_i \frac{\partial p}{\partial n} \, ds \end{aligned}\right\} \tag{6-4}$$

where, N_i defines the appropriate shape function, V and S, the region and the external boundary of an element and n, the direction normal to the boundary. The summation is carried out over all the elements corre-

sponding to the degree-of-freedom. The eight-nodal-point isoparametric element[6] is employed to model the water system in this study (see Appendix 6-I).

Since the extent of the water system is large, it is necessary to truncate the system at a sufficiently large distance from the structure. At this boundary, a suitable radiation condition is imposed ensuring that no waves are reflected, such as the radiation boundary condition method[7] or the infinite element method[8] of which the latter was found to be preferable by Zienkiewicz et al. who investigated in detail.

Accordingly, the latter was adopted at the artificially truncated boundary. The infinite element extends to infinity in one direction (x-direction) and is finite in the other direction (y-direction) (see Appendix 6-II).

The equation of motion, Eq. 6-1 is solved under the following boundary conditions that on the boundary where the normal motion is prescribed:

$$\frac{\partial p}{\partial n} = -\rho_w \alpha_n \tag{6-5}$$

where, ρ_w is the mass density of water, and α_n the absolute acceleration in the normal direction at the point under consideration.

On the free surface, assuming the absence of surface wave,

$$p = 0 \tag{6-6}$$

(2) Coupling of structural and hydrodynamic aspects

The equation of motion of a soil-structure interaction system is:

$$[M]\{\ddot{\delta}\} + [C]\{\dot{\delta}\} + [K]\{\delta\} = \{f\} \tag{6-7}$$

where, $[M]$, $[C]$ and $[K]$ are mass, damping and stiffness matrices and $\{\delta\}$ and $\{f\}$ are the nodal displacement and force vectors of the system. When the dynamic interaction with water is considered, the external force vector, $\{f\}$, in Eq. 6-7 is the summation of inertia force, $\{F\}$, and the

force due to hydrodynamic pressure, $\{P\}$. Namely,

$$\{f\} = \{F\} + \{P\} \tag{6-8}$$

where, element i of vector $\{P\}$ is:

$$P_i = \int_s N_i' \Sigma N_j p_j \, ds \tag{6-9}$$

where, p_i is hydrodynamic pressure on the nodal point i and N_i' the appropriate shape function which converts hydrodynamic pressure into nodal force vectors depending on the direction of the normal relative to the global coordinates. In matrix form, Eq. 6-9 can be written as

$$\{P\} = [L]\{p\} \tag{6-10}$$

On the other hand, the excitation vector, $\{B\}$ of Eq. 6-2, equivalent to the boundary condition (6-5), can be written as

$$\{B\} = -\rho_w [L]^T (\{a_g\} + \{\ddot{\delta}\}) \tag{6-11}$$

where, vector $\{a_g\} + \{\ddot{\delta}\}$ represents the absolute acceleration of the interface due to ground motion $\{a_g\}$ and the superscript, T, indicates that the matrix is transposed.

Substituting Eq. 6-10 into Eq. 6-7 and with inertia force $\{F\} = -[M]\{a_g\}$, the equation of motion of the soil-structure interaction system can be written as:

$$[M]\{\ddot{\delta}\} + [C]\{\dot{\delta}\} + [K]\{\delta\} = -[M]\{a_g\} + [L]\{p\} \tag{6-12}$$

Substituting Eq. 6-11 into Eq. 6-2, that for water can be written as:

$$[Q]\{\ddot{p}\} + [H]\{p\} = -\rho_w [L]^T (\{a_g\} + \{\ddot{\delta}\}) \tag{6-13}$$

Let the steady-state of the ground motion be:

$$\{a_g\} = \{a_{g0}\} e^{i\omega t} \tag{6-14a}$$

here, ω is the circular frequency and $\{a_{g0}\}$ is the amplitude of ground

acceleration. The steady-state responses of the system will be given by

$$\{\delta\} = \{\delta_0\}e^{i\omega t} \tag{6-14b}$$

$$\{p\} = \{p_0\}e^{i\omega t} \tag{6-14c}$$

where, $\{\delta_0\}$ and $\{p_0\}$ are the amplitudes of nodal displacement and hydrodynamic pressure,

Substituting Eqs. 6-14 into Eqs. 6-12 and 6-13, the following equations are obtained:

$$([K] + i\omega[C] - \omega^2[M])\{\delta_0\} = -[M]\{a_{g0}\} + [L]\{p_0\} \tag{6-15}$$

$$([H] - \omega^2[Q])\{p_0\} = -\rho_w[L]^T(\{a_{g0}\} - \omega^2\{\delta_0\}) \tag{6-16}$$

From Eq. 6-16, hydrodynamic pressure vector $\{p_0\}$ is:

$$\{p_0\} = -([H] - \omega^2[Q])^{-1}\rho_w[L]^T(\{a_{g0}\} - \omega^2\{\delta_0\}) \tag{6-17}$$

Substituting Eq. 6-17 into 6-15, the equation of motion governing the soil structure interaction system can be derived:

$$([K] + i\omega[C] - \omega^2[M^*])\{\delta_0\} = -[M^*]\{a_{g0}\} \tag{6-18}$$

where,

$$[M^*] = [M] + \rho_w[L]([H] - \omega^2[Q])^{-1}[L]^T \tag{6-19}$$

here, the second term of Eq. 6-19 implies virtual mass.

Solving Eqs. 6-18 and 6-19, the response, $\{\delta_0\}$, of a soil-structure system with the effects of hydrodynamic pressure, $\{p_0\}$, can be determined for a prescribed circular frequency, ω.

6.3 Dynamic characteristics of soil-structure-water interaction systems

(1) The model analyzed

Figure 6-1(a) shows the water-soil-revetment structure system which

is analyzed and Fig. 6-1(b) the finite element mesh of the system which is called Model 1. The model without water is called Model 2. The soil and the structure are both assumed to be linear elastic materials and perfect bonding at the contact surface between the soil and structure is postulated in this section. Constants of the model are listed in Table 6-1.

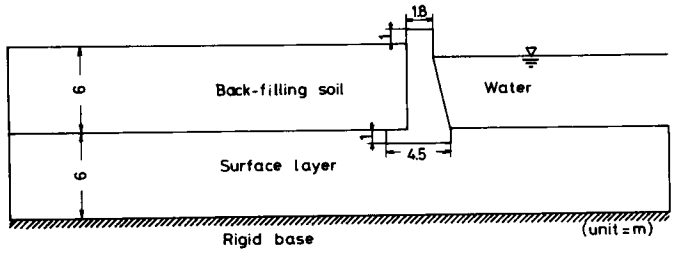

Fig. 6-1(a) Model 1 - A general view of the water-soil-structure system.

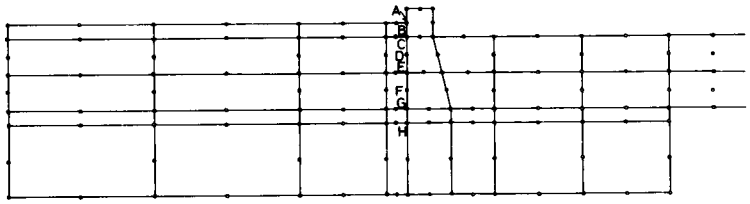

Fig. 6-1(b) Finite element mesh of Model 1.

Table 6-1 Physical properties of the model.

	Unit weight (tf/m^3)	Shear wave velocity (m/sec)	Poisson's ratio	Damping factor
Structure	γ_1=2.35	C_1=1600	ν_1=0.17	h_1=0.05
Back-filling soil	γ_2=1.70	C_2=120	ν_2=0.40	h_2=0.05
Surface layer	γ_3=1.80	C_3=160	ν_3=0.40	h_3=0.05
Water	γ_4=1.00	Velocity of sound in water 1440 (m/sec)		

Prior to the dynamic response analysis, natural frequencies and normal modes were obtained. The results are shown in Table 6-2 and Fig. 6-2. From Fig. 6-2, shear deformation is predominant in the fundamental mode and vertical deformation of back-filling is predominant in the second mode.

Table 6-2 Natural frequencies of Model 2.

Mode	Natural frequency (Hz)
1	3.37
2	5.07
3	6.60
4	6.99
5	7.75

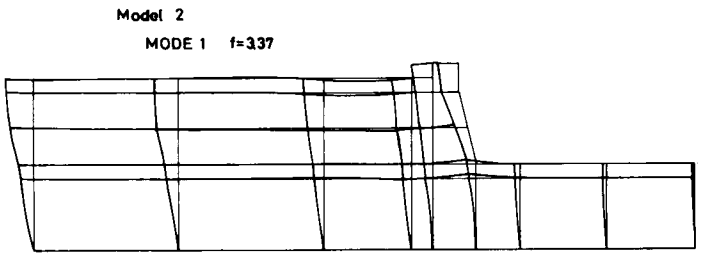

(a) The fundamental mode

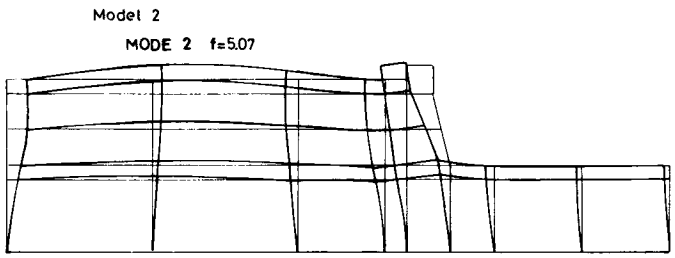

(b) The second mode

Fig. 6-2 Mode shapes of Model 2.

(2) Hydrodynamic responses

(a) The distribution of hydrodynamic pressure along the boundary

The distribution of hydrodynamic pressure produced on the wall, perpendicular to the direction of motion, is given by Westergaard's equation. Hydrodynamic pressure along the inclined wall was investigated by Zangar et al.[9] . Although the equations are valid for low frequency ranges, they may give estimate hydrodynamic pressure which are too low in the area of the resonant frequency of the structure because they assume that the wall is rigid and moves to the same degree as does the ground.

Figure 6-3 shows the distribution of hydro- dynamic pressure along the revetment structure's surface and the bottom of the water at 0.29 Hz by the finite element method, a frequency far lower than the 3.37 Hz resonant frequency of the system. The distributions from Westergaard's and Zangar's equations are also shown. Since hydrodynamic pressure decreases as the wall inclines, Westergaard's equation gives the largest value. The finite element method agree well with Zangar's equation for a 15° inclination, or that of the structural face.

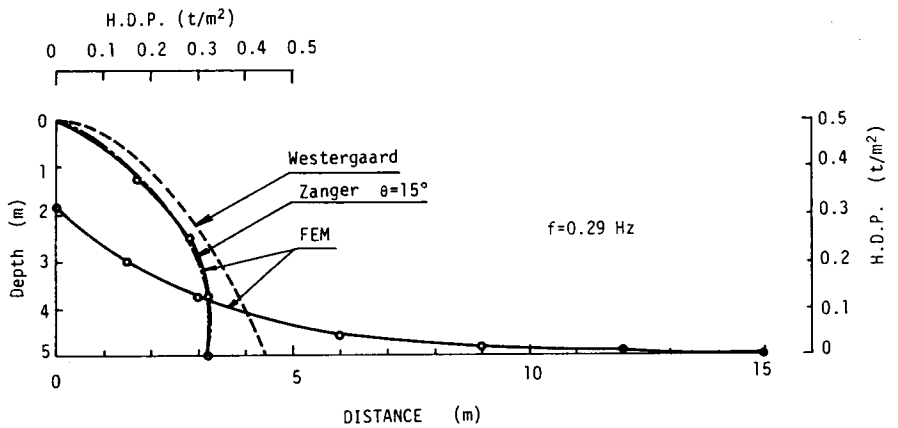

Fig. 6-3 The distribution of hydrodynamic pressure at a low frequency (0.29 Hz).

Figure 6-4 shows the distribution of hydrodynamic pressure at 3.36 Hz, close to the resonant frequency. Comparing this with Fig. 6-3, the amplification of hydrodynamic pressure is remarkable on the upper half of the water depth. This is attributed to the amplified acceleration of the structure caused by its rocking motion. The magnitude of hydrodynamic pressure is more than 5 times those obtained by either Westergaard's or Zanger's equations which are approximate, and are, therefore, no longer applicable.

On the other hand, hydrodynamic pressure acting on the bottom of the water exponentially decreases with the distance from the structure and becomes negligible at a distance of 2.5 ∿3.0 times that of the depth of water (Figs. 6-3 and 6-4). the appropriate extent of the water system modeled by finite element meshes is about three times that of its depth.

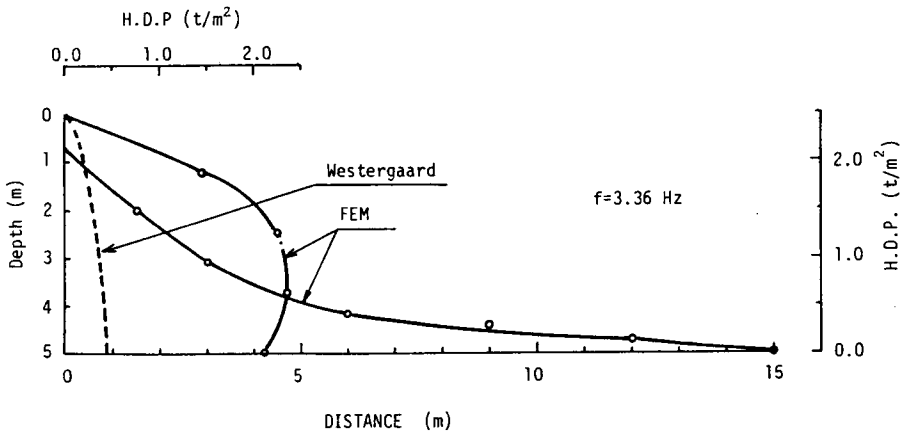

Fig. 6-4 The distribution of hydrodynamic pressure in the vicinity of the system's resonant frequency (3.36 Hz).

(3) Frequency response analyses of hydrodynamic pressure

Figure 6-5 shows frequency response curves of hydrodynamic pressure at various points along the structure's surface. Figure 6-6 shows the magnification factors of acceleration at the top and the bottom of the structure. Since hydrodynamic pressure strongly depends on the response

acceleration (Eq. 6-17), the response curves well agree with acceleration curves. Hydrodynamic pressure is increasingly affected by the vertical motion of the bottom of the water as its depth increases. That is, the frequency components near 8 Hz predominate as depth increases, and 8 Hz is the predominant frequency of the vertical motion of the bottom surface.

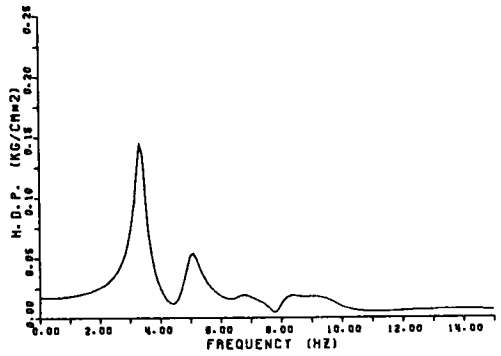

(a) 1.25 m in depth

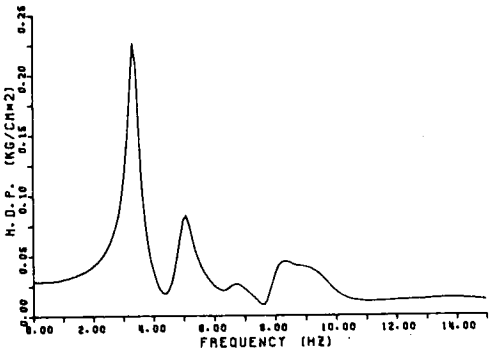

(b) 2.5 m in depth

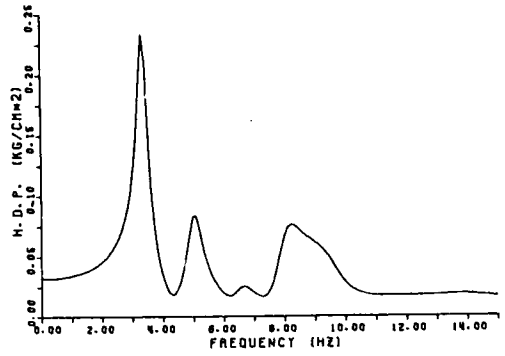

(c) 3.75 m in depth

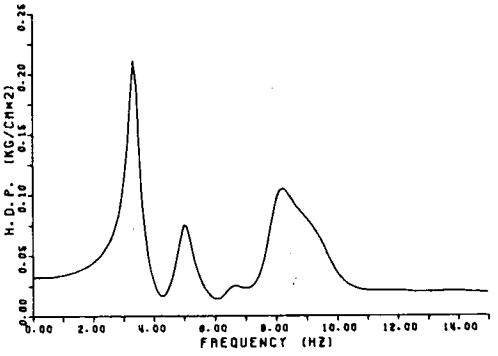

(d) 5.0 m in depth (the bottom of the water)

Fig. 6-5 A comparison of the frequency response curves of hydrodynamic pressure caused by horizontal sinusoidal ground motion (100 gal) at different depths.

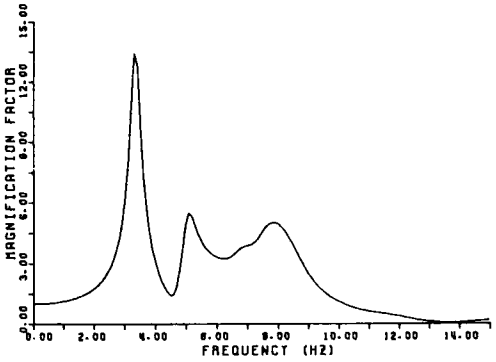

(a) The horizontal component at the top of the structure

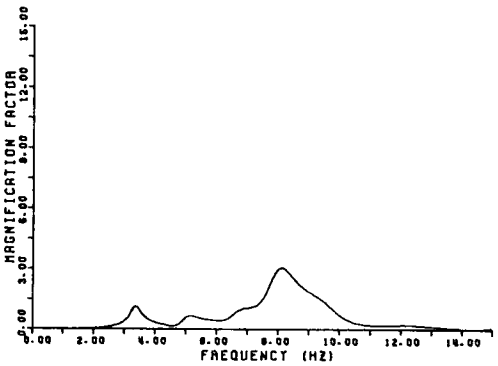

(b) The horizontal component at the bottom of the water

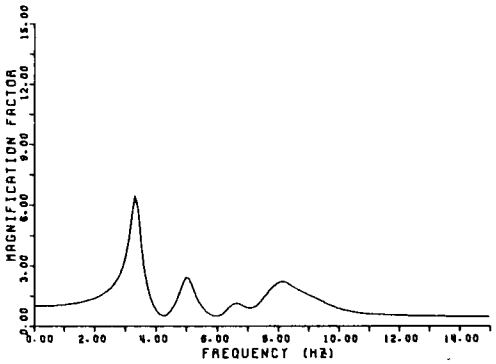

(c) The vertical component at the top of the structure

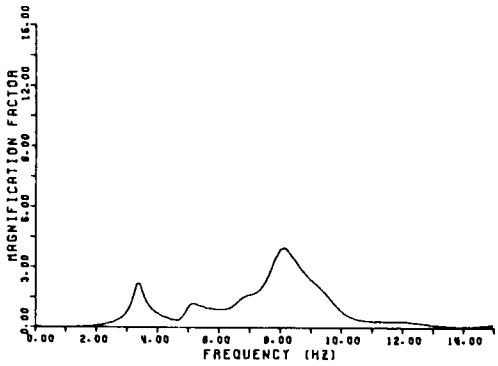

(d) The vertical component at the bottom of the water

Fig. 6-6 Structural response curves during horizontal ground motion.

(4) The influence of hydrodynamic pressure on the behavior of the revetment structure

A comparison of horizontal response acceleration at the top of the structure between Models 1 and 2 has been made in Fig. 6-7 in order to

investigate the effects of hydrodynamic pressure. The solid line shows Model 1 and the broken line, Model 2. The fundamental natural frequency of Model 2 is 3.37 Hz (Table 6-2) and the first resonant frequency of Model 1 is 3.35 Hz as shown in Fig. 6-7. As obvious from Eq. 6-18, hydrodynamic pressure contributes to the equation of motion of the system as its virtual mass, and the reduction of first resonant frequency due to virtual mass is only 0.02 Hz. The rate of resonant frequency reduction tends to increase as frequency increases. Virtual mass tends to increase amplification in low frequency ranges and decrease it in high frequency ranges. In general, however, the difference is not significant between these two response curves.

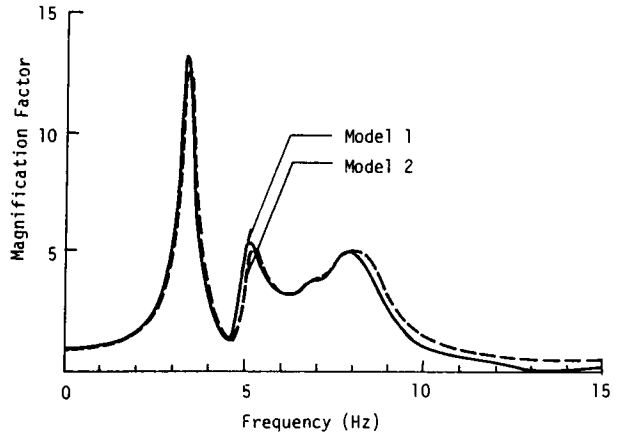

Fig. 6-7 The effects of hydrodynamic pressure on structural response acceleration during horizontal ground motion.

The maximum response values obtained by the FFT technique are summarized in Table 6-3. The models were subjected to the NS component of the El Centro accelerogram of a 100 gal maximum amplitude. All response values of Model 1 are 2 ∿ 5 % larger than those of Model 2. This implies that virtual mass increases structural responses in some cases, but its effects are not very significant. Similar results have been reported by Uwabe and Takahashi[10].

Table 6-3 Maximum response acceleration, velocity and displacement at the top of the structure (linear models).

	Item	Model 1	Model 2
Horizontal	Acceleration (gal)	330	313
	Velocity (kine)	14	13
	Displacement (mm)	6.0	5.9
Vertical	Acceleration (gal)	61	58
	Velocity (kine)	2.10	1.81
	Displacement (mm)	0.60	0.56

6.4 Nonlinear seismic response analyses of soil-structure-water interaction systems

(1) The model analyzed

Dynamic analyses in the previous section were based on the assumption that the soil was linear elastic material and that the contact surface between the soil and structure was perfectly bonded. In past earthquakes, however, there has been damage such as subsidence or cracking in the filled area, swelling and tilting toward the sea of the quaywall. These belong to the category of destructive phenomena, and cannot be treated by linear analyses.

In this section, the dynamic stress state of the filled area, and the dynamic stability of the revetment structure are investigated taking into account the effects of hydrodynamic pressure. The soil is assumed to be elasto-perfect plastic material and the Mohr-Coulomb failure law is employed as the yield criterion. Contact surfaces are modeled by joint element arrangements, and are dealt with as in previous chapters. The four-nodal-point isoparametric element is adopted in stead of the eight-nodal-point one adopted in section 6.3. The finite element mesh is shown in Fig. 6-8.

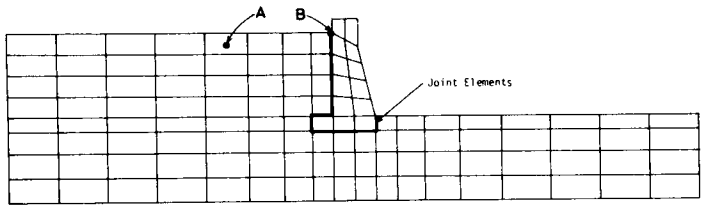

Fig. 6-8 Finite element mesh for a nonlinear seismic response analysis.

(2) The introduction of hydrodynamic pressure effects into the nonlinear dynamic response analysis

Hydrodynamic pressure is included as virtual mass in the equation of motion of the soil-structure interaction system. Accordingly, the frequency dependence of Eq. 6-19's second term corresponding to virtual mass was examined first. The results are shown in Fig. 6-9. Since the $[H]$ and $[Q]$ matrices of the infinite element are complex, this term is also complex. The real and imaginary parts of the two diagonal elements of the virtual mass matrix are shown. They correspond to depths of 2.5 m and 5.0 m, the bottom of the water. From Fig. 6-9, the imaginary part is extremely small when compared to the real part, and the real part is almost completely independent of frequency, and can be regarded as constant in this frequency range which is important from an engineering point of view.

Taking the fundamental natural circular frequency $\omega_0 = 2\pi f_0 = 2\pi \times 3.37$ (rad) as ω in the second term of Eq. 6-19 and denoting the resulting constant matrix as $[M']$, the hydrodynamic pressure vector, $\{p\}$ is:

$$\{p\} = [L]^{-1}[M']\left(\{a_g\} + \{\ddot{\delta}\}\right) \tag{6-20}$$

Substituting Eq. 6-20 into Eq. 6-12, the nonlinear equation of motion of the soil-structure system when the effect of hydrodynamic pressure is

considered is:

$$([M] + [M']\{\ddot{\delta}\} + [C]\{\dot{\delta}\} + [K]\{\delta\} = -([M] + [M']\{a_g\} \qquad (6\text{-}21)$$

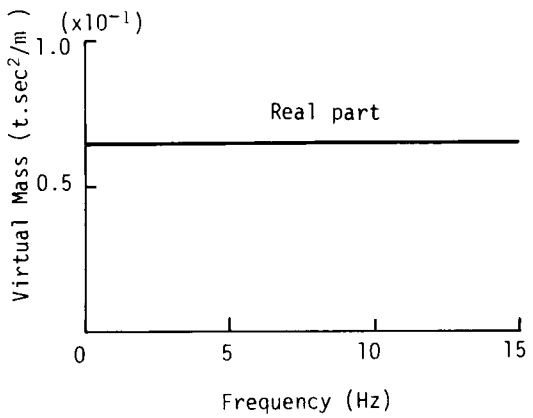

(a) The real part of the virtual mass matrix component (2.5 m in depth)

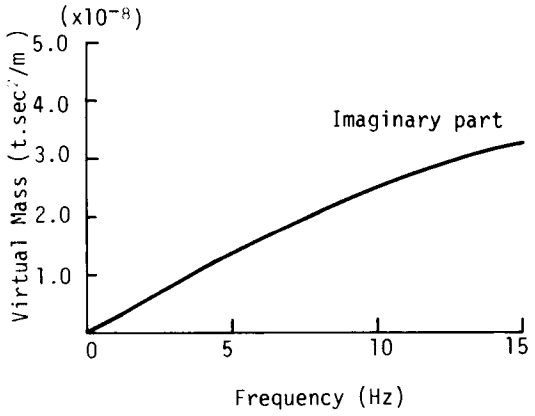

(b) The imaginary part of the virtual mass matrix component (2.5 m in depth)

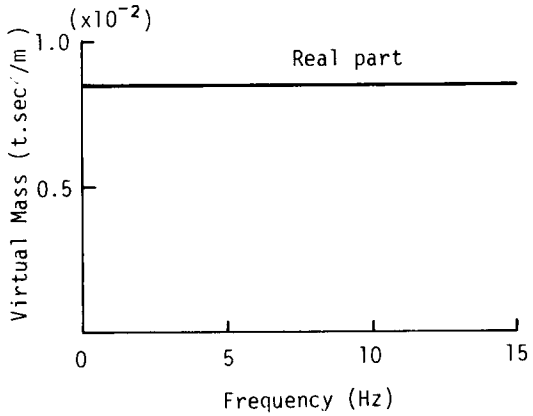

(c) The real part of the virtual mass matrix component (5.0 m in depth)

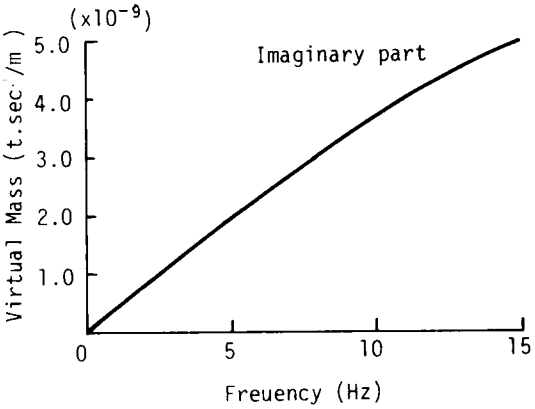

(d) The imaginary part of the virtual mass matrix component (5.0 m in depth)

Fig. 6-9 Frequency characteristics of virtual mass.

(3) The initial stress state

When estimating the initial stress state, hydrostatic pressure should also be considered. Figure 6-10 shows the initial stresses in Model 1 on the contact surfaces between the revetment structure and the surrounding ground. (a) shows the distribution of normal stress and (b) shear stress. Figures 6-11(a) and (b) are normal and shear stress in Model 2. Hydrodynamic pressure significantly reduces shear stress along the base of the structure while only slightly altering normal stress along the contact surface.

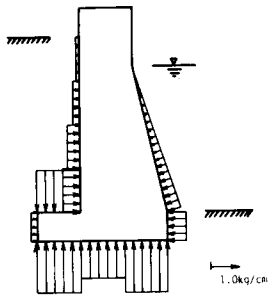

(a) Normal stress

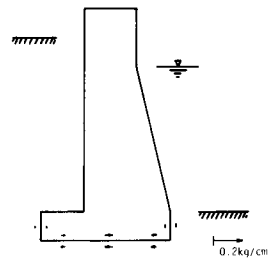

(b) Shear stress

Fig. 6-10 Model 1 - The distribution of initial stresses due to gravity force acting on the structure.

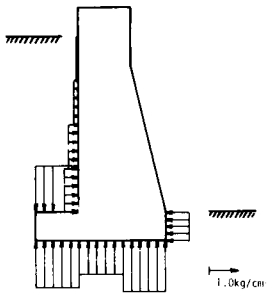

(a) Normal stress

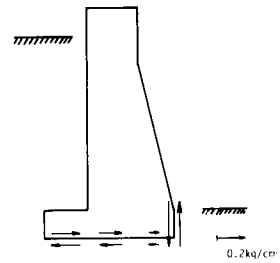

(b) Shear stress

Fig. 6-11 Model 2 - The distribution of initial stresses due to gravity force acting on the structure.

(4) Nonlinear behavior of soil-structure interaction systems

Model 3 is introduced in this section. Model 1 includes both hydrodynamic and hydrostatic pressure, Model 2, neither of these and now in Model 3, hydrostatic pressure is included to estimate initial stresses but hydrodynamic pressure is ignored. The strength parameters of the soil and the contact surfaces are listed in Table 6-4.

Table 6-4 Strength parameters controlling shear strength of soils and joint element.

	Cohesion (tf/m^2)	Angle of internal friction (degree)
Back-filling soil	0.0	40
Surface layer	3.0	35
Joint element	0.0	30

(a) Nonlinear seismic response of soil-structure interaction systems

The maximum responses at the top of the revetment structure are listed in Table 6-5 when the models were subjected to the NS component of the El Centro accelerograms of a reduced maximum acceleration of 100 gal. The maximum values are almost identical for the three models and also nearly equal those for linear models (Table 6-3).

Table 6-5 Maximum response acceleration, velocity and displacement at the top of the structure (nonlinear models).

	Item	Model 1	Model 2	Model 3
Horizontal	Acceleration (gal)	327	310	304
	Velocity (kine)	14	13	14
	Displacement (mm)	6.2	6.1	6.0
Vertical	Acceleration (gal)	66	63	64
	Velocity (kine)	1.84	1.87	1.93
	Displacement (mm)	0.59	0.64	0.60

The shaded areas in Fig. 6-12 show the elements which yielded during the period of 2.0 ∿ 2.5 sec, or the main shock. Figure (a) shows Model 1, (b) Model 2 and (c) Model 3. In the figures, the joint elements which separated or slid are marked by solid and regular broken lines, respectively. Model 2 had the widest zone of yield, and Model 3 had the narrowest zone. Figure 6-13 shows the hysteresis curves of τ_{xy}- γ_{xy} relationships of the soil at point A in Fig. 6-8. The plastic strains are almost the same for all models despite their different yielded areas. At the contact surface between the back-filling and the

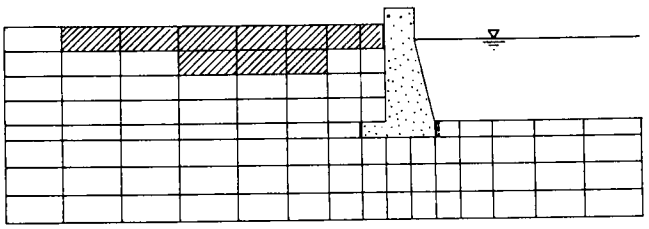

(a) Model 1

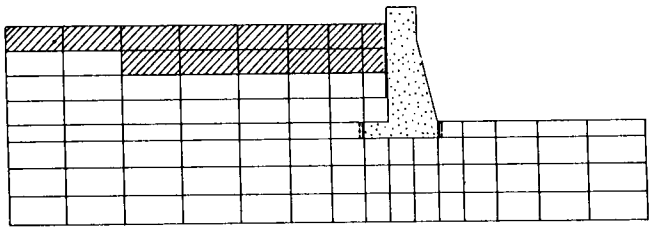

(b) Model 2

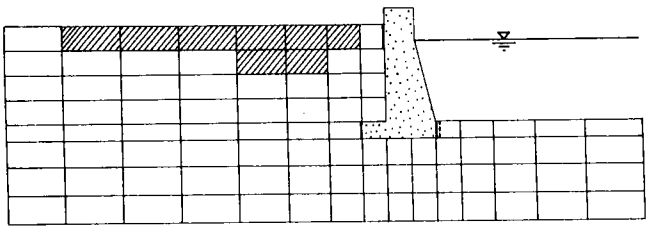

(c) Model 3

Fig. 6-12 Failure zone of back-filling elements and joint elements which have slid or separated.

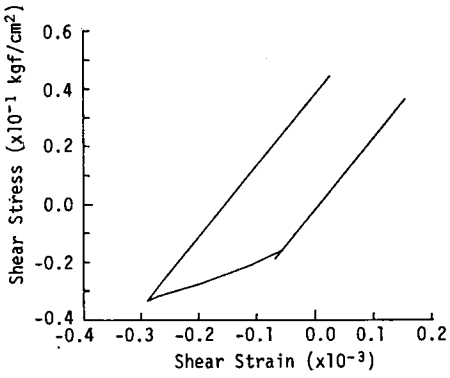

(a) Model 1

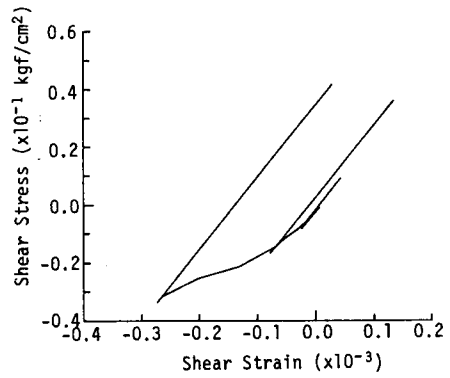

(b) Model 2

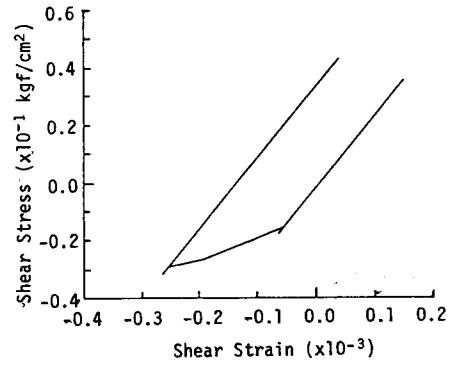

(c) Model 3

Fig. 6-13 The hysteresis loop of τ_{xy}-γ_{xy} at point A of Fig. 6-8.

structure, the greatest sliding occurred in Model 2, while that in Models 1 and 3 was limited to the ground surface.

The maximum horizontal accelerations were of the order of 300 gal, at which level separation did not take place implying that cracking did not occur.

Seismic response analyses have been performed for the 200 gal imput accelerogram. Figure 6-14 shows the zone of yield, separation and sliding. Figure (a) shows Model 1 and (b) Model 2. The maximum response accelerations at the top of the structure is about 680 gal in both and there is little difference. As can be seen from Fig. 6-14, in Model 2, however, almost the entire area of back-filling has yielded and sliding has spread to the bottom of the structure (6 m in depth), and besides, separation has spread to 3 m in depth. On the other hand, these phenomena are much more limited in Model 1. The nonlinear features of the models thus differ considerably although thier maximum response accelerations are almost identical.

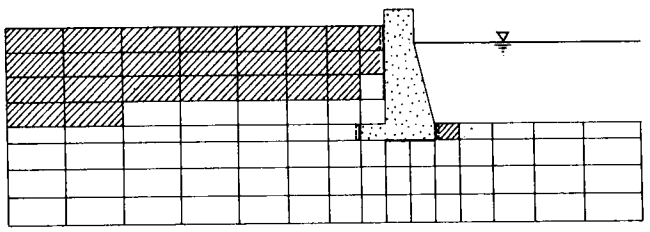

(a) Model 1

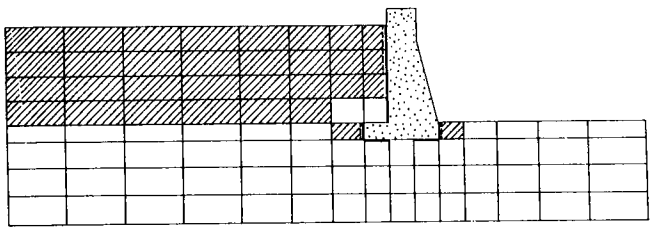

(b) Model 2

Fig. 6-14 Failure zone of back-filling elements and joint elements which have slid or separated.

Figure 6-15 shows the time histories of vertical displacement at point B on the ground surface, with (a) and (b) for Models 1 and 2. Residual displacement (or subsidence) caused by the yielding of the soil occured at about 2.4 sec, and it was of the order of several millimeters. One reason subsidence is so small is that tilting and/or swelling and sliding of the structure did not occur, but it would have increased if they had occurred.

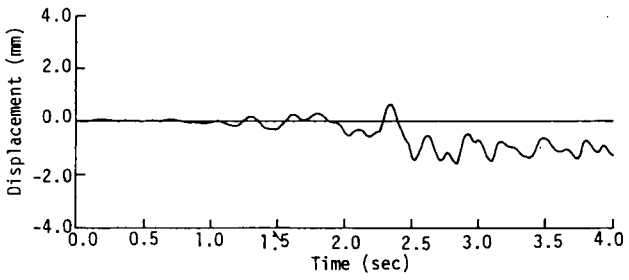

(a) Model 1

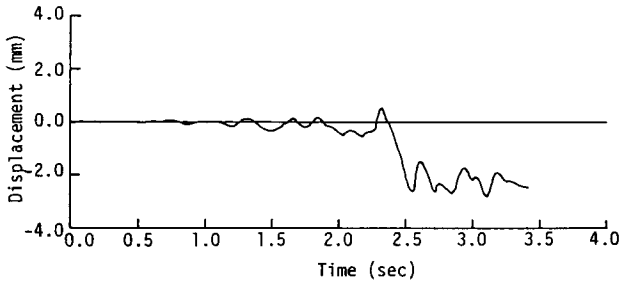

(b) Model 2

Fig. 6-15 Vertical displacement showing settlement at point B of Fig. 6-8.

(b) The dynamic stability of the revetment structure

The effects of hydrodynamic pressure on the overturning moment and on the sliding stability of the revetment structure have been investigated. The dynamic overturning moment is calculated from the stresses which have developed on the joint element which is in contact with the structure[14]. Safety against sliding is discussed using the total safety factor[15] defined by Eq. 2-27. TSF is assessed from the stresses on three

joint elements arranged along the structural bottom.

Overturning moments and TSF values are tabulated in Table 6-6 when the three models were subjected to 100 gal or 200 gal NS components of the El Centro accelerograms. In the table, the eccentricities, e, calculated from the overturning moments are also listed. The largest moment is developed in Model 2 regardless of the input acceleration amplitude, and the smallest in Model 3. The moment of Model 1 is 15 % larger than that of Model 3 regardless of the excitation amplitude, and is nearly equal to that of Model 2.

The eccentricity, e, gives an assessment of the safety against overturning. In earthquakes, if the eccentricity is less than one-third of the width of the structural base, B, the structure is regarded as safe and stable[16].

Table 6-6 Maximum overturning moments and TSF values.

Amplitude of input acceleration (gal)	Model	Overturning moment (tf·m)	Eccentric distance (m)	T S F
100	Model 1	26.9	0.57	4.43
	Model 2	31.4	0.66	3.20
	Model 3	23.2	0.49	4.90
200	Model 1	44.7	0.95	1.64
	Model 2	45.1	0.95	1.62
	Model 3	38.4	0.81	1.71

The eccentricity of Model 2 subjected to a 200 gal excitation is 0.95 m, the largest, and with the width of the structural base, as 4.5 m, then

$$\frac{e}{B} = 0.21 < \frac{1}{3} \tag{6-22}$$

or in other words, the structure is stable against overturning. Model 2 has the lowest safety factor in terms of sliding stability. When the ex-

citation is 200 gal, however, the safety factors of Model 1 nearly equals to that of Model 2, the same tendency as that of overturning moment.

It can be concluded that the dynamic stability of the revetment structure is lowered by hydrodynamic pressure to the level as when there is no water. In that case, the dynamic stability of the revetment structure is at its lowest.

6.5 Conclusions

Using the finite element method, linear and nonlinear seismic response analyses were made of water-soil-revetment structure interaction systems to investigate the effects of hydrodynamic pressure on the system's responses and on structural dynamic stability.

The results can be summarized as follows:

(1) Although the magnitude of hydrodynamic pressure acting on the wall can be estimated by Westergaard's or Zangar's equations with sufficient accuracy for low frequency ranges, it is actually several times larger at the resonant frequency of the system, and these equations therefore are no longer applicable.

(2) Since hydrodynamic pressure acts as virtual mass in the system, it decreases the resonant frequency of the structure. In the case, however, where the water is shallow and there is back-filling soil as was true here, the effects of hydrodynamic pressure on maximum acceleration, velocity and displacement are not significant.

(3) Because virtual mass can be regarded as a constant independent of frequency in the important frequency ranges in engineering sense provided that the water is not very deep, it can be introduced as approximately a constant in nonlinear seismic response analyses.

(4) In general, the existence of water results in greater revetment structure stability. However, as the excitation level increases, the dynamic stability of the structure decreases to the same level as when water does not exist .

As the model structure is very stiff and heavy, it is less affected by hydrodynamic pressure. However, when they are flexible structures such as sheetpiles or if the water is deeper, its effects on structural responses are more significant.

Finally, although the analyses presented here are based on a total stress analysis, they should in the future be based on the effective stress field with considerations given to dynamic soil-ground water interactions because the ground water table is high in the places where revetment structures are constructed, and a large amount of damage due to liquefaction has been reported.

Chapter 6 references

1) Westergaard H. M.: Water pressure on dams during earthquakes, Trans. ASCE, Vol.98, p.413, 1933.

2) Zienkiewicz O. C. and P. Bettess: Coupled hydrodynamic response of concrete gravity dam using finite element and infinite element, Int. J. Earthq. Eng. Struc. Dyn., Vol.6, pp.363-374, 1978.

3) Chopra O. K.: Earthquake analysis of concrete gravity dams including dam-water-foundation rock interaction, Int. J. Earthq. Eng. Struc. Dyn., Vol.9, pp.366-383, 1981.

4) Shibata T., T. Sato and Y. Tatsumi: Dynamic analysis of the earth retaining wall by the finite element method, Proc. 4th Japan Earthquake Engineering Symposium, pp.455-462, 1975, (in Japanese).

5) Shibata T., T. Sato and Y. Tatsumi: Prediction of earthquake damage to quaywall structures, Ann. of D.P.R.I., Kyoto University, No.20B, pp.1-17, 1977, (in Japanese).

6) Zienkiewicz O. C.: The finite element method, 3rd Ed., McGraw-Hill, pp.148-177, 1972.

7) Zienkiewicz O. C. and R. E. Newton: Coupled vibrations of a structure submerged in a compressible fluid, Proc. Int. Symp. Finite Element Tech., 1969.

8) Zienkiewicz O. C. and P. Bettess: Diffraction and refraction of surface waves using finite and infinite elements, Int. J. Num. Meth. Eng. Vol.11, pp.1271-1290, 1977.

9) Ohara S.: The latest earthquake engineering, Morikita Shuppan, pp.128-129, 1975, (in Japanese).

10) Uwabe T. and H. Takahashi: Vibrative experiment on the hydrodynamic pressure acting on the high mound breakwater, 36th Proc. of the annual meeting of JSCE, pp.335-336, 1981. (in Japanese).

11) General report on the 1978 Miyagiken-oki earthquake, Investigation committee of the 1978 Miyagiken-oki earthquake at Tohoku Branch of

JSCE, 1980, (in Japanese).

Toki K., T. Sato and F. Miura: Separation and sliding between soil and structure during strong ground motion, Int. J. Earthq. Eng. Struc. Dyn., Vol.9, pp.266-277, 1981.

13) Toki K. and F. Miura: Nonlinear seismic response analysis of soil-structure interaction system, Proc. JSCE, No.317, pp.61-68, 1982, (in Japanese).

14) Toki K., F. Miura and T. Yoshimura: The dynamic stability analysis of the structure during strong earthquake motion, Report of 16th meeting of earthquake engineering, pp.116-116, 1981, (in Japanese).

15) Toki K., F. Miura and T. Otake: Nonlinear seismic response analysis of soil-structure interaction system by the 3-dimensional joint element, Proc. JSCE, No.322, pp.51-61, 1982, (in Japanese).

16) Aoki S., Y. Hirano and I. Hirahara: Examples of design for the spread foundation the pier and the abutment, Sankaido, pp.5-6, 1979, (in Japanese).

Appendix 6-I

The shape function matrix of the eight-nodal-point isoparametric element, $[N]$, is (see Fig. 6-A-1):

$$[N] = \begin{bmatrix} N_1 & 0 & N_2 & 0 & \cdots & N_8 & 0 \\ 0 & N_1 & 0 & N_2 & \cdots & 0 & N_8 \end{bmatrix} \tag{6-A-1}$$

where,

$$\left.\begin{aligned} N_1 &= (1-s)(1+t)(-s+t-1)/4 \\ N_2 &= (1-s)(1-t^2)/2 \\ N_3 &= (1-s)(1-t)(-s-t-1)/4 \\ N_4 &= (1-s^2)(1-t)/2 \\ N_5 &= (1+s)(1-t)(s-t-1)/4 \\ N_6 &= (1+s)(1-t^2)/2 \\ N_7 &= (1+s)(1+t)(s+t-1)/4 \\ N_8 &= (1-s^2)(1+t)/2 \end{aligned}\right\} \tag{6-A-2}$$

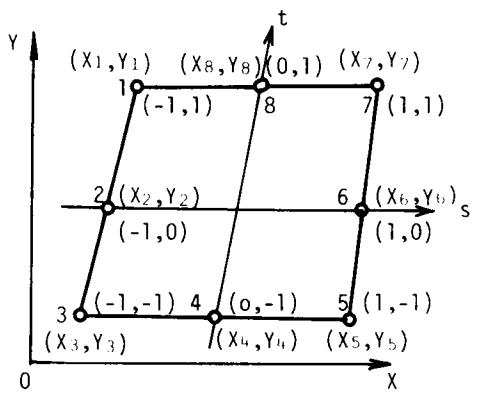

Fig. 6-A-1 An isoparametric element with eight nodal points.

Appendix 6-II

The shape function of the infinite element (Fig. 6-A-2) in x-direction is:

$$\left.\begin{aligned} L_1 &= \left(1-\frac{x}{l}\right)e^{-\left(\frac{1}{\lambda}+ik\right)x} \\ L_2 &= \frac{x}{l}\,e^{\frac{\lambda}{l}}\,e^{-\left(\frac{1}{\lambda}+ik\right)x} \\ L_3 &= 1-L_1-L_2 \end{aligned}\right\} \qquad (6\text{-A-3})$$

where,

$$\lambda = \frac{C}{a\omega} \qquad k = \frac{\omega}{C} \qquad (6\text{-A-4})$$

and C is the velocity of sound in water, a is radiation damping parameter and ω the circular frequency.

In y-direction,

$$\left.\begin{aligned} M_1 &= \frac{2}{h^2}\left(y+\frac{h}{2}\right)y \\ M_2 &= \frac{4}{h^2}\left(\frac{h}{2}-y\right)\left(\frac{h}{2}+y\right) \\ M_3 &= \frac{2}{h^2}\left(y-\frac{h}{2}\right)y \end{aligned}\right\} \qquad (6\text{-A-5})$$

Therefore, the shape function between nodal points i and j, N, can be written as:

$$N_{ij} = L_i M_j \qquad (6\text{-A-6})$$

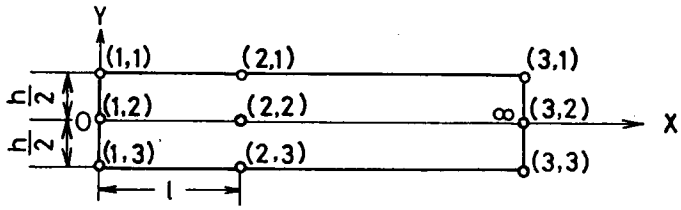

Fig. 6-A-2 The infinite element.

CONCLUDING REMARKS

This dissertation has presented an effective method to analyze nonlinear dynamic soil-structure interaction considering not only the nonlinear behavior of soil but also sliding and separation phenomena at the contact surface between the soil and the structure by the finite element method. In this study, the method has been applied to soil-structure, soil-rock and soil-structure-water systems. The main results are briefly summarized, followed by proposals for future research.

The method is based on the application of the joint element which was developed by static rock mechanics, to dynamic soil-structure interaction. The analytical procedures are described in detail in chapters 1, 2 and 3 and the applicability was discussed. In order to determine the constitutive relationships of the joint element, numerous simple shear tests were carried out. The results demonstrated the validity of modeling the constitutive relationships as an elasto-perfect plastic type. The load transfer method was adopted for nonlinear seismic response analyses. CPU time was in this way greatly reduced compared to that required by other nonlinear techniques. An analysis assuming perfect bonding at the contact surface did not estimate the system's responses correctly. Moreover, a detailed explanation of such mechanisms as the development of sliding with time, or the redistribution of stresses along a contact surface where sliding or separation was taking place, was made possible by this approach.

The stability against sliding of a nuclear reactor building was investigated for several strong types of earthquake motions. Safety factor obtained by the classical method were lower than those obtained from the proposed dynamic method. The difference was, however, less than 10 %.

The difference was attributed to the nonlinear behavior of soil and to local sliding at the contact surface.

It is very important to make clear the validity or limitations of replacing a real three-dimensional system by a two-dimensional model, and to do so, a three-dimensional joint element was developed (chapter 3). Its applicability was examined in detail and was found to be adequate. The structural stability against sliding was examined, and the safety factors obtained from two-dimensional models were lower than those of the three-dimensional one. This implies that a real three-dimensional structure will remain safe even when a replaced two-dimensional model subjected to seismic force is at a critical state against sliding.

The applications of the method were demonstrated in chapters 4, 5 and 6. Dynamic characteristics of pile-foundation structures were investigated (chapter 4) focusing the effects of embedment of the footing, the friction resistance on the pile surface and the dynamic lateral group efficiency of a group of piles. Embedding the footing caused a reduction in structural response by approximately 10 %, and a 40 % reduction in shear stress in the pile head. The shared rate of normal resistance at the pile tip is predominant for dead load, whereas shearing resistance by the pile surface is predominant for dynamic load. The increase of a number of piles would sometimes caused increases rather than decreases in structural responses, a result the reverse of the case for static force. This must be taken into consideration when pile foundations are designed by the seismic coefficient method.

Dynamic stability of a existing slope was investigated in chapter 5. Both the present method and that of Janbu which is practically used, gave similar safety factors. Slope stability during earthquakes depends not only on the amplitude of the excitation but also on its predominant frequency. Ground water remarkably lowered the level of stability and therefore, it is essential to keep the water table level as

low as possible. Stability was re-measured when the slope had been reinforced by sheetpiles and the required sheetpile strength was determined when the slope is subjected to strong earthquake motions.

In chapter 6, a revetment structure was discussed in terms of the effects of hydrodynamic pressure on its dynamic stability. The virtual mass, equivalent to hydrodynamic pressure, was approximately independent of frequency as long as the water was not as deep as that in the model analyzed here. A procedure to handle hydrodynamic pressure has been described. Structural dynamic stability decreased to the same degree when excitation level was increased as when there was no water, although the existence of water, in general, gave greater stability.

In considering structural dynamic stability classical methods such as the seismic coefficient method, in which the seismic load is statically applied, are convenient for the practical design purposes because of their simplicity. Therefore, the relationship between safety factors obtained from classical methods and the dynamic type proposed here must be understood. The latter is a powerful tool which, in fact, has already given significant results.

Nevertheless, there still exist certain unsolved problems. First, throughout this paper, analyses were based on total stress. They should in fact be based on effective stress by evaluating the dynamic interaction between the soil and ground water when the effect of ground water is expected to have significant effects, as in chapters 5 and 6. Secondly, although three-dimensional models were analyzed (chapter 3), they were discretized by coarse finite element meshes. Models of greater detail with fine meshes are required for greater accuracy. Finaly, as is evident from the meshes used here, their greater portion represent the ground because the model does not permit radiation damping. For a precise discussion of the dynamic stability analysis, a computer code must be developed which permits the energy transmission through the artificially truncated boundaries in nonlinear dynamic analyses.